# Differentiable solver for time-dependent deformation problems with contact

ZIZHOU HUANG[*], New York University, USA

DAVI COLLI TOZONI[*], NTop and New York University, USA

ARVI GJOKA, New York University, USA

ZACHARY FERGUSON, Massachusetts Institute of Technology and New York University, USA

TESEO SCHNEIDER, University of Victoria, Canada

DANIELE PANOZZO, New York University, USA

DENIS ZORIN, New York University, USA

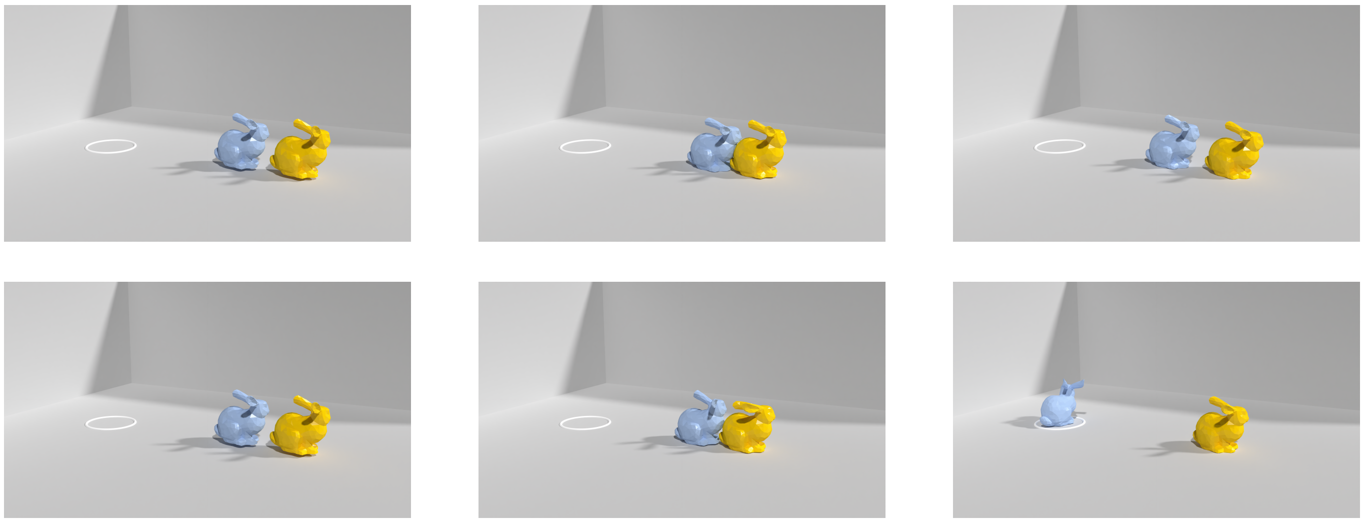

Fig. 1. The direction and magnitude of the initial velocity of the yellow bunny is optimized to push, after contact, the blue bunny into the white circle marker. Top row is the initial configuration, and bottom row is our optimized result. This scene involves a elastodynamic simulation with a non-linear material model with contact and friction forces.

We introduce a general differentiable solver for time-dependent deformation problems with contact and friction. Our approach uses a finite element discretization with a high-order time integrator coupled with the recently proposed incremental potential contact method for handling contact and friction forces to solve ODE- and PDE-constrained optimization problems on scenes with complex geometry. It supports static and dynamic problems and differentiation with respect to all physical parameters involved in the physical problem description, which include shape, material parameters, friction parameters, and initial conditions. Our analytically derived adjoint formulation is efficient, with a small overhead (typically less than 10% for nonlinear problems) over the forward simulation, and shares many similarities with the forward problem, allowing the reuse of large parts of existing forward simulator code.

We implement our approach on top of the open-source PolyFEM library and demonstrate the applicability of our solver to shape design, initial condition

[*]Joint first authors with equal contributions

Authors' addresses: Zizhou Huang, zizhou@nyu.edu, New York University, USA; Davi Colli Tozoni, NTop and New York University, USA, davi.tozoni@nyu.edu; Arvi Gjoka, New York University, USA, arvi.gjoka@nyu.edu; Zachary Ferguson, Massachusetts Institute of Technology and New York University, USA, zfergus@mit.edu; Teseo Schneider, University of Victoria, Canada, teseo@uvic.ca; Daniele Panozzo, New York University, USA, panozzo@nyu.edu; Denis Zorin, New York University, USA, dzorin@cs.nyu.edu.

0730-0301/2024/3-ART $15.00
https://doi.org/10.1145/nnnnnnn.nnnnnnn

optimization, and material estimation on both simulated results and physical validations.

Additional Key Words and Phrases: Differentiable Simulation, Finite Element Method, Elastodynamics, Frictional Contact

**ACM Reference Format:**

Zizhou Huang, Davi Colli Tozoni, Arvi Gjoka, Zachary Ferguson, Teseo Schneider, Daniele Panozzo, and Denis Zorin. 2024. Differentiable solver for time-dependent deformation problems with contact. *ACM Trans. Graph.* 1, 1 (March 2024), 31 pages. https://doi.org/10.1145/nnnnnnn.nnnnnnn

## 1 INTRODUCTION

ODE- and PDE-constrained optimization problems, i.e. the minimization of a functional depending on the state of a physical system modeled using a set of (partial) differential equations, appear in many application areas: optimized design in engineering and architecture, metamaterial design in material science, inverse problems in biomedical applications, controllable physically-based modeling in computer graphics, control policy optimization, and physical parameter estimation in robotics.

A common family of PDE-constrained optimization problems in graphics, robotics, and engineering involves static or time-dependent elastic deforming objects interacting with each other via contact and friction forces. A significant number of approaches have been proposed to tackle PDE-constrained optimization problems of this type (Section 2).

However, these approaches often make application-specific assumptions aimed at simplifying the differentiable simulator, often sacrificing generality (e.g., handling contact only with simple rigid obstacles or differentiating with respect to material parameters only), robustness (e.g., using a contact model that requires per-scene parameter tuning to prevent failure), accuracy (e.g., using approximate spatial discretizations, or non-physical material and friction models), or scalability (e.g., restricting the number of system parameters with respect to which it can be optimized).

Building on and integrating a broad range of previous work on PDE-constrained optimization, including shape optimization, material property estimation, and trajectory control, we develop a differentiable solver that eliminates or reduces these shortcomings. Our solver has the following characteristics:

(1) Maximally *general differentiability*: we support differentiation with respect to all physical parameters (Section 8) involved in the physical problem description: shape, material parameters, friction parameters, and initial conditions. The user can pick an arbitrary subset of these parameters to use in objective functions (Section 9.1), differently from previous works which limit this selection (Table 1).

(2) Our contact/friction formulation builds upon the recently proposed Incremental Potential Contact (Section 8.2) approach [Li et al. 2020]. Our differentiable simulator supports complex geometry, is automatic and robust (with only two main parameters controlling the accuracy of the spatial and temporal discretizations), and guarantees physically valid configurations at all timesteps, without intersections nor inverted elements. Many previous works instead use a restricted set of contact scenarios (Table 1).

(3) We use discretizations of arbitrary order (Section 10), both in space and time with general non-linear elasticity material models, ensuring *accuracy*. Many competing works instead rely on linear time and spatial discretization and often use simplified material models, leading to lower accuracy solutions (Section 2).

(4) Our formulation supports both static and dynamic problems in a unified framework (Section 4).

(5) Our differentiation approach is *low cost*. The computation of the derivatives for one PDE-constrained optimization step is at most as expensive as a forward evaluation of the underlying forward simulation of the physical systems (Section 4.3, Table 4), and, for nonlinear problems, we observe that the differentiability adds at most 10% to the cost.

While individually most of these features appeared in previous works in some form, they have never been combined in a unified formulation and algorithm for accurately solving inverse problems in elastodynamics with contact. The foundation of our approach is the *adjoint method*, which we systematically apply to obtain derivatives with respect to all parameters in a unified and general way, while achieving high efficiency. We discuss our design choices and compare to alternatives in Section 2.1.

We demonstrate the effectiveness of our approach on a set of examples involving multiple objectives and optimizing for the shape, material parameters, friction parameters, and initial conditions.

## 2 RELATED WORK

We summarize the most relevant simulation frameworks, primarily focusing on those supporting differentiable simulations of elastic deformable objects.

For the works closer to our targeted applications, we provide an explicit breakdown of which subset of the characteristics of our solver they support (Table 1). We also highlight the generality of our solver by explicitly identifying which solvers cannot reproduce the examples in our paper (Table 2). While implementing additional derivatives with respect to parameters already present in one of these codes is easy in some cases, other features are harder to add, e.g., contact between soft bodies or self-collisions. The reasons why specific solvers cannot handle certain problems are included in the caption of Table 2. We note that prior works in Tables 1, 2 can solve problems that our method cannot handle, e.g. the application in visuomotor control tasks in [Jatavallabhula et al. 2021] is not included in this work.

**Differentiable deformable object simulators.** Numerous differentiable elastic body simulators have been developed for applications in optimal design of shapes [Ly et al. 2018; Panetta et al. 2017, 2015; Tozoni et al. 2020], actuators [Chen et al. 2020; Maloisel et al.

Table 1. The table columns correspond to five comparison characteristics: (1) High-order space and time discretization, (2) supported optimization parameters (3) support for complex contacts between arbitrary surfaces, including self-collision, (4) support for static and dynamic simulations, and (5) method for the derivatives computation. No existing differentiable solver supports all features of our solver simultaneously; in particular, most do not support differentiating with respect to the shape of the domain.

| Method | (1) HO | (2) Parameters | (3) Collisions | (4) Static and Dynamic | (5) Differentiation |
|---|---|---|---|---|---|
| Elastic Texture [Panetta et al. 2015] | Yes | Shape | No support | Static-Only | Adjoint |
| CB-Assemblies [Tozoni et al. 2021] | Yes | Shape | Static and Prescribed | Static-Only | Adjoint |
| ADD [Geilinger et al. 2020] | No | Material, Initial | Only planes or SDF, no self-collisions | Dynamic-Only | Adjoint |
| GradSim [Jatavallabhula et al. 2021] | No | Material, Initial | Only planes, no self-collisions | Dynamic-Only | Code transformation |
| DiSECt [Heiden et al. 2021] | No | Material | Only planes or SDF, no friction | Dynamic-Only | Code transformation/autodiff |
| NeuralSim [Heiden et al. 2020] | No | Material, Initial | Only rigid-bodies | Dynamic-Only | Code transformation/autodiff |
| DiffPD [Du et al. 2021] | No | Material, Initial | Only planes or SDF | Dynamic-Only | Adjoint |
| **Ours** | **Yes** | **Shape, Material, Initial** | **No restrictions** | **Static and Dynamic** | **Adjoint** |

Table 2. To clarify the differences between our approach and other differentiable simulators, we show which simulators support the features needed for each experiment in our paper. The figure captions provide more details for each experiment; most significantly, almost no other simulators support shape optimization (Fig 5–13), and the ones that do lack support for dynamic. From left to right: Fig 1 and 22 require contact handling between soft bodies; Fig 5–13 require shape optimization; Fig 16–17 require material distribution optimization; and Fig 19 and 21 require self-collision handling.

| Method | Fig1 | Fig5–10 | Fig11–13 | Fig14 | Fig16–17 | Fig18 | Fig19 | Fig20 | Fig21 | Fig22 | Fig23 |
|---|---|---|---|---|---|---|---|---|---|---|---|
| Elastic Texture [Panetta et al. 2015] | | | | | Y | | | | | | |
| CB-Assemblies [Tozoni et al. 2021] | | Y | | | | | | | | | |
| ADD [Geilinger et al. 2020] | | | | Y | | Y | | Y | | | Y |
| GradSim [Jatavallabhula et al. 2021] | | | | Y | | Y | | Y | | | Y |
| DiSECt [Heiden et al. 2021] | | | | | | Y | | Y | | | Y |
| NeuralSim [Heiden et al. 2020] | | | | | | | | | | | |
| DiffPD [Du et al. 2021] | | | | Y | | Y | | Y | Y | | Y |
| **Ours** | **Y** | **Y** | **Y** | **Y** | **Y** | **Y** | **Y** | **Y** | **Y** | **Y** | **Y** |

2021; Skouras et al. 2013], sensors [Tapia et al. 2020], material characterization [Hahn et al. 2019; Schumacher et al. 2020], and robotic control [Bern et al. 2019; Hoshyari et al. 2019]. Differentiable simulators are also developed for fluid simulations in [Li et al. 2023b; McNamara et al. 2004; Schenck and Fox 2018]. These simulators broadly fit into three categories: (i) those employing analytic derivatives computed using sensitivity analysis; (ii) those using automatic differentiation libraries [Heiden et al. 2020; Hu et al. 2019a] based on overloading, or algorithmic differentiation (iii) neural surrogate models replacing the entire simulation with a differentiable neural network [Baque et al. 2018; Bern et al. 2020; Chang et al. 2016; Zhang et al. 2016].

Our method belongs to the first category: analytic sensitivity analysis generally requires manual differentiation of the physics equations, but allows one to reuse existing solvers most easily; direct differentiation is feasible only if the number of parameters is very small; a large number of parameters requires construction of the adjoint equations for specific functionals [Bern et al. 2019; Du et al. 2021; Li et al. 2022; Liang et al. 2019; Ly et al. 2018; Qiao et al. 2020; Rojas et al. 2021], and is more efficient than all other approaches. One exception is Dolphin-Adjoint [Mitusch et al. 2019], which automatically and robustly derives adjoint models for models written in the finite element software FEniCS [Alnaes et al. 2015]. Automatic differentiation methods are most general but require existing simulators to be rewritten using data structures required for gradients and Hessians, and typically incur a significant performance penalty. Surrogate models, though enabling dramatic speedups in some cases, require huge training sets and long training times for even simple design spaces [Gavriil et al. 2020], and currently are unsuitable for high-precision applications [Bächer et al. 2021]. Code transformation and auto-differentiation, e.g. in simulators such as [Jatavallabhula et al. 2021] and [Heiden et al. 2021], based on technology developed in NVIDIA Warp [Xu et al. 2022], while potentially allowing one to reuse existing codes, typically places a few limitations on what the code may contain. To the best of our knowledge, none of the existing simulators support robust handling of contact and friction for complex geometries, and they only support a subset of the design parameters compared to the more general formulation of this paper.

We provide direct comparisons of our solver, [Du et al. 2021], and [Jatavallabhula et al. 2021] in Section 10.5.

**Differentiable Simulations with Contact.** Differentiable simulators incorporating various contact models have recently been developed for rigid [Heiden et al. 2020] and soft bodies [Geilinger et al. 2020; Heiden et al. 2021; Jatavallabhula et al. 2021; Liang et al. 2019; Qiao et al. 2020]. These contact models often require per-scene parameter tuning if complex contact scenarios are present, which makes these methods hard to use in optimization, especially shape optimization.

Our approach uses the recently proposed Incremental Potential Contact (IPC) formulation [Li et al. 2020], replacing the traditional zero-gap assumption [Belytschko et al. 2000; Bridson et al. 2002; Brogliato 1999; Daviet et al. 2011; Harmon et al. 2009, 2008; Kikuchi and Oden 1988; Otaduy et al. 2009; Stewart 2001; Verschoor and Jalba 2019; Wriggers 1995] with a smooth version ensuring a (small) non-zero separation between objects at every frame of the simulation. This approach was designed with the explicit goal of guaranteeing *robustness* and its smooth formulations of contact and friction avoids the need for handling non-smooth constraints.

Stupkiewicz et al. [2010] is one of the few papers that demonstrate sensitivity analysis of elastic problems with contact with respect to a range of parameters, including shape and material properties. This method, tested on a limited set of regular-grid problems, uses direct differentiation requiring a solve per parameter, and does not use a robust contact model.

We compare our solver, [Du et al. 2021], and [Jatavallabhula et al. 2021] in Section 10.5 in scenes involving both contact and self-contact.

**Shape and topology optimization with contact.** Historically shape optimization was primarily considered separately, e.g., for physical parameter or initial condition estimation, primarily in static settings, often with additional assumptions on bodies involved in contact.

Some previous works in this area have considered the specific case of optimization in the presence of contact between a soft body with fixed rigid surfaces [Beremlijski et al. 2014; Haslinger et al. 1986; Herskovits et al. 2000]. Other works, like ours, have studied the interaction of two or more deformable bodies in contact [Desmorat 2007; Maury et al. 2017; Stupkiewicz et al. 2010; Tozoni et al. 2021]. Most papers do not consider friction or use a simplified model (compared to the standard Coulomb formulation) as discussed by Maury et al. [2017].

Most closely related to our approach, Maury et al. [2017] presented a level set discretization technique where contact and friction were modeled with penalty terms, using smooth approximations to the problem. Using a similar contact and friction model, Tozoni et al. [2021] designed a shape optimization technique that focused on reducing stress of static assemblies that are held together by contact and friction. Both these works followed the mathematical model of contact presented by Eck et al. [2005], which allows for interpenetration and assumed that contact zones are fixed.

For the specific use case of avoiding sag due to gravity forces, Hsu et al. [2022] proposes a global/local approach to optimize the rest shape and initial displacement of input geometries to avoid the deformation introduced by gravity forces. This work uses the IPC contact model in some simulation examples, but does not use IPC in their optimization procedure.

Our approach supports dynamic simulation, allows contact zones to change with both optimization parameter changes and in the course of the simulation, and supports contact and self-contact between arbitrary deformable objects.

**Meshfree methods.** A number of differentiable simulation methods use meshfree discretizations. Especially for shape optimization, methods like XFEM [Hafner et al. 2019; Schumacher et al. 2018] and MPM [Hu et al. 2019b] that do not maintain conforming meshes are often considered to circumvent remeshing-induced discontinuities [Bächer et al. 2021]. However, these methods sacrifice accuracy [de Vaucorbeil et al. 2019], particularly for stress minimization problems [Sharma and Maute 2018]. Our approach computes accurate displacement and stressed by using a finite element method framework using high-order elements, coupled with dynamic remeshing to compensate for the distortion introduced by large deformations.

## 2.1 Choice of approach to computing gradients

A broad variety of approaches to differentiable simulation exist in the literature on optimal control, shape optimization, and inverse problems (see, e.g., [van Keulen et al. 2005] for a systematic overview); in this section, we briefly discuss the motivation for the design choices in our algorithm. Our choice is significantly influenced by the features of our problem setting:

- High dimension: e.g., shape and variable material property optimization may require thousands of parameters.
- Complex linear solvers: we aim to accurately solve highly nonlinear, time-dependent or static, stiff problems, requiring complex linear solvers for large sparse linear systems in the inner loop of nonlinear solvers.
- Contact: resolving contacts requires additional complex algorithms for continuous collision detection, in the nonlinear solver line searches.
- Large shape changes and deformations: shape differentiation often leads to large shape changes, which may require remeshing.

**Choice of the overall approach.** The two most general approaches are, in a sense, opposite extremes, but neither is a good fit for our setting.

*Finite difference* methods can be used with any black-box solver, but require an extra solve for each parameter, so it is not suitable for high-dimensional problems or even problems of moderate dimension (Table 6 compares the efficiency of our method and finite differences).

*Code differentiation* [Bischof and Bücker 2000; Griewank and Walther 2008; Margossian 2019; Naumann 2012] through overloading operators, or using a specialized language, has two fundamental problems, making it unsuitable for complex nonlinear codes with contact: it requires rewriting all of the simulation code, including supporting numerical libraries, e.g., sparse linear solvers and contact handling, and even more significantly is likely to produce unnecessarily inefficient code (fully differentiable sparse linear matrix inversion is going to be slow, and differentiating through a nonlinear solve is unnecessary, as we see below). While automatic code transformation in principle may eliminate the need to rewrite the code, and there is promising work [Jakob 2010; Moses et al. 2022] in this direction, we are unaware of fully automated tools capable of handling large software systems, and the concerns about the efficiency of the resulting code remain.

Existing differentiable solvers following this route use explicit time integration and/or a few iterations of an iterative linear solver. Both these options are unsuitable for applications requiring robustness and accuracy, limiting their applicability. For more details, we refer to Appendix E.3 of [Hu et al. 2019a], where the authors discuss that it is not realistic to differentiate stably a complex linear solver (the paper refers to a multigrid solver, but it is even more true for a sparse direct solver), so they use 10 Jacobi iterations to approximate the linear solve in the smoke simulation.

We opt for the approach based on *adjoint equations*, well established in scientific computing and optimal control, as described in Section 3. It is widely considered the most efficient approach to computing sensitivities, with the cost of a single additional linear solve per time step, and reusing important parts of the forward solver, at the expense of requiring derivations specific to a particular time-stepping algorithm. It allows us to implement efficient differentiability for solvers with all the features listed above.

**Fixed vs. changing discretization.** The adjoint method is particularly simple to apply to a purely algebraic problem, in which both the objective and PDE are discretized once, and then the problem is treated as a purely algebraic finite-dimensional optimization problem with PDE acting as a constraint. However, in our context, as shape optimization may change the domain, we cannot view the optimization problem as purely algebraic, as the discretization may change at every optimization step: both the forward and adjoint systems are rebuilt starting from a new discretization.

**Discretize-then-optimize vs optimize-then-discretize.** In the context of adjoint methods, we need to choose between the "discretize-then-optimize" approach and "optimize-then-discretize" [van Keulen et al. 2005]. In the first approach, the original PDE and objectives are converted to a discrete form which is then differentiated with respect to discrete optimization parameters. In the second approach, a PDE for the sensitivities is derived, and this PDE is discretized. The difference between these approaches is relatively small for differentiation with respect to material parameters, but more significant for shape derivatives. In this context, "optimize-then-discretize" is the most common approach: its convergence theory is better established, and directly follows from the discretization convergence. On a more practical side, it leads to a simpler form of adjoint equations for the shape derivatives formulated in the physical domain, enabling better reuse of the forward solver code. We refer to Section 2.3 in [Allaire et al. 2021] for additional discussion and to Appendix G for an example illustrating the differences for the Poisson problem. We emphasize that both approaches, for a suitable choice of discretization, lead to the same discrete solution; however, discretize-then-optimize in the context of shape optimization obscures the essential fact that the system matrix need not be recomputed. We use a specific discretization that ensures that the computed gradients are consistent with differentiating the discretized objective, as this simplifies the implementation of optimization algorithms.

[Dokken et al. 2020] uses the "discretize-then-optimize" approach to support shape derivatives in FEniCS, which has its own DSL. This approach allows one to support a broad range of PDEs but at the expense of higher complexity and significant additional performance overhead.

**Constructing adjoint equation components: AD vs analytic approach.** The adjoint method requires partial derivatives of the objective for the right-hand side of the adjoint system, and the stiffness and mass matrices for the adjoint PDE itself, which are similar to or coincide with those for the forward PDE. These can be computed using an AD method (note that the code to be differentiated is a straightforward algebraic computation, not a complex algorithm like a linear solver) or in closed form.

This can be done by transforming the code of assembling force vectors and computing objectives to an AD framework or applying code transformation to these parts of the code. However, AD leads to less reuse compared with the analytic case and higher computational complexity. We briefly compare these options in Section 10. We opt for doing extra analytical work to derive all derivatives explicitly, but the approaches can be combined - one can add additional forces or objectives using AD.

## 3 OVERVIEW

In Sections 4-9, we provide a self-contained description of our method. While this contains a mix of known and new material, we aim to present all components of the method in a unified and systematic notation to ensure reproducibility.

**Typographical conventions.** We use lower-case italic for functions $a(z)$ and variables $z$, with both $z$ and $a$ in $\mathbb{R}^D$, where $D = 2, 3$. Boldface lower-case letters ($\mathbf{a}$) are used for vectors of coefficients of a FEM (or any other) discretization of a function. For a vector or matrix quantity, superscripts are used to index whole vectors or matrices: e.g., $\mathbf{p}^i$ may denote $\mathbf{p}$ at time step $i$. Subscripts are used for the indices of components of a vector, e.g., $a(z) = \sum_{\ell=1}^n a_\ell \phi^\ell(z)$ means that the function $a(z) : \mathbb{R} \to \mathbb{R}^D$ is a linear combination of basis functions $\phi^\ell$, with coefficients $a_\ell$ which are components of $\mathbf{a}$. If $a(z)$ has values in $\mathbb{R}^D$, its coefficients in a scalar basis $\phi^\ell$ are $D$-dimensional, Then $\mathbf{a}$ is a vector of length $D \cdot n$, with $D$ coordinates of each component of $a_\ell$ in sequential entries.

**General problem form.** We solve static and dynamic optimization problems of the form

$$\min_q J(u, x, q), \text{ such that, } \mathcal{H}(u, x, q) = 0 \tag{1}$$

and

$$\begin{gathered} \min_q J(\mathbf{u}, \mathbf{q}) = \min_q \int_{t=0}^T J(\mathbf{u}, t, \mathbf{q}) \\ \text{such that } \rho \ddot{u} = \mathcal{H}(u, x, t, q) \text{ on } \Omega_{\bar{\mathbf{q}}},\ u(0) = g^u(q), \dot{u}(0) = g^v(q), \end{gathered} \tag{2}$$

where $J$ is an objective, possibly including constraints in penalty form, $u(x, t)$ is the displacement of a material point $x$ satisfying a static or dynamic physics equation, and $g^u$ and $g^v$ are the initial conditions for the displacements and velocities. In this work, we consider nonlinear elastic deformation, contact, friction, and damping forces. We assume the density $\rho$ to be constant in time. The optimization parameter functions $q = (\bar{\mathbf{q}}, \mathbf{q}^1, \ldots, \mathbf{q}^m)$ include all parameters of the system: material properties (elastic, friction, and damping), object shape, and initial and boundary conditions. The

Table 3. Notation.

| **Domains and bases** | |
|---|---|
| $D_d$ | Domain dimension, 2 or 3. |
| $D_s$ | Solution dimension, 1, 2 or 3. |
| $\Omega_{\text{ref}}$ | **Reference domain** $\Omega_{\text{ref}} \subset \mathbb{R}^{D_d}$ consists of copies of identical reference elements $\hat{K}_j$, $j = 1 \dots n_K$ identified along edges. |
| $\hat{x}_\ell$ and $\hat{z}_\ell$ | **Nodes** are points in $\Omega_{\text{ref}}$ used to define bases, $\ell = 1 \dots n_N^x$, and $1 \dots n_N^z$ respectively. *The set of nodes $\hat{z}_\ell$ does not include nodes with Dirichlet boundary conditions; the set of nodes $x_i$ does include these nodes.* |
| $\hat{\phi}^\ell$ and $\hat{\xi}^\ell$ | **FE basis functions** are scalar basis functions defined on $\Omega_{\text{ref}}$; $\hat{\xi}^\ell$ correspond to nodes $\hat{x}_i$, and is used for geometric maps (we use p.w. linear basis); $\hat{\phi}^\ell$ correspond to $\hat{z}_\ell$ and used for all other quantities (arbitrary order Lagrangian). |
| $\bar{q}$, $\bar{q}^j(y^j)$, $\bar{\mathbf{q}}$, $x_\ell$ | **Geometric map** $\bar{q}$ embedding a reference element in space, is defined on each $\hat{K}_j$ in $\Omega_{\text{ref}}$ with local coordinates $y^j$ as $\bar{q}^j(y^j) = \sum_\ell x_\ell \hat{\xi}^\ell(y^j)$, where $x_\ell \in \mathbb{R}^{D_d}$ are the positions of the nodes of the element $j$ forming the vector $\bar{\mathbf{q}}$. Concatenation of these maps yields the global geometric map $\bar{q} : \Omega_{\text{ref}} \to \mathbb{R}^{D_d}$. |
| $\Omega_{\bar{\mathbf{q}}}$ | **Physical domain** is the domain on which the PDE is solved, parametrized by $\bar{\mathbf{q}}$, $\Omega_{\bar{\mathbf{q}}} = \bar{q}(\Omega_{\text{ref}})$. The global coordinate on $\Omega_{\bar{\mathbf{q}}}$ is $x = x^{\bar{\mathbf{q}}} \in \mathbb{R}^{D_d}$. |
| $\phi^\ell(x)$,$\xi^\ell(x)$ | **FE bases on** $\Omega_{\bar{\mathbf{q}}}$**.** The bases $\hat{\phi}^\ell$ and $\hat{\xi}^\ell$ can be pushed forward to the domain $\Omega_{\bar{\mathbf{q}}}$ via $\phi(x) = \hat{\phi} \circ \bar{q}^{-1}(x)$ and $\xi(x) = \hat{\xi} \circ \bar{q}^{-1}(x)$. |
| $\Omega_{\bar{\mathbf{q}}+\boldsymbol{\theta} t}$ | **Perturbed domain** obtained using a perturbation direction $\boldsymbol{\theta}$ in $\bar{\mathbf{q}}$. Perturbation $\theta(x) \in \mathbb{R}^{D_d}$ is: $\theta = \theta(x) = \sum_\ell \theta_\ell \, \hat{\xi}^\ell \circ (\bar{q}^j)^{-1}(x) = \sum_\ell \theta_\ell \, \xi^\ell(x)$. |

| **Functions on physical domain** $\Omega_{\bar{\mathbf{q}}}$ | |
|---|---|
| $u_{\bar{\mathbf{q}}}(x)$,$\mathbf{u}$ | **PDE solution defined on** $\Omega_{\bar{\mathbf{q}}}$ with values in $\mathbb{R}^{D_s}$. We denote the vector of coefficients of $u$ in the FE basis $\phi$ by $\mathbf{u}$. $u(x) = \sum_\ell u_\ell \hat{\phi}^\ell \circ \bar{q}^{-1}(x) = \sum_\ell u_\ell \phi^\ell(x)$. |
| $w(x)$, $\psi(x)$,$\mathbf{w}$,$\boldsymbol{\psi}$ | **Test functions** (scalar) defined similarly to $u(x)$ in the same basis and vectors of their coefficients are $\mathbf{w}$ and $\boldsymbol{\psi}$. |
| $p(x)$,$\mathbf{p}$ | **Adjoint solution** is the solution of the adjoint equation and the vector of its coefficients, with values in $\mathbb{R}^{D_s}$. |
| $q^m(x)$, $\mathbf{q}^m$ | $m$**-th optimization parameter** $q^m(x) = \sum_{\ell=1}^{n_q^m} q_\ell^m \zeta^\ell(x)$ with a basis $\zeta^\ell$ with values in $\mathbb{R}^{D_q^m}$ parameters can be material properties, boundary conditions etc, defined on all or parts of $\Omega_{\bar{q}}$. For the geometry map $\bar{q}$, $\xi$ on $\text{Dom}(\bar{q}) = \Omega_{\text{ref}}$, and $\zeta^\ell = \xi^\ell$. |

| **PDE and derivatives** | |
|---|---|
| $\mathbf{h}(\mathbf{u},\mathbf{q}) = 0$ | **Discretized form of the PDE,** i.e., a system of $n_u$ algebraic equations with components of $\mathbf{u}$ as unknowns. |
| $J(\mathbf{u},\mathbf{q})$ | **Discretized form of the objective**. |
| $\partial_\mathbf{q} a(\mathbf{u},\mathbf{q})$ | **Derivative of a (possibly) vector quantity** $a$ **with respect to a vector of optimization parameters**, not including dependence through $u$. The vector is the vector of coefficients of one of $q^m$ or $\bar{q}$. If the dimension of $a$ is $n_a$, then $\partial_\mathbf{q}\mathbf{a}$ is a matrix of size $n_a \times D_q^m n_q^m$. |
| $\partial_\mathbf{u} a(\mathbf{u},\mathbf{q})$ | **Derivative of a quantity** $a$ **with respect to the the PDE solution** $u$; it is a vector of length $D_s n_u$. |
| $d_\mathbf{q} a(\mathbf{u},\mathbf{q})$ | **Full derivative of** $a$ **with respect to q, including through the dependence on** $u$**.** |
| $\nabla a(v)$, $\nabla_i a(v,w)$ | **Derivatives of** $a$ **with respect to arguments** $v, w \in \mathbb{R}^D$. |

first of these, $\bar{q}$ plays a special role: it determines the shape of the domain $\Omega_{\bar{\mathbf{q}}}$ on which the PDE is defined; it is a function on a reference domain $\Omega_{\text{ref}}$ defining its deformation. Parameters $q^i$ may be global constants, or dependent on the points of the reference domain, or pairs of points (as it is the case for the friction coefficient).

This problem statement is similar to [Geilinger et al. 2020] and other works on differentiable simulators; however, our goal is to support full differentiability, including shape, in a systematic way (see Table 1 for details) which affects the adjoint formulation and requires deriving expressions for a number of gradients of forces and functionals.

**Discrete problem.** We postpone the exact description of the discrete problem to Section 6. The discretized static problem obtained using FEM discretization has the general form:

$$\min_{\mathbf{q}} J(\mathbf{u},\mathbf{q}), \ \text{s.t.,} \ \mathbf{h}(\mathbf{u},\mathbf{q}) = 0, \tag{3}$$

where $\mathbf{u}$ is the vector of FE basis coefficients of $u$ and $\mathbf{q}$ is the concatenation of the vectors of coefficients of $\bar{\mathbf{q}}, \mathbf{q}^1, \dots, \mathbf{q}^m$.

The dynamic discretized problem with BDF of order $m$ discretization in time has the general form:

$$\begin{aligned}
&\min_{\mathbf{q}} J(\mathbf{u}, \mathbf{q}) = \min_{\mathbf{q}} \sum_{i=0}^{N} w_i J_i(\mathbf{u}^i, \mathbf{q}) \\
&\mathbf{u}^i + \sum_{j=1}^{\min(i,m)} \alpha^i_j \mathbf{u}^{i-j} = \beta_i \Delta t\, \mathbf{v}^i \\
&M\left(\mathbf{v}^i + \sum_{j=1}^{\min(i,m)} \alpha^i_j \mathbf{v}^{i-j}\right) = \beta_i \Delta t\, \mathbf{h}^i(\mathbf{u}^i, \mathbf{u}^{i-1}, \mathbf{q}) = \hat{\mathbf{h}}^i,
\end{aligned} \tag{4}$$

where $M$ is the mass matrix. The higher-order BDF schemes need to be initialized with lower-order steps; more specifically, $\alpha^i_j$ is $j$-th coefficient of BDF$i$, for $1 \leqslant i < m$, and $j$-th coefficient of BDF$m$ otherwise. In the formulation above, $\mathbf{h}(\mathbf{u}, \mathbf{q})$ does not depend on velocities $\mathbf{v}$. If the dependence on velocities is needed, as for damping forces, we discretize in time, and handle it as dependence on $\mathbf{u}$ at different time steps.

**Overview of the method.** We aim to present a complete, largely self-contained formulation, to ensure reproducibility as well as support easy addition of new types of forces. This requires restating briefly some of the known facts and formulas using our notation; we identify parts that are not present in previous work.

We first assume the discretized form of the problem (3) and (4), and derive consistent adjoint equations for the static and dynamic cases.

Each force and objective can be added to this general framework by deriving a set of matrices and vectors needed to compute partial force and objective derivatives.

We then proceed by computing these quantities analytically for the set of forces involved in our formulation, and a broad selection of functionals, including most used in the previous work both on differentiable dynamic simulation and shape optimization. We compute these in a form that allows for easy remeshing of $\Omega_{\text{ref}}$ and $\Omega_{\bar{\mathbf{q}}}$, which is necessary for the large changes in physical domain introduced by shape optimization.

## 4 ADJOINT-BASED OBJECTIVE DERIVATIVES

The derivatives of the objective $J$ with respect to optimization parameters can be computed efficiently using the classic adjoint method. While the basic principles of derivation are well-known, we show how these are applied in the context of our problem. The general form of our equations is similar to [Geilinger et al. 2020], which in turn is based on [Hahn et al. 2019] for the specific case of BDF2 time-stepping and material parameter differentiation. We derive the abstract form of the adjoint system for a general form of BDF time-stepping, and importantly we ensure that the dynamic adjoint solution is *consistent*, i.e., yields identical, rather than approximately identical, results to direct differentiation, as well as consider variable mass matrix needed for shape derivatives.

### 4.1 Static case

With the adjoint method, the gradient with respect to *any* number of parameters can be obtained by solving a single additional linear PDE (the adjoint PDE), and then evaluating an expression depending on this unknown. The adjoint PDE is obtained by considering the Lagrangian

$$\mathcal{L} = J(\mathbf{u}, \mathbf{q}) \qquad \{\text{objective term}\} \tag{5}$$

$$+\, \mathbf{p}^T\, \mathbf{h}(\mathbf{u}, \mathbf{q}) \qquad \{\text{physical constraint term}\} \tag{6}$$

and differentiating it with respect to the parameters $\mathbf{q}$:

$$d_{\mathbf{q}}\mathcal{L} = \partial_{\mathbf{q}} J + \partial_{\mathbf{u}} J\, d_{\mathbf{q}}\mathbf{u} + \mathbf{p}^T\, \partial_{\mathbf{q}}\mathbf{h} \ + \mathbf{p}^T\, \partial_{\mathbf{u}}\mathbf{h}\, d_{\mathbf{q}}\mathbf{u}. \tag{7}$$

$d_{\mathbf{q}}\mathcal{L}$ is expensive to compute if the dimension of $\mathbf{q}$ is large; a direct computation involves computing $d_{q_m}\mathbf{u}$ (how solution changes according to parameter $q_m$) for every optimized parameter $q_m$ in $\mathbf{q}$, which means solving $|q|$ different linear PDEs. Isolating all terms multiplying $d_{\mathbf{q}}\mathbf{u}$:

$$d_{\mathbf{q}}\mathcal{L} = \partial_{\mathbf{q}} J + \mathbf{p}^T\, \partial_{\mathbf{q}}\mathbf{h} + \left(\partial_{\mathbf{u}} J + \mathbf{p}^T\, \partial_{\mathbf{u}}\mathbf{h}\right) d_{\mathbf{q}}\mathbf{u}. \tag{8}$$

We can then eliminate the last term by choosing the *adjoint variable* $\mathbf{p}$ such that it solves *the adjoint problem*:

$$\mathbf{p}^T\, \partial_{\mathbf{u}}\mathbf{h} = -\partial_{\mathbf{u}} J. \tag{9}$$

Then, by plugging the solution $\mathbf{p}$ of the adjoint PDE into the Lagrangian, we obtain the final shape derivative:

$$d_{\mathbf{q}} J = d_{\mathbf{q}}\mathcal{L}(\mathbf{p}) = \partial_{\mathbf{q}} J + \mathbf{p}^T\, \partial_{\mathbf{q}}\mathbf{h}. \tag{10}$$

**Combining contributions from different forces and objectives together.** Our discretized equation has the form

$$\mathbf{h}(\mathbf{u}, \mathbf{q}) = \sum_k \mathbf{h}^k(\mathbf{u}, \mathbf{q}) = 0,$$

where $\mathbf{h}^k$ is a contribution from each type of force (elasticity forces, contact forces, etc). Similarly, the objective $J$ is a sum of contributions from several objective components or constraints in penalty form:

$$J(\mathbf{u}, \mathbf{q}) = \sum_\ell J^\ell(\mathbf{u}, \mathbf{q}).$$

Thus, the adjoint system and the full parametric derivative have the following form, respectively:

$$\begin{aligned}
\mathbf{p}^T\left(\sum_k \partial_{\mathbf{u}}\mathbf{h}^k\right) &= -\sum_\ell \partial_{\mathbf{u}} J^\ell, \\
d_{\mathbf{q}} J &= \sum_\ell \partial_{\mathbf{q}} J^\ell + \sum_k \mathbf{p}^T \partial_{\mathbf{q}}\mathbf{h}^k.
\end{aligned} \tag{11}$$

Thus, for each force, we need $\partial_{\mathbf{u}}\mathbf{h}^k$ and $\partial_{\mathbf{q}}\mathbf{h}^k$ and each objective component, $\partial_{\mathbf{u}} J^k$ and $\partial_{\mathbf{q}} J^\ell$.

### 4.2 Dynamic case

**Discrete time-dependent Lagrangian.** We write the time-dependent Lagrangian $\mathcal{L}$ for the functional $J$ viewing the equations for $\dot{\mathbf{v}}$ and $\dot{\mathbf{u}}$ as constraints with Lagrange multipliers $\mathbf{p}$ and $\boldsymbol{\mu}$.

Similar to the static case, we expand the derivative $d_{\mathbf{q}}\mathcal{L}$, and isolate the terms containing $d_{\mathbf{q}}\mathbf{u}$ and $d_{\mathbf{q}}\mathbf{v}$. By setting the sum of each of these two sets of terms to zero, we obtain two adjoint equations.

Our Lagrangian consists of three parts, corresponding to the objective ($J$), physics constraints ($\mathcal{L}_c$), and initial condition constraints ($\mathcal{L}_{in}$):

$$\mathcal{L}(\mathbf{u},\mathbf{v},\mathbf{p},\boldsymbol{\mu},\mathbf{q}) = J(\mathbf{u},\mathbf{q}) + \mathcal{L}_c(\mathbf{u},\mathbf{v},\mathbf{p},\boldsymbol{\mu},\mathbf{q}) + \mathcal{L}_{in}(\mathbf{u}^0,\mathbf{v}^0,\mathbf{p}^0,\boldsymbol{\mu}^0,\mathbf{q}),$$

where

$$\mathcal{L}_{in} = \mathbf{p}_0^T(\mathbf{v}^0 - \mathbf{g}^v) + \boldsymbol{\mu}_0^T(\mathbf{u}^0 - \mathbf{g}^u),$$

and

$$\mathcal{L}_c = \sum_{i=1}^{N} \mathbf{p}_i^T M\left(\mathbf{v}^i + \sum_{j=1}^{\min(i,m)} \alpha_j^i \mathbf{v}^{i-j} - \hat{\mathbf{h}}^i\right) + \boldsymbol{\mu}_i^T\left(\mathbf{u}^i + \sum_{j=1}^{\min(i,m)} \alpha_j^i \mathbf{u}^{i-j} - \beta_i \Delta t\, \mathbf{v}^i\right).$$

**Adjoint equations.** As shown in the Appendix, this leads to the following adjoint equations:

$$\begin{aligned}\left(\mathbf{p}_i + \sum_{j=1}^{\min(m,N-i)} \alpha_j^{i+j}\mathbf{p}_{i+j}\right) &= \beta_i \Delta t\, \boldsymbol{\nu}_i \\ M^T\left(\boldsymbol{\nu}_i + \sum_{j=1}^{\min(m,N-i)} \alpha_j^{i+j}\boldsymbol{\nu}_{i+j}\right) &= \\ (\partial_{\mathbf{u}^i}\hat{\mathbf{h}}^i)^T\mathbf{p}_i + (\partial_{\mathbf{u}^i}\hat{\mathbf{h}}^{i+1})^T\mathbf{p}_{i+1} - (\partial_{\mathbf{u}}\hat{J}^i)^T&,\end{aligned} \tag{12}$$

where we introduce a new variable $\boldsymbol{\nu}$ satisfying $\boldsymbol{\mu} = M^T\boldsymbol{\nu}$.

Note that this system is very similar to the forward time-stepping, with the following differences: it proceeds backward, from $\boldsymbol{\nu}_{i+1}$ to $\boldsymbol{\nu}_i$; there is a single *linear* solve per time step, rather than a nonlinear solve as for the forward system; for higher-order time stepping the first few steps in the forward system are lower-order BDF steps; however, this is *not* the case for the adjoint system: to maintain consistency, we derive the initial low-order steps from the forward system. If BDF2 is used for the forward time-stepping, the resulting scheme is different from the standard BDF2 scheme used in [Hahn et al. 2019] for the adjoint system. If the system were discretized inconsistently as in [Hahn et al. 2019], a sufficiently small time step is needed to maintain accuracy of the gradient that would ensure that the discrete energy decreases along the gradient direction.

By introducing $\mathbf{p}_{N+1},\ \boldsymbol{\nu}_{N+1}$, the initial condition can be simplified as

$$\begin{aligned}\mathbf{p}_{N+1} &= 0,\\ \boldsymbol{\nu}_{N+1} &= 0.\end{aligned} \tag{13}$$

The first (last in the adjoint solve) values need to be treated separately, as shown in Appendix A.2:

$$\boldsymbol{\mu}_0 = -(\partial_{\mathbf{u}}\hat{J}^0)^T - \sum_{j=1}^{m}\alpha_j^j\boldsymbol{\mu}_j + \mathbf{p}_1^T\partial_{\mathbf{u}^0}\hat{\mathbf{h}}^1,\ \ \mathbf{p}_0 = -\sum_{j=1}^{m}\alpha_j^j M^T\mathbf{p}_j. \tag{14}$$

**Computing the derivative of $J$ from the forward and adjoint solutions.** From the adjoint variables, we can compute $d_{\mathbf{q}}J = d_{\mathbf{q}}\mathcal{L}$:

$$\begin{aligned}d_{\mathbf{q}}J = &-\mathbf{p}_0^T\partial_{\mathbf{q}}\mathbf{g}^v - \boldsymbol{\mu}_0^T\partial_{\mathbf{q}}\mathbf{g}^u \\ &+ \sum_{i=0}^{N}\partial_{\mathbf{q}}\hat{J}^i \\ &+ \sum_{i=1}^{N} -\mathbf{p}_i^T\partial_{\mathbf{q}}\hat{\mathbf{h}}^i + \beta_i\Delta t\,\boldsymbol{\nu}_i^T d_{\mathbf{q}}M\mathbf{v}^i \\ &+ \sum_{j=1}^{m}\alpha_j^j\mathbf{p}_j^T d_{\mathbf{q}}M\mathbf{v}^0.\end{aligned} \tag{15}$$

Partial derivatives $\partial_{\mathbf{q}}\hat{\mathbf{h}}, \partial_{\mathbf{u}}\hat{\mathbf{h}}$ and $\partial_{\mathbf{q}}\hat{J}_i$, $\partial_{\mathbf{u}}\hat{J}_i$ are exactly the same as used in the construction of the system for static adjoint and computation of the functional. The differences, specific to time discretization, are:

- Mass matrix derivative $d_{\mathbf{q}}M$. See Appendix (section A.3).
- Partial derivatives of the initial conditions with respect to parameters $\partial_{\mathbf{q}}\mathbf{g}^v$ and $\partial_{\mathbf{q}}\mathbf{g}^u$, for positions and velocities. See Section A.4 in the Appendix. Typically, a 3D position and velocity for the whole object (or angular velocity for the object rotating as a rigid body) are used as parameters, so these are trivial to compute.

### 4.3 Summary of the parametric gradient computation

Computing the derivative $d_{\mathbf{q}}J$ requires the following components

- Derivatives $\partial_{\mathbf{u}}J_i$, $\partial_{\mathbf{u}}\mathbf{h}_i$, $\partial_{\mathbf{q}}J_i$ and $\partial_{\mathbf{q}}\mathbf{h}_i$ for each time step $i$. See Sections 8 to 9.2 for corresponding formulas.
- For the dynamic problems, $\partial_{\mathbf{q}}\mathbf{g}^u$ and $\partial_{\mathbf{q}}\mathbf{g}^v$, derivatives of the initial conditions. See Section A.4 in the Appendix.

To compute the parametric derivative of $J$, the steps are as follows:

1. Solve the forward system (3) or (4), and store the resulting solutions $\mathbf{u}$ for the static problem; for the dynamic problem, we store $\mathbf{u}^i, \mathbf{v}^i$, $i = 0 \ldots N$ at every step.
2. Initialize adjoint variables $\mathbf{p}_{N+1}, \boldsymbol{\nu}_{N+1}$ as shown in (13).
3. For the static problem, solve the adjoint system (9). For the dynamic problem, perform backward time stepping using (12).
4. At every step of the dynamic solve, evaluate derivative of the mass matrix $d_{\mathbf{q}}M$, if applicable, and use formulas (15) to update $d_{\mathbf{q}}J$.

## 5 OPTIMIZATION ALGORITHM

We provide a high-level summary of our method in Algorithm 1, its major components are:

- ForwardSolve solves the nonlinear elasticity system, retaining all solution steps for time-dependent problems;
- Objective computes the objective function given the solution and parameters;

- AdjointSolve solves the adjoint system (12) stepping backward in time and using the solutions of the forward problem;
- DiscreteDerivative computes gradients given displacements and adjoint variables;
- LineSearch is the standard Wolfe-Armijo line search, with additional prevention of element inversion and contact [Li et al. 2020];
- Remesh performs remeshing of $\Omega_{\text{ref}}$ and $\Omega_{\mathbf{q}}$ to improve the mesh quality before restarting optimization;
- Converged is the outer iteration stopping criterion.

We omit the pseudo-code for the forward solve as it closely follows that of [Li et al. 2020] with only a few notable changes: (1) we use an area weighting inside the barrier potential for convergence (see Section 8.2), (2) we use a fixed barrier stiffness $\kappa$ as changing it adaptively throughout the simulation would require computing its gradient through the update, and (3) to speed up convergence, we only project the Hessian to positive semi-definite in the Newton update if the unprojected direction is not a descent direction.

The inner loop works on a fixed mesh for $\Omega_{\text{ref}}$, and is close to the standard L-BFGS algorithm with two additional features, essential for handling shape derivatives and large deformations: (1) we check for any inversions of tetrahedra and contacts resulting from changes to the shape of the domain $\Omega_{\bar{\mathbf{q}}}$ as a result of changing shape parameters and (2) after each update of the boundary vertices, we call the SLIM smoothing algorithm [Rabinovich et al. 2017], with boundary vertices $p$ fixed, to move the interior vertices to improve mesh quality.

Unlike previous work we support remeshing. If the mesh quality $Q$ is smaller than a tolerance $\delta_{\text{remesh}}$, the domain is remeshed. If the gradient w.r.t. $\mathbf{q}$ is smaller than a tolerance $\delta_{\text{grad}}$ or the step size is smaller than a tolerance $\delta_x$, the optimization is stopped.

## 6 PHYSICAL MODEL AND DISCRETIZATION

In this section, we summarize the physical model we use. The model is similar to the one used in [Li et al. 2020], with some minor modifications to the friction and contact formulation (Section 8.2), most significantly, addition of damping.

To discretized the model we use arbitrary-order Lagrangian elements and arbitrary-order BDF time stepping (our experiments are with schemes of order 1 and 2).

The forces, which contribute to the PDE and need to be included in the adjoint equations and corresponding parametric gradient terms are:

- geometrically non-linear elasticity (with linear and Neo-Hookean constitutive laws as options);
- contact forces in smoothed IPC formulation;
- friction forces also in smoothed IPC formulation;
- strain-rate proportional viscous damping for elastic objects;

**Algorithm 1** Optimization algorithm overview

```
function Gradient($\mathbf{q}$)
    $\mathbf{u} \leftarrow$ ForwardSolve($\mathbf{q}$)
    $\mathbf{p} \leftarrow$ AdjointSolve(Objective, $\mathbf{u}$, $\mathbf{q}$)
    $\mathbf{g} \leftarrow$ DiscreteDerivative(Objective, $\mathbf{u}$, $\mathbf{p}$, $\mathbf{q}$)
    return $\mathbf{g}$
end function

function ParameterOptimization
    $\mathbf{q} \leftarrow$ initial parameter values
    $oi \leftarrow 0$                          ▷ Optimization iteration count
    repeat
        $\mathbf{g} \leftarrow$ Gradient($\mathbf{q}$)
        $\mathbf{d} \leftarrow$ LBFGSDirection($\mathbf{g}$, $\mathbf{q}$)
        $s \leftarrow$ LineSearch($\mathbf{d}$)
        $\mathbf{q} \leftarrow \mathbf{q} + s\mathbf{d}$
        if $Q < \delta_{\text{remesh}}$ then
            $\mathbf{q} \leftarrow$ Remesh($\Omega_{\mathbf{q}}$)
        end if
        $oi \leftarrow oi + 1$
    until $oi = oi_{\max}$ or $\|\mathbf{g}\| < \delta_{\text{grad}}$ or $\|s\mathbf{d}\| < \delta_x$
end function
```

- external forces such as gravity or surface loads.

The right-hand side of the system of equations we solve on $i$-th time step of (12) can be written as

$$\mathbf{h}^e(\mathbf{u}^i; \lambda(x), \mu(x)) + \mathbf{h}^c(\mathbf{u}^i) + \mathbf{h}^f(\mathbf{u}^i, \mathbf{u}^{i-1}; \mu(x, y)) \\ + \mathbf{h}^d(\mathbf{u}^i, \mathbf{u}^{i-1}; \alpha(x), \beta(x)),$$

where $\mathbf{h}^e$ is the discrete elastic PDE term, $\mathbf{h}^c$ and $\mathbf{h}^f$ define contact and friction forces, and $\mathbf{h}^d$ defines damping. In greater detail, all these forces are defined in the next section, along with $\partial_{\mathbf{u}}\mathbf{h}$ and $\partial_{\mathbf{q}}\mathbf{h}$ for each one of them.

The physical parameters $\mathbf{q}$ of the model with respect to which it can be differentiated include:

- (possibly spatially variant) Lame coefficients for elasticity $\lambda(x), \mu(x)$;
- friction coefficient between pairs of points $\gamma(x, y)$ (we consider it fixed for each pair of objects, to reduce the number of variables involved);
- damping coefficients $\alpha(x), \beta(x)$.

**Domains.** A critical aspect of the formulation at the foundation of our solver is the distinction between *reference domain* $\Omega_{\text{ref}}$, and (undeformed) *physical domain* $\Omega_{\bar{\mathbf{q}}}$, where $\bar{\mathbf{q}}$ denotes parameters defining the shape (Figure 2). The physics equations $\mathcal{H}(u, x, t, q)$ and the solution $u(x, t)$ is defined on $\Omega_{\bar{\mathbf{q}}}$ most naturally, but this domain may be changed by optimization. The optimization parameters $q$ are defined on $\Omega_{\text{ref}}$. This distinction is present in previous work on shape optimization (e.g., [Tozoni et al. 2021]) but not in the more general setting of dynamic differentiable simulation.

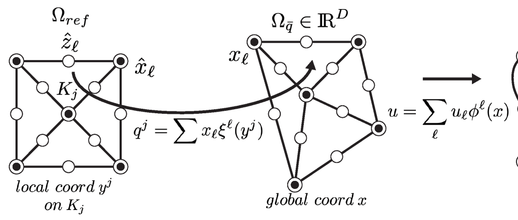
$\Omega_{ref}$
$\hat{z}_\ell$
$\hat{x}_\ell$
$K_j$
$\Omega_{\bar{q}} \in \mathbb{R}^D$
$x_\ell$
$q^j = \sum x_\ell \xi^\ell(y^j)$
$u(\Omega_{\bar{q}}) \in \mathbb{R}^D$
$u = \sum_\ell u_\ell \phi^\ell(x)$
local coord $y^j$ on $K_j$
global coord $x$

Fig. 2. Notation for domains and maps we use, see Table 3.

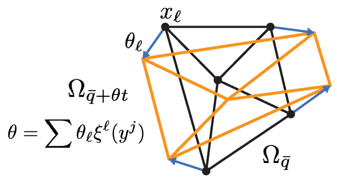
$x_\ell$
$\theta_\ell$
$\Omega_{\bar{q}+\theta t}$
$\theta = \sum \theta_\ell \xi^\ell(y^j)$
$\Omega_{\bar{q}}$

Fig. 3. Domain perturbation $\theta$, see Table 3.

## 7 EXAMPLE: POISSON EQUATION

To explain the principles of how individual derivatives for forces and target functionals are computed, we use a simple example. For more complex forces in our problem formulation, we state the final result in this paper, and we refer to the Appendix for the derivation.

Consider a variable-coefficient Poisson equation $\nabla \cdot (c(x)\nabla u) = f$ and zero Neumann boundary conditions on a domain $\Omega_{\bar{q}}$ that can be changed by the optimization. We take as the optimization objective the squared gradient of the solution on the domain. Then

- the optimization parameters are $q = [\bar{q}, c]$;
- The PDE in weak form is
$$\mathcal{H}(u, q, w) = \mathcal{H}(u, \bar{q}, c, w) = \int_{\Omega_{\bar{q}}} c\nabla u \nabla w - f w\, dx.$$
- The objective is
$$J(u, \bar{q}) = \int_{\Omega_{\bar{q}}} \|\nabla u\|^2 dx.$$

Discretizing in FE basis, with basis functions $\hat{\phi}^\ell$ (e.g., quadratic) used for $u = \sum_\ell u_\ell \hat{\phi}^\ell$ and $c = \sum_\ell c_\ell \hat{\phi}^\ell$, and basis $\hat{\xi}^\ell$ used for the geometric map $\bar{\mathbf{q}} = \sum_\ell x_\ell \hat{\xi}^\ell$, we obtain the following. (Note that both our basis $\hat{\xi}$ and $\hat{\phi}$ are defined on the fixed triangulated domain $\Omega_{\text{ref}}$.)

- $\mathbf{q} = [\bar{\mathbf{q}}, \mathbf{c}] = [x_1 \dots x_{n_N}, c_1 \dots c_{n_N}]$, where $x_\ell \in \mathbb{R}^2$ are vertices of the physical domain $\Omega_{\bar{\mathbf{q}}}$, which we optimize, and $c_\ell$ are the coefficients of $c$ in FE basis.
- The PDE discretization is performed on the physical domain $\Omega_{\bar{\mathbf{q}}}$, and has the form $\mathbf{h}(\mathbf{u}, \mathbf{q}) = S(\mathbf{q})\mathbf{u} - M(\mathbf{q})\mathbf{f}$. The entry $(m, \ell)$ of the matrix $S(\mathbf{q})$ are obtained by substituting $\mathbf{u} = \phi^m \circ g^{-1}$ and $w = \phi^\ell \circ g^{-1}$, and the discrete expression for $c$ into the expression below; entries of $M(\mathbf{q})$ are obtained in a similar way
$$S(u, w) = \int_{\Omega_{\bar{\mathbf{q}}}} c(\bar{\mathbf{q}}^{-1}(x))\nabla u \cdot \nabla w\, dx; \quad M(v, w) = \int_{\Omega_{\bar{\mathbf{q}}}} vw\, dx. \quad (16)$$
- The discrete objective is $J(\mathbf{u}, \mathbf{q}) = \mathbf{u}^T T(\mathbf{q})\mathbf{u}$, with entries of $T(\mathbf{q})$ also obtained by substituting pairs of basis functions into the bilinar form
$$T(u, w) = \int_{\Omega_{\bar{\mathbf{q}}}} \nabla u \cdot \nabla w\, dx. \quad (17)$$

Computing derivatives of $S$, $\partial_{c_k} S(u, w)$, with respect to $c$ is straightforward, as the dependence on the coefficients of $c$ is linear. Computation of shape derivatives is more complex, as the integration domain and the gradient operator $\nabla$ with respect to physical domain variables are affected by the change of shape parameters.

**Direct approach.** The direct approach is to perform a change of variables in (16) and (17) and to the domain $\Omega_{\text{ref}}$, and differentiate with respect to $x_\ell$; e.g.,(16) becomes
$$S(u, w) = \int_{\Omega_{\text{ref}}} c(y)\, \nabla_y \hat{u}^T (\nabla_y \bar{q})^{-1} (\nabla_y \bar{q})^{-T} \nabla_y \hat{w} \ \det \nabla \bar{q}\ dy,$$
where $\hat{u}$ and $\hat{w}$ denote compositions $u \circ \bar{q}^{-1}$. These expressions are highly nonlinear in $x_\ell$ and the final expressions for $\partial_{x_\ell} S(u, w)$ needed for $\partial_{\bar{\mathbf{q}}}\mathbf{h}$ are unwieldy, especially for more complex forces like nonlinear elasticity and friction.

**Shape derivative approach.** Instead, we use *shape derivative calculus* commonly used in shape optimization to obtain the derivatives with respect to the shape parameters directly on the physical domain $\Omega_{\bar{\mathbf{q}}}$ (for the parameters not affecting domain shape the approaches using $\Omega_{\text{ref}}$ and $\Omega_{\bar{\mathbf{q}}}$ are identical).

To compute $\partial_{\mathbf{q}} h$, or $\partial_{\mathbf{q}} J$, we consider the perturbed domain $\Omega_{\bar{\mathbf{q}}+\theta\epsilon}$, where $\boldsymbol{\theta}$ is a vector field, and compute the full derivative as limit of
$$\frac{1}{\epsilon}\Big(h(u_{\bar{\mathbf{q}}+\theta\epsilon}, \bar{\mathbf{q}} + \boldsymbol{\theta}\epsilon) - h(u_{\bar{\mathbf{q}}}, \bar{\mathbf{q}})\Big),$$
as $\epsilon \to 0$. In the resulting expression, the terms not containing the change $\delta u(x)$ correspond to $\partial_{\mathbf{q}} J\boldsymbol{\theta}$, and the terms containing derivatives of $u(x)$ are transformed to $\partial_{\mathbf{u}} J\boldsymbol{\psi}$ by substituting $\psi$ instead of $\delta u(x)$.

## 8 PARAMETRIC DERIVATIVES OF FORCES

In this section, we derive expressions for $\partial_{\mathbf{u}}\mathbf{h}$ and $\partial_{\mathbf{q}}\mathbf{h}$ for specific forces needed for the adjoint equations and the final derivative formula respectively.

For each force, we obtain expressions of the forms $B$ and $A$ below, from which the matrices for corresponding derivatives can be obtained using:
$$B^k(p, \theta) = \mathbf{p}^T \partial_{\mathbf{q}} \mathbf{h}^k\, \boldsymbol{\theta},\ A^k(p, \psi) = \mathbf{p}^T \partial_{\mathbf{u}} \mathbf{h}^k \boldsymbol{\psi}, \quad (18)$$
with $\theta$ going over basis vectors for this parameter type, $p$ going over adjoint variable components, and $\psi$ over the test function basis vectors for the adjoint; i.e., two matrices of size $D_s n_N^z \times D_s n_N^z$.

While nonlinear elasticity derivatives with respect to material parameters and initial conditions were used in [Geilinger et al. 2020] and [Hahn et al. 2019], and static-problem shape derivatives for a different (static, allowing interpenetration) contact and friction model were obtained in [Tozoni et al. 2021], we present expressions for all force-related derivatives with respect to all parameters (material, shape, initial conditions) in a unified way, simplifying adding additional forces, building whenever possible on a general form described in Section 8.1.

## 8.1 Volume forces

Many forces in continuum mechanics have the general weak form

$$\mathcal{H}^v(u, w, q) = \int_{\Omega_{\bar{\mathbf{q}}}} f^v(\nabla u, q) : \nabla w \, dx, \tag{19}$$

where $u$ is the displacement vector, with the components of the vector $\mathbf{h}^v(\mathbf{u})$ obtained as $\mathcal{H}^v(u, \phi^\ell, q)$, for all basis functions $\phi^\ell$, and the column denotes tensor contraction. In our case, elastic forces, irrespective of the constitutive law used, belongs to this category.

In these expressions $f^v(\nabla u, q)$ is a tensor of dimension $D_d \times D_s$; e.g., for elasticity, $D_d = D_s$, and this expression is the stress tensor, as a function of $\nabla u$.

If the force is associated with a volume energy density $W^v(\nabla u, q)$, associated forces have the form above, specifically, $f^v(\nabla u, q) = \nabla_1 W^v$. (Here, $\nabla_1$ means the gradient with respect to the first parameter, which in this case is $\nabla u$). For a surface energy density $W^s(u, q)$, the formulas are similar, but the integrals are over the surface.

We also formulate damping forces in a similar way, as explained in more detail below, except at each timestep $W^v$ depends on displacements $u^i$ and $u^{i-j}$, $j = 1 \dots m$ at the current and $m$ previous steps, where $m$ is the order of approximation of velocity used in damping (we use $m = 1$). The formulas for $A^v$ and $B^v$ in this case are obtained in exactly the same way as for the dependence on $u^i$ only, separately for $u^i$ and $u^{i-1}$, corresponding to $\partial_{\mathbf{u}_i}\mathbf{h}^i$ and $\partial_{\mathbf{u}_{i-1}}\mathbf{h}^i$ respectively.

To obtain matrices $A^v$ and $B^v$ corresponding to $\partial_{\mathbf{u}}\mathbf{h}^v$ and $\partial_{\mathbf{q}}\mathbf{h}^v$ (18), we split $\partial_{\mathbf{q}}\mathbf{h}^f$ into $\partial_{\bar{\mathbf{q}}}\mathbf{h}^f$ and $\partial_{\mathbf{q}^1}\mathbf{h}^f$, the shape and non-shape parameter derivatives, assuming $f$ depends on a single volume vector of parameters $q = \mathbf{q}^1$ (e.g., Lame constants). We treat these two types of parameters separately, as $\bar{\mathbf{q}}$ affects the domain of integration but not the integrand, and conversely, $q$ affects the integrand but not the domain.

**Shape derivatives.** For the shape derivative contribution, we obtain the following forms (the derivation and explicit form of matrix entries can be found in supplementary material).

$$\begin{aligned} B^v(\theta, p) = \int_{\Omega_{\bar{\mathbf{q}}}} & -f(\nabla u)\nabla\theta^T : \nabla p \\ & - (\nabla_1 f(\nabla u) : (\nabla u \nabla\theta)) : \nabla p + (f(\nabla u) : \nabla p)\nabla \cdot \theta \, dx, \end{aligned} \tag{20}$$

$B^v(\theta, p)$ is linear in $\theta$ and $p$, and we convert it to a matrix form by substituting basis functions for $\theta$ and $p$.

The contribution to the left-hand side of the adjoint equation is

$$A^v(\psi, p) = \int_{\Omega_{\bar{\mathbf{q}}}} (\nabla_1 f(\nabla u) : \nabla\psi) : \nabla p \, dx. \tag{21}$$

Observe that the matrix is identical to the matrix used in the forward solve.

**Non-shape volumetric parameter derivatives.** We assume that the force depends on $q = q(x)$, a function of the point in $\Omega_{\bar{\mathbf{q}}}$, defined by its values $\mathbf{q}$ at the same nodes as the solution, and interpolated using the same basis $\phi$.

In this case, the form $B$ is:

$$B^v(\theta, p) = \int_{\Omega} (\partial_q f \cdot \theta) : \nabla p \ dx.$$

The contribution to the left-hand side of the adjoint equation is identical to the shape derivative case.

In our implementation we consider two versions of elastic forces, both defined by Lame parameters specified as functions on $\Omega_{\text{ref}}$: $q(x) = [\lambda(x), \mu(x)]$. The only quantities we need are derivatives of $f(\nabla u)$ with respect to $\nabla u$, and material parameters.

**Linear elasticity.** For linear elasticity, we replace $f^v$ with

$$f^e(\nabla u, \mathbf{q}) = \sigma(\nabla u, \mathbf{q}) = C(\mathbf{q}) : \varepsilon(\nabla u) = \frac{1}{2} C(\mathbf{q}) : (\nabla u^T + \nabla u),$$

with $C_{ijkl}(\lambda, \mu) = \lambda\delta_{ij}\delta_{kl} + \mu(\delta_{ik}\delta_{jl} + \delta_{il}\delta_{jk})$.

For computing $A^e$ and $B^e$ we use partial derivatives of $f^e$ with respect to material parameters:

$$\begin{aligned} \nabla_1 f^e(\nabla u, \boldsymbol{\lambda}, \boldsymbol{\mu}) &= C, \\ \partial_\lambda f^e(\nabla u, \boldsymbol{\lambda}, \boldsymbol{\mu})_{ij} &= \delta_{ij}\delta_{kl}\varepsilon_{kl}, \\ \partial_\mu f^e(\nabla u, \boldsymbol{\lambda}, \boldsymbol{\mu})_{ij} &= (\delta_{ik}\delta_{jl} + \delta_{il}\delta_{jk})\varepsilon_{kl}. \end{aligned}$$

**Neo-Hookean elasticity.** For Neo-Hookean elasticity, the following formula is used for computing stress from the deformation gradient:

$$f^e(\nabla u, \mathbf{q}) = \mu(F(\nabla u) - Q(\nabla u)) + \lambda \log(\det(F(\nabla u)))\, Q(\nabla u),$$

where $F(\nabla u) = \nabla u + I$ and $Q(\nabla u) = F(\nabla u)^{-T}$.

We can then compute derivatives of $f(\nabla u)$:

$$\begin{aligned} \nabla_1 f^e(\nabla u, \mathbf{q})_{ijkl} &= \mu(\delta_{ik}\delta_{jl} + Q_{il}Q_{kj}) \\ &\quad + \lambda(Q_{ij}Q_{kl} - \log(\det(F))\, Q_{il}Q_{kj}), \\ \partial_\lambda f^e(\nabla u, \mathbf{q}) &= F(\nabla u) - Q(\nabla u), \\ \partial_\mu f^e(\nabla u, \mathbf{q}) &= \log(\det(F(\nabla u)))\, Q(\nabla u). \end{aligned}$$

**Damping.** For damping, we have material parameters controlling shear and bulk damping $\alpha, \beta$. We use the strain-rate proportional damping described in [Brown et al. 2018]. Given deformation gradient $F = \nabla u + I$, the Green strain tensor $E = \frac{1}{2}(F^T F - I)$ is rotation-invariant. The viscous Piola-Kirchhoff stress is of the form

$$P(\nabla u, \nabla \dot{u}) = F(2\alpha\dot{E} + \beta\, \text{Tr}(\dot{E})I),$$

where $\dot{E}$ denotes the time derivative, and the weak form of the corresponding force

$$\mathcal{H}^d(u, \dot{u}, w) = \int_{\Omega_{\bar{q}}} P(\nabla u, \nabla \dot{u}) \nabla w dx.$$

In our case, to fit this force into our differentiable formulation, we discretize $\dot{F}$ using as $\dot{F}^i = \frac{1}{\Delta t}(F^i - F^{i-1})$; this yields a force expression of the form

$$\mathcal{H}^d(u^i, u^{i-1}, w) = \int_{\Omega_{\bar{q}}} P(\nabla u^i, \nabla u^{i-1}) \nabla w dx,$$

which is identical to (19), except it depends on both $\nabla u^i$ and $\nabla u^{i-1}$. As a consequence, expressions for $A^d(\psi, p)$ and $B^d(\theta, p)$ are obtained in the same way as in (21) and (20), except two pairs of matrices are obtained, one for $\nabla u^i$ the other for $\nabla u^{i-1}$, using $\nabla_1 P$ and $\nabla_2 P$ as $\nabla_1 f$ respectively.

## 8.2 Contact and Friction

For the contact forces, we use a slightly modified version of the formulation of [Li et al. 2020]. While the original formulation is introduced in a discrete form, it can be derived with minimal changes as a linear finite-element discretization of a continuum formulation [Li et al. 2023a]. The contact incremental potential uses log barrier function $b(y)$, where $b$ is a truncated log barrier function, approaching infinity, if $y \to 0$, and vanishing for $y \geqslant \hat{d}$ for some small distance $\hat{d}$.

For any pair $k$ of primitives (vertices, edges, and faces) of the surface mesh $\partial\Omega_{\mathbf{x}^d}$, defined by the vertex positions $\mathbf{x}^d = M^* \bar{\mathbf{q}} + \mathbf{u}$, $d_k(\mathbf{x}^\mathbf{d})$ denotes the distance between them; $C$ is the set of primitive pairs in contact, i.e., pairs of primitives with $d_k < \hat{d}$.

Recall that the geometric map $\bar{q}$ always uses piecewise-linear elements $\xi_\ell$, while the basis for the deformations $u$ can be of any order. The matrix $M^*$ is an upsampling matrix to bring dimension of $\bar{\mathbf{q}}$ to the same as discrete solution $\mathbf{u}$. The upsampling is performed by linear interpolation from $\hat{x}_\ell$ to nodes $\hat{z}_\ell$.

The contact forces are derived from the following potential:

$$E(\mathbf{u}, \bar{\mathbf{q}}) = \kappa \sum_{k \in C} b(d_k(\mathbf{x}^\mathbf{d})) A_k = \sum_{k \in C} W_k(\mathbf{u}, \bar{\mathbf{q}}) A_k,$$

where $\kappa > 0$ is a parameter controlling the barrier stiffness and $A_k$ corresponds to the sum of surface areas associated with each primitive in $k$ (i.e., $\frac{1}{3}$ of the sum of areas of incident triangles for vertices and edges, and the area for triangles). See Section D in the Appendix.

We define $F_k^c(\mathbf{u}, \bar{\mathbf{q}}) = \partial_\mathbf{u} W_k(\mathbf{u}, \bar{\mathbf{q}}) = \kappa b'(d_k(\mathbf{x}^d)) \partial_{\mathbf{x}^\mathbf{d}} d_k$.

The contact force is given by

$$\mathbf{h}^c = \sum_{k \in C} F_k^c(\mathbf{u}, \bar{\mathbf{q}}) A_k.$$

The terms $B^c$ and $A^c$ have the form

$$B^c(p, \theta) = \sum_k \left( \partial_{\bar{\mathbf{q}}} F_k^c \theta \cdot p + F_k^c \cdot p \ \partial_{\bar{\mathbf{q}}} A_k \right) A_k,$$
$$A^c(p, \psi) = \sum_k \partial_\mathbf{u} F_k^c \psi \cdot p \ A_k,$$

where

$$\partial_\mathbf{u} F_k^c = \kappa (b''(\partial_{\mathbf{x}^\mathbf{d}} d_k)(\partial_{\mathbf{x}^\mathbf{d}} d_k)^T + b' \partial_{\mathbf{x}^\mathbf{d}}(\partial_{\mathbf{x}^\mathbf{d}} d_k)),$$
$$\partial_{\bar{\mathbf{q}}} F_k^c = \partial_\mathbf{u} F_k^c M^*$$

and $\partial_{\bar{\mathbf{q}}} A_k$ corresponds to the gradient of the area term, which varies depending on the type of primitive pairs corresponding to $k$. See Section D in the Appendix.

**Friction.** In general, the friction coefficient $\gamma(x_1, x_2)$ is a function of pairs of surface material points in $\partial\Omega_{\bar{\mathbf{q}}}$. As a simplification, in our implementation, we assume that each pair of objects $(m, n)$, in the simulation has a single coefficient $\gamma_{m,n}$, which can vary through the optimization. To simplify notation, we use $\gamma_{k_1,k_2}$ for a pair of primitives $k_1$ and $k_2$ to indicate the friction coefficient between objects these primitives belong to.

We follow the IPC definition of friction [Li et al. 2020]. Its key feature is that it is a differentiable function of displacements, which determine the contact forces, and relative velocities, which, for dynamic problems, we discretize using first-order approximation $u^i - u^{i-1}$, where $i$ is the time step.

The friction force for each active pair of primitives $k$ is

$$F_k^f(\mathbf{u}^{i-1}, \mathbf{u}^i) = -\gamma_{k_1,k_2} N_k T_k f_\eta(\|\tau_k\|) \frac{\tau_k}{\|\tau_k\|}, \tag{22}$$

where $N_k$ is the contact force magnitude, $T_k$ is a tangential frame matrix, constructed as described in [Li et al. 2020], and $\tau_k$ and $f_\eta$ are defined as

$$\tau_k = T_k(\mathbf{x}^{d,i-1})^T(\mathbf{u}^i - \mathbf{u}^{i-1}),$$
$$f_\eta(y) = \begin{cases} -\frac{y^2}{\eta^2} + \frac{2y}{\eta} & y \in [0, \eta) \\ 1 & y \geqslant \eta \end{cases}.$$

The total friction force has the form

$$\mathbf{h}^f = \sum_{k \in C} F_k^f(\mathbf{u}^i, \mathbf{u}^{i-1}, \bar{\mathbf{q}}) A_k,$$

with the form $B$ for shape derivatives given by

$$B^f(p, \theta) = \sum_k \partial_{\bar{\mathbf{q}}} F_k^f \theta \cdot p A_k + F_k^f \cdot p \ \partial_{\bar{\mathbf{q}}} A_k \ A_k.$$

Additional details on the computation of $\partial_{\bar{\mathbf{q}}} F_k^f$ are in the Appendix (Section E). The derivative with respect to friction coefficient values is easily obtained as the force is linear in friction coefficients. If $\mathbf{q}$ is a vector of friction coefficients,

$$\partial_{q_\ell} F_k^f = \begin{cases} -N_k T_k f_\eta(\|\tau_k\|) \frac{\tau_k}{\|\tau_k\|} & \text{if } q_\ell \text{ corresponds to } \gamma_{k_1,k_2} \\ 0 & \text{otherwise.} \end{cases}$$

Two forms $A^f$, for $\partial_{\mathbf{u}_i}$ and $\partial_{\mathbf{u}_{i-1}}$ are needed for the adjoint equation. Both have the general form

$$A^f(\psi, p) = \sum_k \partial_{\mathbf{u}} F_k \psi \cdot p \; A_k,$$

which reduces to computing the derivative of each $F_k$ term with respect to $u^i$ and $u^{i-1}$, which can be be found in Appendix E.

## 9 OBJECTIVE DERIVATIVES

In this section, we define the $\partial_{\mathbf{q}} J$ and $\partial_{\mathbf{u}} J$ terms needed for the gradient computation (10): For each objective-optimization parameter pair, $\partial_{\mathbf{q}} J^\ell \boldsymbol{\theta}$ and $\partial_{\mathbf{u}} J^\ell \boldsymbol{\psi}$, i.e., two vectors of size $D_s n_N^z$.

Similar to Section 8, we present all objective derivatives with respect to all types of optimization parameters, including shape in a unified way. We consider a comprehensive set of objectives used in many previous works, that can be easily extended with additional ones. In Section 9.1 we present general forms that all objectives can be reduced to.

### 9.1 General forms of objectives

Typically, objectives do not depend directly on the optimization parameters other than shape, so we focus primarily on derivatives of objectives with respect to shape parameters $\bar{\mathbf{q}}$ and solution $\mathbf{u}$.

We consider objectives of the form

$$J(\mathbf{u}, \bar{\mathbf{q}}) = J(J_1(\mathbf{u}, \bar{\mathbf{q}}), \dots J_{n_J}(\mathbf{u}, \bar{\mathbf{q}})), \tag{23}$$

where $J$ is a differentiable function, and $J_i$, $i = 1 \dots n_J$ are *objective terms* each of which typically has one of the integral forms described below. $J$ can be as simple $J(J_1) = J_1$, or can depend on several terms, as e.g., the center of mass optimization. The derivatives of objective are reduced to the the derivatives of the objective terms by a direct application of a chain rule, so we focus on these.

We first consider two general forms of objective terms which will be used for a number of specific objectives in Section 9.2. This includes inequality constraints in penalty form.

For each objective term $J^o$, we obtain vectors $R^o(\psi)$ and $S^o(\theta)$ corresponding to the partial derivatives $\partial_{\mathbf{u}} J^o$ and $\partial_{\mathbf{q}} J^o$, which are necessary to compute the adjoint solution and the full shape derivative. As for the derivatives of the objective vectors $\partial_{\mathbf{u}} J^o$ and $\partial_{\mathbf{q}} J^o$ are obtained by plugging in the basis functions $\phi_\ell$ int $R^o$ and $S^o$.

**Objectives depending on gradient of solution and shape.**

Consider an objective term that depends on both the solution of the PDE and the domain:

$$J^o(\nabla u, \bar{q}) = \int_{\Omega_{\bar{\mathbf{q}}}} j(\nabla u, x) dx. \tag{24}$$

In this case, as derived in the supplementary document,

$$S^o(\theta) = \int_{\Omega_{\bar{\mathbf{q}}}} -\nabla_1 j : \nabla u \, \nabla\theta + \nabla_2 j \cdot \theta + j \nabla \cdot \theta \; dx \tag{25}$$

and

$$R^o(\psi) = \int_{\Omega_{\bar{\mathbf{q}}}} \nabla_1 j : \nabla\psi \; dx. \tag{26}$$

**Objective terms depending on solution and shape.** We also use objective terms depending on both the solution of the PDE and the domain:

$$J^o(u, \bar{q}) = \int_{\Omega_{\bar{\mathbf{q}}}} j(u, x) dx. \tag{27}$$

In this case,

$$S^o(\theta) = \int_{\Omega_{\bar{\mathbf{q}}}} \nabla_2 j \cdot \theta + j \nabla \cdot \theta \; dx \tag{28}$$

and

$$R^o(\psi) = \int_{\Omega_{\bar{\mathbf{q}}}} \nabla_1 j \cdot \psi \; dx. \tag{29}$$

### 9.2 Specific objectives

$L_p$ **norm of stress.** For $p = 2$ this objective measures the overall average stress, and for high $p$, $L_p$-norm of stress approximates maximal stress:

$$J^\sigma = \left( \int_{\Omega_{\bar{\mathbf{q}}}} \|\sigma(\nabla u)\|_F^p dx \right)^{1/p}, \tag{30}$$

where $\sigma(\nabla u) = f(\nabla u)$ represents stress, which depends on $\nabla u$. Following the chain rule, this objective is a function of a single objective term $J^\sigma = (J_1^\sigma)^p$ which is of the form (24). with $j = \|\sigma(\nabla u)\|_F^p$ for which $\nabla_2 j = 0$, and

$$\nabla_1 j = p \, \|\sigma\|^{p-2} \; \sigma \; : \; \nabla f(\nabla u).$$

**Weighted difference from target deformations.**

$$J^{trj}(x, u) = \int_{\Omega_{\bar{\mathbf{q}}}} w(\bar{q}^{-1}(x)) \; \|x^d - x^{trg}(\bar{q}^{-1}(x))\|^2 \; dx \tag{31}$$

where $x^d = x + u$, the deformed state of the object, weight $w$ determines relative importance of points, and $x^{trg}$ is the target configuration, defined as function on $\Omega_{\text{ref}}$.

The formulas for the general objective (27), apply, with

$$\nabla_1 j = \nabla_2 j = 2w(\bar{q}^{-1}(x))(x^d - x^{trg}(\bar{q}^{-1}(x)).$$

If we define only the shape on the boundary as the target, then we have:

$$J^{btrj} = \int_{\partial\Omega_{\bar{\mathbf{q}}}} w(\bar{q}^{-1}(x)) \; \|x^d - x^{trg}(\bar{q}^{-1}(x))\|^2 \; dx$$

. Formulas for the derivatives are similar:

$$S^{btrj} = \int_{\partial\Omega_{\bar{\mathbf{q}}}} \nabla_2 j \cdot \theta + j(u, x) \, \nabla_s \cdot \theta \; dx,$$

$$R^{btrj} = \int_{\partial\Omega_{\bar{\mathbf{q}}}} \nabla_1 j \cdot \psi \; dx,$$

where $\nabla_s$ denotes the surface derivative.

**Target center of mass trajectory.** A related objective is the deviation of the center of mass of the object from a target trajectory.

$$J^{ctr}(J^P, J^D) = \left\| \frac{J^P}{J^D} - x^{ctr} \right\|^2 = \left\| \frac{\int_{\Omega_{\bar{q}}} \rho(x)\, x^d\, dx}{\int_{\Omega_{\bar{q}}} \rho(x)\, dx} - x^{ctr} \right\|^2 = \sum_i^{D_d} \left( \frac{J_i^P}{J^D} - x_i^{ctr} \right)^2. \tag{32}$$

Using the chain rule, we can reach a formulation where $S^{ctr}$ and $R^{ctr}$ depend on respective derivatives from each $J_i^P$ and $J^D$:

$$S^{ctr} = \sum_i (\partial_1 J^{ctr})_i S_i^P + \partial_2 J^{ctr} S^D,$$
$$R^{ctr} = \sum_i (\partial_1 J^{ctr})_i R_i^P + \partial_2 J^{ctr} R^D.$$

We then need to compute shape derivative and adjoint terms for both of our scalar integrals $J_i^P$ and $J^D$, following general formulas for 27. For each $J_i^P$, we have:

$$\nabla_1 j = \nabla_2 j = \rho(x) e_i,$$

where $e_i \in \mathbb{R}^{D_d}$ is a vector with 0s everywhere except at index $i$, where the value is 1.

Finally, assuming that densities are constant per point, for $J_D$,

$$\nabla_1 j = \nabla_2 j = 0.$$

**Height.** This functional aims to maximize the height of the center of mass:

$$J^{z_{\max}} = -\frac{\int_{\Omega_{\bar{q}}} \rho(x) x_z^d dx}{\int_{\Omega_{\bar{q}}} \rho(x) dx}, \tag{33}$$

where $u_z$ is the z (vertical) component of the solution (displacement) $u$, $x_z$ is the z component of the original position x. We can rewrite this formula using $J_z^P$ and $J^D$ from previous subsection:

$$J^{z_{\max}}(J_z^P, J^D) = -\frac{J_z^P}{J^D}. \tag{34}$$

This way, similar to $J^{ctr}$, we have:

$$S^{z_{\max}} = \partial_1 J^{z_{\max}} S_z^P + \partial_2 J^{z_{\max}} S^D,$$
$$R^{z_{\max}} = \partial_1 J^{z_{\max}} R_z^P + \partial_2 J^{z_{\max}} R^D.$$

Then, as for previous case, we can compute $S_z^P$, $R_z^P$, $S^D$ and $R^D$ through general formula 27, using $\nabla_1 j = \nabla_2 j = \rho(x) e_z$ for $J_z^P$ and $\nabla_1 j = \nabla_2 j = 0$ for $J^D$.

**Upper bound for volume.** A constraint on the volume of the optimized object in penalty form is

$$J^V = \varphi(V(\Omega_{\bar{q}}) - V_t), \tag{35}$$

where $V$ corresponds to ($\int_{\Omega_{\bar{q}}} dx$), the volume of shape $\Omega_{\bar{q}}$, $V_t$ to the target volume, and $\varphi(z)$ is a quadratic penalty function equal to $z^2$ for positive $z$ and zero for negative $z$. This functional reduces to the general objective (27), with $\nabla_1 j = \nabla_2 j = 0$, since $j(u, x) = 1$.

**Upper bound for stress.** Similarly, we can impose an approximate upper bound on stress via a penalty:

$$J^{\sigma_t} = \int_{\Omega_{\bar{q}}} \varphi(\|\sigma\| - s_t) dx, \tag{36}$$

where $s_t$ is the stress magnitude target. As for $L_p$ stress energy, our integrand $\varphi(\|\sigma\| - s_t)$ depends only on $\nabla u$ and (24) applies with

$$\nabla_1 j = \varphi' \frac{f(\nabla u)}{\|\sigma\|} : \nabla f(\nabla u),$$
$$\nabla_2 j = 0.$$

## 9.3 Regularization terms

In addition to the physical objectives described in the previous sections, we use two discrete regularization terms essential for numerical stability for a number of problems.

**Scale-invariant smoothing.**

$$J^{\text{smooth}} = \sum_{i \in B} \|s_i\|^p, \qquad s_i = \frac{\sum_{j \in N(i) \cap B} (v_i - v_j)}{\sum_{j \in N(i) \cap B} \|v_i - v_j\|}, \tag{37}$$

where $B$ contains the indices of all boundary vertices, $N(i)$ contains the indices of all neighbor vertices of vertex $i$, and $v_i$ is the position of vertex $i$. The value of $p$ can be adjusted to obtain smoother surfaces at the cost of less optimal shapes, normally we use $p = 2$. This term is scale-invariant and pushes the triangles/tetrahedra of the mesh toward equilateral. The derivative of this smoothing term with respect to optimization parameters $v_i$ can be seen in the first paragraph of Appendix F.

**Material parameter spatial smoothing.**

$$J^{\lambda,\mu \text{ smooth}} = \sum_{t \in T} \sum_{t' \in Adj(t)} \left(1 - \frac{\lambda_{t'}}{\lambda_t}\right)^2 + \left(1 - \frac{\mu_{t'}}{\mu_t}\right)^2, \tag{38}$$

where $T$ is the set of all triangles/tetrahedra, $Adj(t)$ is the set of triangles/tetrahedra adjacent to $t$. $\lambda, \mu$ are the material parameters defined per triangle. The derivative of this term can be seen in the last part of Section F (Appendix).

## 10 RESULTS

We partition our results into three groups depending on the type of the dofs used in the objective function: shape (Section 10.2), initial conditions (Section 10.3), or material (Section 10.4). For each group, we provide a set of examples of static and dynamic scenes of increasing complexity. In Section 10.5, we compare our solver, [Du et al. 2021], and [Jatavallabhula et al. 2021] to evaluate the effect of different material and contact models. We also compare against a baseline implementation using finite differences. We run our experiments on a workstation with a Threadripper Pro 3995WX with 64 cores and 512 Gb of memory. For a selection of problems, we validate our results with physical experiments using items fabricated in silicon rubber (we use 1:1 SMOOTH-ON OOMOO 30 poured into a 3D printed PVA mold) or 3D printed PLA plastic.

We additionally provide a video showing the intermediate optimization step for all the results in the paper as part of our additional material.

**Statistics.** We provide statistics for our experiments in Table 4, including the size of the meshes, material model, running time, and memory used.

We observe that the time to compute the gradients of the objective function is negligible compared to the forward solve time (usually less than 10%). This implies that as long as a physical system can be simulated in PolyFEM, our approach enables optimizing functionals depending on it with a comparable running time per optimization iteration.

We recall that the gradient computation requires solving one linear system for each time step of the forward simulation. For linear problems, the system to solve has the same stiffness matrix and we can thus reuse the factorization. For non-linear problems requiring Newton iterations, the forward step requires multiple Netwon steps, while the solve for the gradient is always a single linear system solve.

An additional acceleration strategy that we employ is noting that the optimization algorithm needs to solve many, often similar, forward simulations. We thus initialize, for non-linear problems, the forward solver with the solution at the previous step, which is often a good initialization.

**Color Legend.** We use green arrows to indicate Neumann boundary conditions, and black squares to indicate nodes that have a Dirichlet boundary condition. To reduce clutter, we use a uniform gray to indicate objects with a uniform Dirichlet boundary condition on all nodes.

To avoid singularities in the optimization we add, to the objective function, a boundary smoothing term (37) in all our shape optimization experiments, and a material regularization term (38) to all our material optimization experiments.

## 10.1 Implementation

**FE Solver.** We implemented our solver in C++ using the PolyFEM library [Schneider et al. 2019] for the forward solve, the IPC Toolkit [Ferguson et al. 2020] for computing contact and friction potentials, and Pardiso [Alappat et al. 2020; Bollhöfer et al. 2019, 2020] for solving linear systems.

**Optimization.** Our optimization algorithm (Algorithm 1) uses the L-BFGS implementation in [Wieschollek 2016], with backtracking line search.

**Remeshing.** Shape optimization might negatively affect the element shape, and for large deformation introduce close to singular elements that force the optimization to take tiny steps. After every optimization iteration, we evaluate the element quality using the scaled Jacobian quality measure [Knupp 2001], and optimize the mesh if it is below a threshold experimentally set to $10^{-3}$.

For 2D examples, we keep the mesh boundary fixed and we regenerate the interior using GMSH [Geuzaine and Remacle 2009]

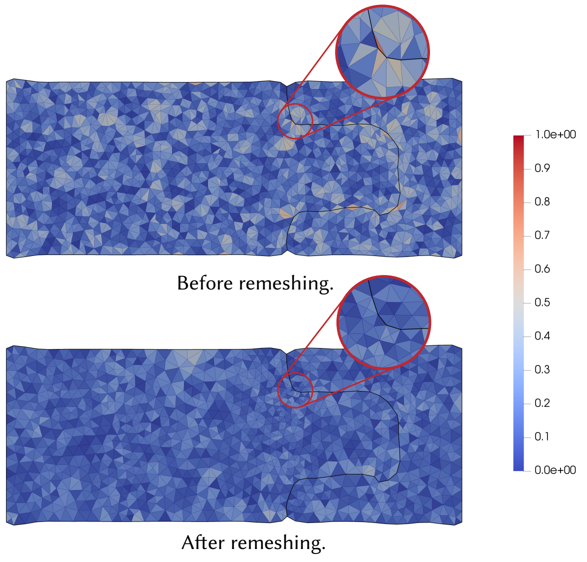

Fig. 4. An example of remeshing in the shape optimization. The quality is shown for each triangle. Triangles with bad quality have higher values.

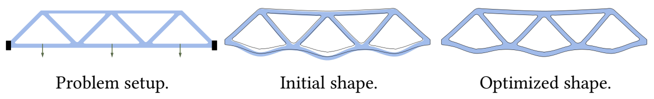

Fig. 5. **Static: Bridge With Fabricated Solution.** The result of the shape optimization (blue surface) matches the target shape (wire-frame).

(Figure 4). For 3D examples, we similarly fix the boundary and then use the mesh optimization procedure of fTetWild [Hu et al. 2020] to improve the quality of the interior until its quality is above the threshold.

The reason why we can remesh without damaging the optimization convergence is that our optimization objectives have little dependence on interior node positions. The objectives are in the form of an integral over the domain or boundary, so remeshing only leads to small errors due to projections between the meshes.

The reason for fixing the boundary in the remeshing is that our optimization objectives (Section 9.1) often depend on quantities on the boundary vertices: if the boundary is remeshed, we will need a bijective map between the two boundaries. Meshing methods providing this map exist [Jiang et al. 2020], but their integration in our framework, while trivial from a formulation point of view, is an engineering challenge that we leave as future work.

**Reproducibility.** The reference implementation of our solver and applications will be released as an open-source project.

## 10.2 Shape Optimization

We start our analysis with shape optimization problems both without and with contact or friction forces.

Table 4. Columns from left to right are: example names, number of vertices, degree of freedom of the simulation, physical formulation, objective functional of the optimization, total running time (sec), peak memory (Mb), number of iterations of the optimization, average running time of the simulation (sec), average running time of computing gradients (sec), total number of Newton iterations (linear solves) in the simulation, number of Newton solves in the simulation.

| Example | Vertices | Dofs | Model | Objective | Total time | Memory | Iter | Solve time | Grad time | Newton Iter. | Newton Solve |
|---|---|---|---|---|---|---|---|---|---|---|---|
| Bridge (Figure 5) | 4641 | 9282 | Linear | Target | 16.1 | 162.3 | 55 | 0.0343 | 0.0296 | 0 | 0 |
| Bridge (Figure 6) | 18598 | 143378 | Linear | Stress | 1665.8 | 1690.8 | 402 | 1.3859 | 0.1861 | 0 | 0 |
| 3D Beam (Figure 7) | 9939 | 209409 | NeoHookean | Stress | 95738.6 | 101786.3 | 171 | 192.1587 | 37.2651 | 1083 | 361 |
| Interlocking (Figure 8) | 1290 | 9946 | IPC | Stress | 303.3 | 188.5 | 101 | 0.8394 | 0.0590 | 4900 | 335 |
| 2D Hook (Figure 9) | 1760 | 13348 | IPC | Stress | 220.5 | 726.5 | 60 | 1.7224 | 0.0802 | 2548 | 126 |
| 3D Hanger (Figure 10) | 4190 | 80412 | IPC | Stress | 14129.4 | 6554.0 | 29 | 204.2374 | 3.2117 | 4708 | 64 |
| Bouncing Ball (Figure 11) | 73 | 146 | IPC | Target | 961.7 | 29.2 | 202 | 1.1061 | 0.0898 | 211611 | 41200 |
| Sliding Ball (Figure 12) | 526 | 6849 | IPC | Stress | 1610.1 | 2184.6 | 29 | 24.3086 | 1.2580 | 0 | 0 |
| Shock Protection (Figure 13) | 53879 | 107758 | IPC | Stress | 33301 | 10100 | 9 | 1264.395 | 129.96 | 35553 | 4800 |
| Puzzle Piece (Figure 14) | 370 | 740 | IPC | Trajectory | 47.4 | 107.6 | 19 | 1.5877 | 0.2129 | 2917 | 630 |
| Throw Bunny (Figure 1) | 2174 | 6522 | IPC | Target | 602.0 | 3344.1 | 9 | 209.2998 | 4.3731 | 15324 | 1000 |
| Colliding Tentacles (Figure 15) | 6896 | 20688 | IPC | Trajectory | 13070 | 8325 | 5 | 2043 | 41.25 | 14447 | 720 |
| Sine (Figure 16) | 651 | 1302 | Linear | Target | 0.3 | 34.4 | 12 | 0.0042 | 0.0022 | 0 | 0 |
| Bridge (Figure 17) | 18598 | 37196 | Linear | Target | 32.7 | 655.2 | 39 | 0.1416 | 0.0398 | 0 | 0 |
| Cube (Figure 18) | 4631 | 103383 | NeoHookean | Target | 455.8 | 6316.6 | 8 | 37.9947 | 2.6101 | 33 | 11 |
| Micro-Structure (Figure 19) | 3268 | 9804 | IPC | Target | 602.3 | 33502.3 | 11 | 42.0954 | 0.0746 | 249 | 14 |
| Kangaroo (Figure 20) | 231 | 462 | IPC | Trajectory | 21.6 | 224.6 | 6 | 1.6704 | 0.1624 | 2987 | 660 |
| Sliding Bunny (Figure 21) | 5682 | 17046 | IPC | Target | 11734.0 | 2304.3 | 8 | 547.3644 | 1.6478 | 61517 | 880 |
| Bouncing Ball (Figure 22) | 720 | 1440 | IPC | Height | 612.3 | 86.4 | 79 | 3.3482 | 0.2003 | 33609 | 5160 |
| Bouncing Ball (Figure 23) | 646 | 1938 | NeoHookean | Trajectory | 206.3 | 152.8 | 24 | 3.0548 | 0.7396 | 3264 | 1632 |
| Bouncing Ball (Figure 23) | 1251 | 3753 | IPC | Trajectory | 10546.6 | 1547.0 | 49 | 113.4214 | 8.8056 | 105401 | 20160 |

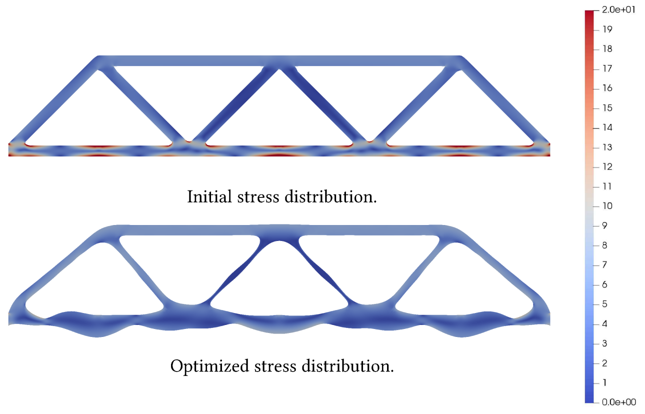

Fig. 6. **Static: Bridge.** Result of shape optimization to minimize the average stress.

**Static: Bridge With Fabricated Solution.** We fabricate a 2D solution to verify the correctness of our formulation and implementation. Starting from the shape of a bridge (Figure 5) we run a forward linear elasticity simulation with the two sides fixed and gravity forces. We now perturb the geometry of the rest pose and solve a shape optimization problem to recover the original rest pose, i.e. we remove the perturbation we introduced by minimizing the objective in (31).

**Static: Bridge.** We use the same model for a more challenging problem (Figure 6): we use the same Dirichlet conditions and material model, replace the gravity forces by 3 Neumann conditions on the lower beams, and minimize the $L^8$ norm of stress (30). To avoid trivial solutions we add a constant volume constraint (Section 9.2). The maximum stress is reduced from 68.789 to 22.232.

**Static: 3D Beam.** Moving to 3D (Figure 7), we perform static optimization of the $L^8$ norm of stress using Neo-Hookean materials on a beam standing on a fixed support at the center (nodes on the bottom surface of the beam have zero Dirichlet boundary conditions), and with two side loads applied as Neumann boundary conditions. We use (35) to bound the volume of the beam during optimization in order to avoid trivial solutions. The maximum stress is reduced from 3,377 to 920. Note that this scene is not using contact, the lower region of the central part of the beam is fixed with Dirichlet boundary conditions.

**Static: Interlocking.** Our framework supports contact and transient friction forces between objects without requiring explicit definition of contact pairs. We borrow the experimental setup used in [Tozoni et al. 2021]: we optimize the shape of two interlocking 2D parts (Figure 8) to minimize the $L^8$ norm of the stress (30). The bottom part is fixed and a force pointing down-right is applied to the top. Figure 8 shows how the shape changes to reduce the maximum stress from 3.2 Pa to 0.29 Pa.

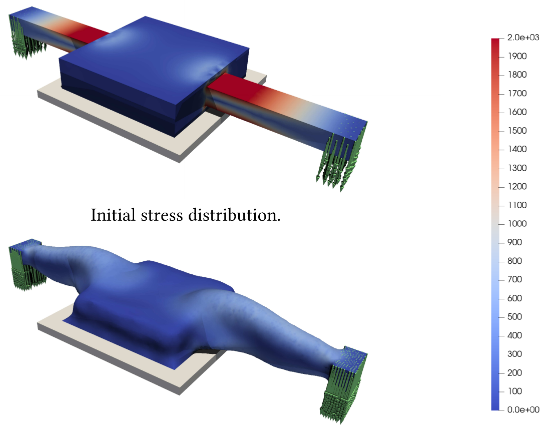

Initial stress distribution.

Optimized stress distribution.

Fig. 7. **Static: 3D Beam.** Result of stress minimization on a beam standing on a platform, with two loads on its sides.

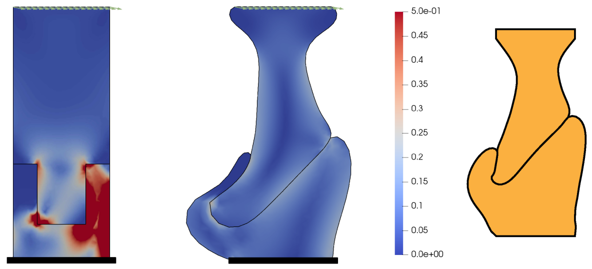

Initial stress distribution.

Optimized stress distribution.

[Tozoni et al. 2021].

Fig. 8. **Static: Interlocking.** Result of shape optimization to minimize the $L^8$ norm of stress.

Note that unlike [Tozoni et al. 2021], our contact model does not support overlapping boundary nodes, which are used in [Tozoni et al. 2021] to keep the contact over the optimization. To mimic this behaviour in our setting, we create small displacements on the overlapped boundary nodes along the normal directions as the initial guess for the forward simulation, so that each object is shrinked by a tiny amount and there is no overlap in the initial guess.

We note that our result is expected to be different from [Tozoni et al. 2021], as the contact models are different and the solutions of these problems are in general not unique. Despite their differences, we observe in both cases a reduction in maximal stress of similar magnitude (around 10 times reduction).

**Static: 2D Hook.** To physically validate our shape optimization results we reproduce the experiment in [Tozoni et al. 2021, Figure 21], where a hook is optimized to minimize the maximum stress (30) when a load is applied to one of its ends (Figure 9). The grey block is fixed with zero Dirichlet conditions on all nodes. We physically validate that the optimized shape is able to withstand a load of over 3× the unoptimized shape before breaking (Figure 9). The hook

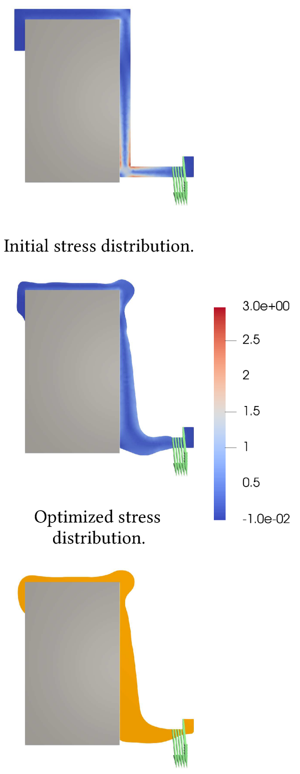

Initial stress distribution.

Optimized stress distribution.

Optimization result from [Tozoni et al. 2021]

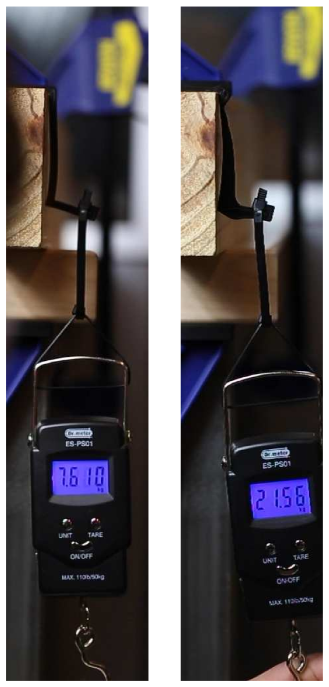

Fig. 9. **Static: 2D Hook.** Shape optimization of a hook to reduce stress concentration (left). Fabricated results with maximum load before failure (right).

has been fabricated using an Ultimaker 3 3D printer, using black PLA plastic. Despite the different contact model, the result is quite similar to the one presented in [Tozoni et al. 2021]: our approach has the advantage of not requiring manual specification of the contact surfaces.

**Static: 3D Hanger.** We also reproduce the experiment [Tozoni et al. 2021, Figure 29]: a coat hanger is composed of two cylinders and a hanger keeping the together. The shape of the hanger is optimized to minimize the maximum internal stress (30) when two loads are applied on its arms (Figure 10). The maximal stress is reduced from 89.93 Pa to 25.74 Pa. When comparing with [Tozoni et al. 2021], we observe a similar optimized shape and an equivalent stress reduction rate (around 3 times).

**Transient: Bouncing ball.** As a demonstration of shape optimization in a transient setting, we run a forward non-linear simulation of a ball bouncing on a plane and use its trajectory as the optimization goal (32). We then deform the initial shape into an ellipse and try to recover the original shape (Figure 11).

**Transient: Shock Protection.** We optimize the shape of a shock-protecting microstructure from [Shan et al. 2015] so that the stress

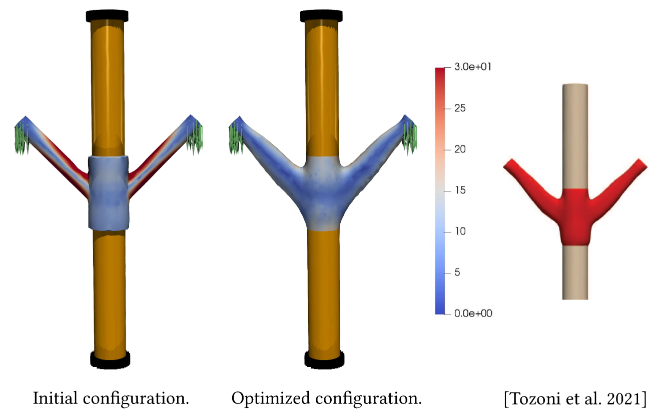

Fig. 10. **Static: 3D Hanger.** Result of shape optimization of a hanger to reduce stress concentration.

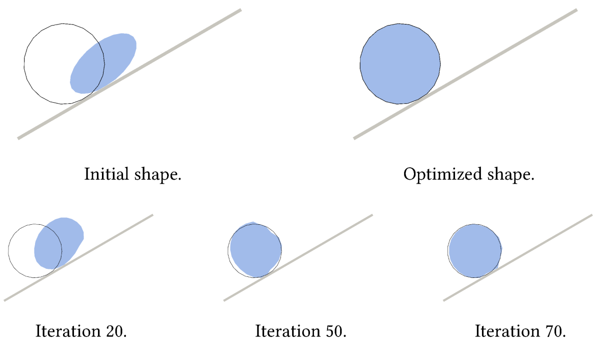

Fig. 11. **Transient: Bouncing ball.** The result of the shape optimization (blue surface) matches the desired trajectory (wire-frame).

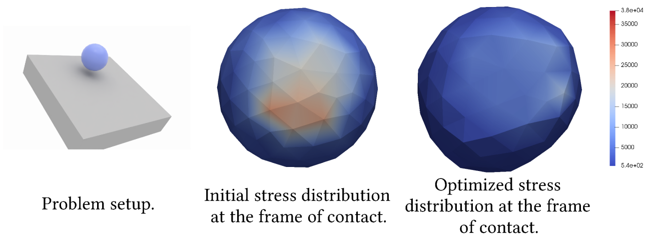
3.8e+04
35000
30000
25000
20000
15000
10000
5000
5.4e+02
Problem setup.
Initial stress distribution at the frame of contact.
Optimized stress distribution at the frame of contact.

Fig. 12. **Transient: Sliding Ball.** Result of shape optimization to reduce stress.

(30) of the load being dropped onto the microstructure is minimized. To accelerate convergence, we adopt a low-parametric shape representation from [Panetta et al. 2015]. In Figure 13, the maximal stress is reduced from 32 kPa to 12 kPa. This example involves complex self-contact inside the microstructure. Unlike penalty-based contact, our method is intersection-free regardless of the contact parameters, so able to produce plausible results with the same configuration even

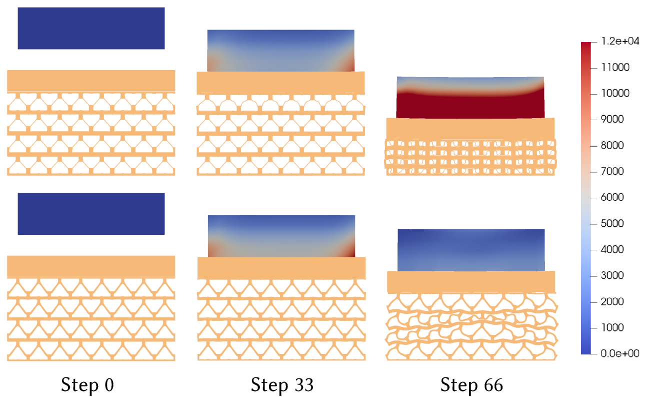

Fig. 13. **Transient: Shock Protection.** Shape optimization of the shock-protecting microstructure to reduce the stress on the falling load. The stress distribution at different time steps is shown for the initial shape (top) and optimized shape (bottom).

though the thickness of beams inside the microstructure changes drastically in the optimization.

**Transient: Sliding Ball.** We optimize the shape of a ball sliding down a ramp to minimize the internal stress (30). To avoid trivial solutions, we add a volume constraint to not allow its volume to decrease. Perhaps unsurprisingly, the ball gets flattened on the side it contacts with the ramp as this leads to a major reduction of max stress, from 38 kPa to 14 kPa.

## 10.3 Initial Conditions

Our formulation supports the optimization of objectives depending on the initial conditions. We show three examples: the first involves an object sliding on a ramp with a complex geometry, the second simulates a game of pool, using bunnies instead of spheres, and the third demonstrates complex contact between tentacles.

**Transient: Puzzle Piece.** We synthesise a trajectory using a forward simulation, and we then perturb the initial conditions and try to reconstruct them minimizing (31), with an additional integration over time (Figure 14). The puzzle piece uses a Neo-Hookean material.

**Transient: Throw Bunny.** We use our solver to optimize the throw (initial velocity) of a bunny to hit and displace a second bunny into the prescribed circle (Figure 1), minimizing (32). This example involves complex contact between the bunnies and the pool table, and also friction forces slowing down the sliding after contact.

**Transient: Colliding Tentacles.** We optimize the initial velocity of the green object in the scene of two colliding half spheres with tentacles (Figure 15), minimizing the difference of the mass trajectory with respect to a trajectory obtained from a reference simulation (32). Our method manages to resolve the complex contact between the soft tentacles.

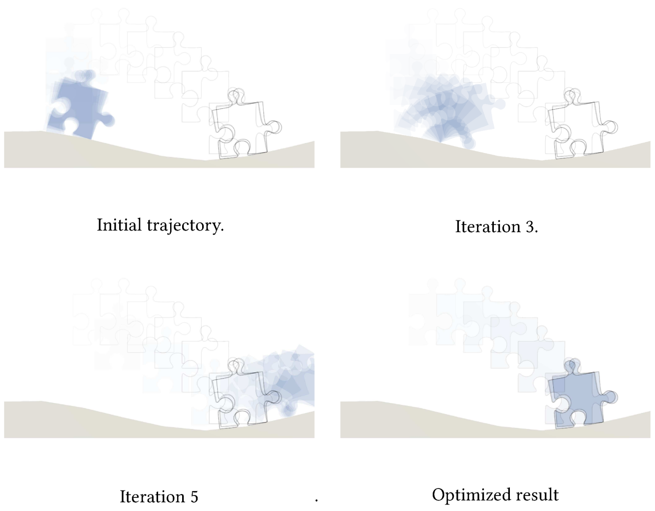

Fig. 14. **Transient: Puzzle Piece.** Optimizing the initial velocity of a bouncing puzzle. Target is shown as a black outline while the trajectory being optimized is blue.

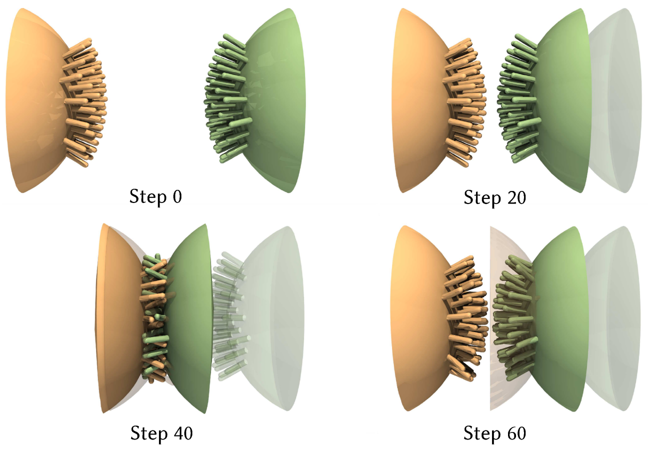

Fig. 15. **Transient: Colliding Tentacles.** We optimize the initial velocity so that the mass trajectory matches the reference simulation. The faded view represents the initial configuration. The optimized simulation matches exactly with the reference simulation.

## 10.4 Material Optimization

Next, we look at material optimization problems, where our differentiable simulator is used to estimate the material properties of an object from observations of its displacement.

**Static: Sine.** We optimize the material of a bar to match the shape of a sine function (wire-frame) when Dirichlet boundary conditions are applied at its ends (31). The rest shape of this bar is a rectangle $[-4, 4] \times [-0.3, 0.3]$, the left and right surfaces are fixed by Dirichlet boundary condition of $u_y = 0.7\sin(x + u_x)$ and $u_x = -sign(x)$,

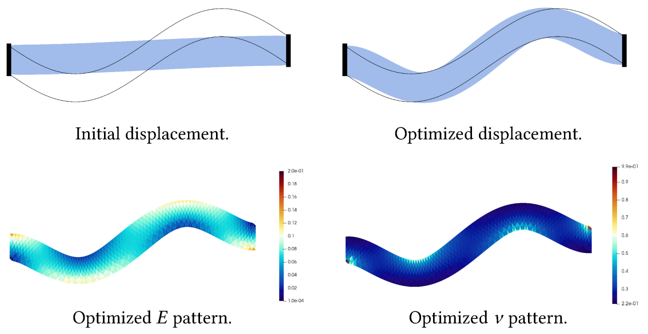

Fig. 16. **Static: Sine.** Optimized material parameters to obtain a displacement (blue surface) in $y$-direction similar to a sine function for a linear material model (wire-frame).

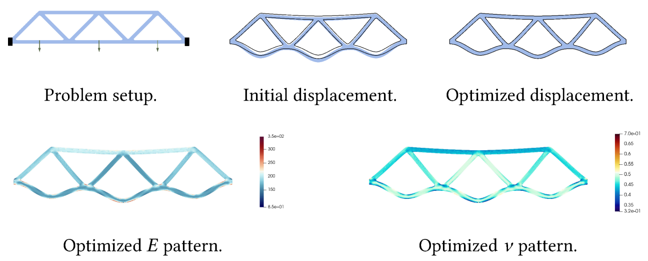

Fig. 17. **Static: Bridge.** Optimization of the materials of a bridge (blue surface) to match a forward simulation (wire-frame).

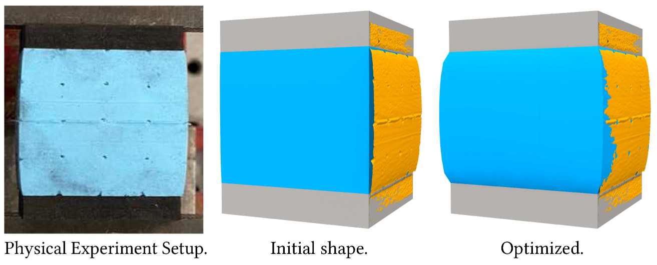

Fig. 18. **Static: Cube.** Material optimization (blue) to match real data (orange).

and no body force is applied. Figure 16 shows that deformed bar is aligned with a sine function.

**Static: Bridge.** We assign material parameters $\lambda = 160, \mu = 80$ to a bridge shape and run a linear forward simulation to obtain the target displacement $u^\star$ (Figure 17 in gray), using the same set of boundary conditions as Figure 5. We initialize the optimization using uniform material $\lambda = 100, \mu = 50$ and minimize (31), successfully recovering $\lambda, \mu$ from $u^\star$.

**Static: Cube.** We set up a physical experiment with a silicon rubber cube compressed by a vise. The deformation is acquired using an HP 3D scanner, and a set of marker points is manually extracted from the scan. We minimize (31) to find the material parameters which

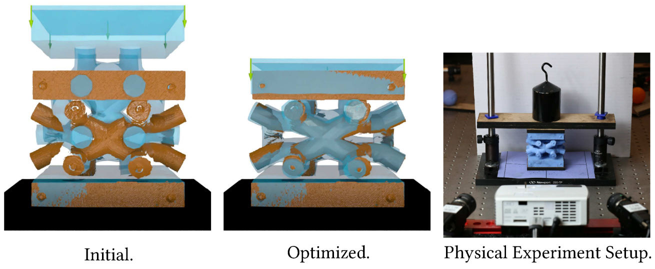

Fig. 19. **Static: Micro-Structure** Material optimization of a complex microstructure in a deformed state with contact (blue) to match real data (orange).

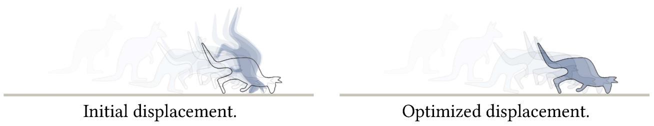

Fig. 20. **Transient: Kangaroo.** Non-linear transient simulation of a kangaroo (blue surface) bouncing on a plane to match a target shape (wire-frame).

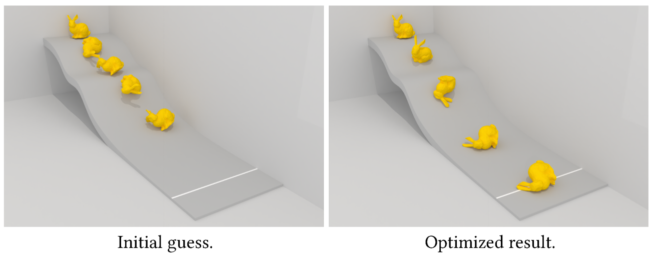

Fig. 21. **Transient: Sliding Bunny.** Optimize the friction coefficient so that the bunny can reach the white line at $t = 2$.

produce the observed displacements. We found that the material parameter that leads to the smallest error is $\nu = 0.4817$ (Young's modulus does not affect its deformation in this setting) and the L2 error in markers position is $3.85 \times 10^{-3}$ m.

**Static: Micro-Structure.** We repeat the same experiments with the complex geometry of a micro-structure tile from [Panetta et al. 2017]. This is a challenging example, as the micro-structure beams come in contact after compression, and physical models without self-contact handling may lead to penetration. The optimization is initialized with $E = 10^6$ Pa and $\nu = 0.3$ and converges to $E = 2.27 \times 10^5$ Pa and $\nu = 0.348$. Our solver can find material properties $E = 2.27 \times 10^5$ Pa and $\nu = 0.348$ with a L2 error on the markers of $8.8 \times 10^{-3}$ m.

**Transient: Kangaroo.** As an example of reconstruction of material parameters from a transient simulation, we run a forward simulation to obtain a transient non-linear target displacement. Then we minimize (31) to reconstruct the material parameters (Figure 20). The initial material parameters are $E = 3 \times 10^6$ Pa and $\nu = 0.5$, and the target material parameters are $E = 10^7$ Pa and $\nu = 0.3$.

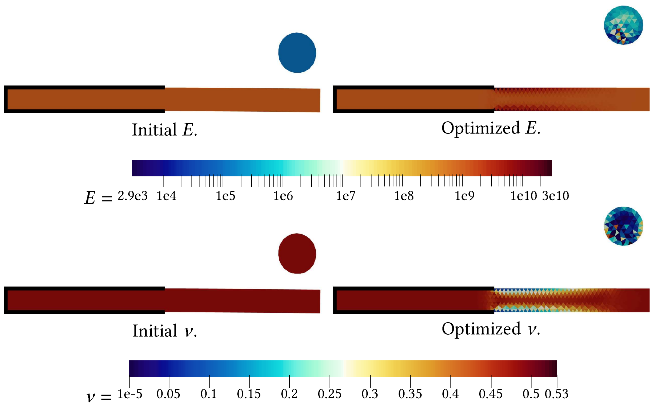
Initial $E$.
Optimized $E$.
$E =$ 2.9e3 1e4 1e5 1e6 1e7 1e8 1e9 1e10 3e10
Initial $\nu$.
Optimized $\nu$.
$\nu =$ 1e-5 0.05 0.1 0.15 0.2 0.25 0.3 0.35 0.4 0.45 0.5 0.53

Fig. 22. **Transient: Bouncing Ball.** Material optimization to increase the bouncing height.

**Transient: Sliding Bunny.** We use our solver to optimize the friction coefficient to ensure that the bunny is on the white line at time $t = 2$. The initial friction coefficient is $\gamma = 0.5$, and the optimized friction coefficient is $\gamma = 0.0974$ (Figure 21). This example involves complex self-contact and friction of the bunny with the floor.

**Transient: Bouncing Ball.** We show that the height of the bounce of a ball can be optimized by changing the material parameters (Figure 22). Initial material parameters for the ball and plank were $E = 10^5$ Pa, $\nu = 0.48$ and $E = 10^9$ Pa, $\nu = 0.48$, respectively and the elasticity model used was NeoHookean. Note that we added a smoothing term to the optimization to increase smoothness in the material parameters.

**Transient: Physical Experiment Bouncing Ball.** We show that we can optimize for the initial velocity, material parameters, friction coefficient, and damping parameters of a silicone rubber ball bouncing on an incline, using trajectory data from a physical experiment. The real-world dynamics of the ball are captured using a high-speed camera and used to formulate a functional based on (32), which penalizes differences between the observed and simulated barycenter of the ball. The material model used is NeoHookean and we match initial conditions by optimizing for them using the observed barycenters of the ball before it hits the ground.

## 10.5 Comparisons

Finally, we compare our method with existing methods in terms of solution quality, contact handling, and efficiency. Due to stability issues, different time step sizes are chosen for different methods so that no visible artifacts appear in the forward simulations. See Table 5 for statistics. We also compare our method with finite difference and automatic differentiation on PolyFEM [Schneider et al. 2019] in terms of efficiency.

**Transient: Armadillo.** We simulate dropping the Armadillo (using the same material parameters) onto a fixed plane (Figure 24) and compute the material derivatives with our method, DiffPD [Du et al.

Physical experiment.

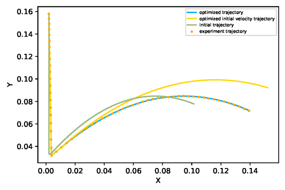

$xy$ coordinates of the barycenter of the ball over time.

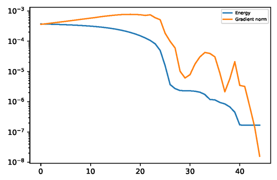

Energy and gradient over the optimization iterations.

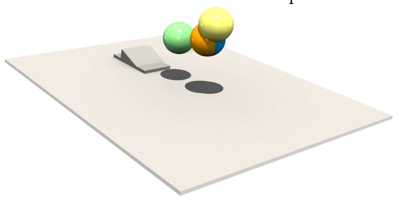

Initial guess (green), initial velocity optimization (yellow), material optimization (blue), and experimental data (orange).

Fig. 23. **Transient: Physical Experiment Bouncing Ball.** Optimize the material and initial velocity of the ball to match the observed physical result.

Table 5. **Comparisons.** Columns from left to right are examples, methods, degree of freedom of the simulation, time step size, peak memory (MB), running time of the simulation (s), and running time of computing gradients (s).

| Example | Method | Dofs | dt | Memory | Solve time | Grad time |
|---|---|---|---|---|---|---|
| Armadillo | DiffPD | 36699 | $3\times10^{-3}$ | 1246 | 37.9 | 131.2 |
| | GradSim | 36699 | $1.5\times10^{-5}$ | 17164 | 167.2 | N/A |
| | **Ours** | 36699 | $6\times10^{-3}$ | 2068 | 220.6 | 14.1 |
| Hilbert Cube | DiffPD | 4050 | $5\times10^{-2}$ | 240 | 1.555 | 2.12 |
| | GradSim | 4050 | $5\times10^{-4}$ | 1323 | 11.1 | 27.7 |
| | **Ours** | 4050 | $5\times10^{-2}$ | 1599 | 73.2 | 1.73 |
| Billiards | DiffPD | 978 | $2.5\times10^{-3}$ | 226 | 11.3 | 10.5 |
| | **Ours** | 978 | $2.5\times10^{-3}$ | 190 | 66.2 | 3.1 |

2021] and GradSim [Jatavallabhula et al. 2021]. The results of GradSim and our method are similar, which is expected as both methods are based on a finite element formulation with a similar material model. However, the backward solve of GradSim encounters NAN and fails to compute the gradient, likely due to the instability from its semi-implicit time integration or the non-differentiable contact model (Its contact force is only $C^0$). DiffPD creates a result that is different from the two, likely due to the use of a different elastic model.

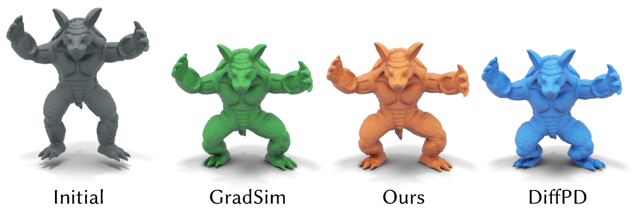

Fig. 24. **Transient: Armadillo.** Simulation of dropping an Armadillo onto the floor.

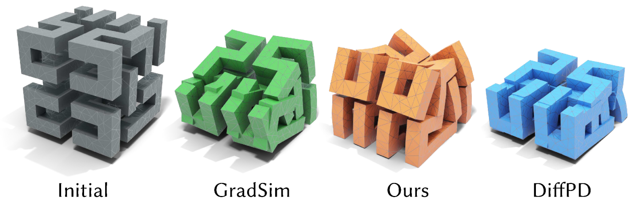

Fig. 25. **Transient: Hilbert Cube.** Simulation of dropping a Hilbert cube onto the floor.

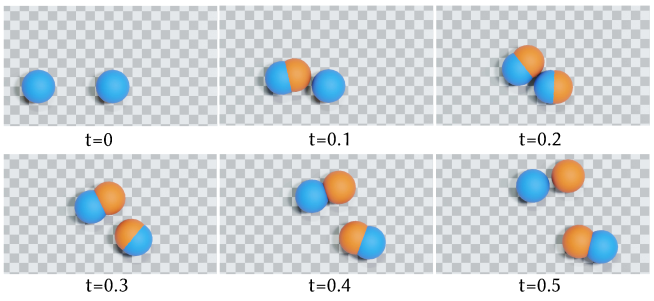

Fig. 26. **Transient: Billiards.** The ball on the left with initial velocity $(\cos(\frac{15}{180}\pi), \sin(\frac{15}{180}\pi))$ hits the ball on the right, simulated with our method (orange) and DiffPD (blue).

**Transient: Hilbert Cube.** In this example, we simulate the drop of a Hilbert cube (Figure 25), compute the material derivatives, and compare our method with GradSim and DiffPD. Although GradSim and DiffPD can resolve the planar contact, they do not support self-collision, resulting in visible and physically implausible self-intersections. In contrast, the solution computed by our method has no self-intersections or inverted elements.

**Static: Tensile Test.** We perform the tensile testing on a bar of size 0.16m × 0.08m × 0.08m, with Poisson's ratio $\nu = 0.3$ and Young's modulus $E = 10^3$Pa, using both our method and DiffPD. We refine the meshes used in both methods until the results become stable and show the converged results. Since there is no contact, our method is equivalent to the standard FEM with Neo-Hookean material. Since the material model used in DiffPD is an approximation of the hyper-elastic model designed for high efficiency, there is a noticeable difference between DiffPD and the standard model when the deformation is large (Figure 27). We favor using the Neo-Hookean

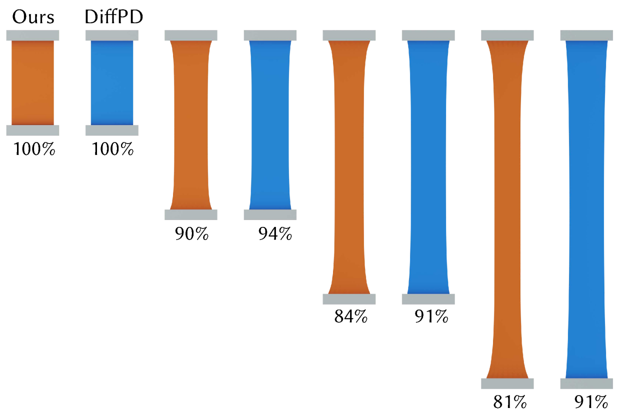

Fig. 27. **Static: Tensile Test.** Stretch a 3D bar up to 300% strain with our method (orange) and DiffPD (blue). The thickness of the deformed bar is shown as a percentage with respect to the initial thickness.

material model, as we are interested in accurately capturing large physical deformations.

**Transient: Billiards.** In this example we reproduce the billiards example in [Du et al. 2021] (Figure 26), and compute the material derivatives. Since GradSim does not support collisions between spheres (or between meshes), we restrict the comparison to DiffPD.

Although the same mesh is used in both methods, there is a significant difference in the contact handling: Our method detects the collision between the discrete meshes, while DiffPD uses the averaged sphere center and radius to detect the collision between spheres. While more efficient, the DiffPD solution is customized for this example, while our approach works on arbitrary geometries. Due to the difference in both the elastic model (Figure 27) and contact handling, the results are different. Our forward simulation is 6 times slower than DiffPD.

**Finite Difference.** To evaluate the correctness and efficiency of our method, we compute the gradient using finite differences and compare it with our method. We use the central difference scheme, which requires solving the forward problem for $2n$ times if the parameter dimension is $n$. As a result, the finite difference is approximately twice as expensive as the forward solve, while the time of our method is negligible (Table 6).

Table 6. **Finite Difference.** Columns from left to right are examples, dimension of the design parameters, running time of the simulation (s), running time of the adjoint method (s), and running time of the finite difference (s). The accuracy is the relative error between the finite difference and the adjoint method.

| Example | Dim | Solve time | Grad time | FD time | Accuracy |
|---|---|---|---|---|---|
| Shock Protection (Figure 13) | 24 | 1273 | 131.8 | 63502 | $1.12 \times 10^{-2}$ |
| Micro-Structure (Figure 19) | 2 | 42.1 | 0.089 | 172.1 | $2.25 \times 10^{-6}$ |
| Sliding Bunny (Figure 21) | 1 | 544.6 | 1.74 | 1092 | $6.35 \times 10^{-10}$ |

**Automatic Differentiation (AD).** While it is impossible to transform the linear solver to AD form for large problems (see Section 2.1), we could use AD to compute the terms needed in the adjoint method. To evaluate the difference in performance between AD and analytic derivation, we focus our investigation on the local assembly of the elastic force vector into AD form [Jakob 2010] to compute the $\mathbf{p}^T \partial_\mathbf{q} \mathbf{h}^k$ in Equation (11). We solve the static NeoHookean PDE on a tetrahedral mesh with 4670 vertices and using linear FE bases. Our method of computing $\mathbf{p}^T \partial_\mathbf{q} \mathbf{h}^k$ takes 0.0174 seconds, while AD takes 0.247 seconds. The forward nonlinear solve takes 2.85 seconds, and the backward adjoint solve takes 0.0212 seconds. Given this experiment, we opted to spend the additional effort in analytically deriving the adjoint terms to avoid this unnecessary additional computational cost. In our setting with expensive implicit solves, the cost of computing the adjoint terms is a small overhead on the whole optimization, and computing the derivatives with AD makes the implementation simpler and makes it easier to switch the material models. However, we found that for more complex contact models, not included in this paper, the cost of AD can still be significant, and in settings in which forward solves can be done explicitly or semi-implicitly, the computational costs are distributed differently.

## 11 CONCLUDING REMARKS

We introduced a generic, robust, and accurate framework for PDE-constrained optimization problems involving elastic deformations of multiple objects with contact and friction forces. Our framework supports customizable objective functions and allows for the optimization of functionals involving the geometry of the objects involved, material parameters, contact/friction parameters, and boundary/initial conditions.

There are several limitations in our work. First, our derivation is limited to hyper-elastic and visco-elastic materials. We don't support simulating shells (cloth), plastic materials, fluid, etc. Second, rigid and articulated objects, which are widely used in robotics, are not supported. Although it can be approximated by very large stiffness in our framework, the simulation is much slower than rigid body simulations. Third, our forward simulation, though robust, is less efficient than previous works like [Du et al. 2021; Jatavallabhula et al. 2021] in simple scenes (Section 10.5).

We believe the benefits of our analytic derivation of the adjoint system (efficiency, generality, guarantee of convergence under refinement) outweigh its downsides (complexity of derivation, difficulty in implementation, and requirement of an explicit FE mesh). We plan to extend our approach to a wider set of PDE-constrained problems and to further optimize it for common use cases in material design and robotics. In particular, we would like to explore the following directions:

(1) Add support for periodic boundary conditions, which are required for the design of micro-structure families [Tozoni et al. 2020].

(2) Add support for rigid and articulated objects (i.e. allow the material stiffness to be infinite). We plan to incorporate the IPC

formulation introduced in [Ferguson et al. 2021] to improve performance in design problems involving rigid objects.

(3) Many robotics problems involve the manipulation of plastic objects or interaction with fluids: adding support for additional physical models will widen the applicability of our simulator.

(4) We designed our system to provide accurate modeling of elastic, contact, and friction forces, as the majority of PDE-constrained applications require accurate simulations faithfully reproducing the behavior observable in the real works. However, there are applications where this is not necessary, and in these cases, it would be possible to either use simpler elastic models or reduce the accuracy of the collision/friction forces by using proxy geometry. This is commonly done in graphics settings, and it would be interesting to add this option to our system to accelerate its performance.

## ACKNOWLEDGMENTS

This work was supported in part through the NYU IT High Performance Computing resources, services, and staff expertise. This work was also partially supported by the NSF CAREER award under Grant No. 1652515, the NSF grants OAC-1835712, CHS-1908767, CHS-1901091, IIS-2313156, a Sloan Fellowship, and a gift from Adobe Research.

## REFERENCES

Christie Alappat, Achim Basermann, Alan R. Bishop, Holger Fehske, Georg Hager, Olaf Schenk, Jonas Thies, and Gerhard Wellein. 2020. A Recursive Algebraic Coloring Technique for Hardware-Efficient Symmetric Sparse Matrix-Vector Multiplication. *ACM Trans. Parallel Comput.* 7, 3, Article 19 (June 2020), 37 pages. https://doi.org/10.1145/3399732

Grégoire Allaire, Charles Dapogny, and François Jouve. 2021. Chapter 1 - Shape and topology optimization. In *Geometric Partial Differential Equations - Part II*, Andrea Bonito and Ricardo H. Nochetto (Eds.). Handbook of Numerical Analysis, Vol. 22. Elsevier, 1–132. https://doi.org/10.1016/bs.hna.2020.10.004

M. S. Alnaes, J. Blechta, J. Hake, A. Johansson, B. Kehlet, A. Logg, C. Richardson, J. Ring, M. E. Rognes, and G. N. Wells. 2015. The FEniCS Project Version 1.5. *Archive of Numerical Software* 3 (2015). https://doi.org/10.11588/ans.2015.100.20553

Moritz Bächer, Espen Knoop, and Christian Schumacher. 2021. Design and Control of Soft Robots Using Differentiable Simulation. *Current Robotics Reports* (2021), 1–11.

Pierre Baque, Edoardo Remelli, François Fleuret, and Pascal Fua. 2018. Geodesic convolutional shape optimization. In *International Conference on Machine Learning*. PMLR, 472–481.

Ted Belytschko, Wing Kam Liu, and Brian Moran. 2000. *Nonlinear Finite Elements for Continua and Structures.* John Wiley & Sons, Ltd.

P. Beremlijski, J. Haslinger, J. Outrata, and R. Pathó. 2014. Shape Optimization in Contact Problems with Coulomb Friction and a Solution-Dependent Friction Coefficient. *SIAM Journal on Control and Optimization* 52, 5 (Jan. 2014), 3371–3400. https://doi.org/10.1137/130948070

James Bern, Pol Banzet, Roi Poranne, and Stelian Coros. 2019. Trajectory Optimization for Cable-Driven Soft Robot Locomotion. In *Robotics: Science and Systems XV*, Vol. 1. Robotics: Science and Systems Foundation. https://doi.org/10.15607/rss.2019.xv.052

James M. Bern, Yannick Schnider, Pol Banzet, Nitish Kumar, and Stelian Coros. 2020. Soft Robot Control With a Learned Differentiable Model. In *2020 3rd IEEE International Conference on Soft Robotics (RoboSoft)*. IEEE, 417–423. https://doi.org/10.1109/robosoft48309.2020.9116011

C. H. Bischof and H. M. Bücker. 2000. Computing Derivatives of Computer Programs. In *Modern Methods and Algorithms of Quantum Chemistry: Proceedings, Second Edition*, J. Grotendorst (Ed.). NIC Series, Vol. 3. NIC-Directors, Jülich, 315–327. http://hdl.handle.net/2128/6053

Matthias Bollhöfer, Aryan Eftekhari, Simon Scheidegger, and Olaf Schenk. 2019. Large-scale Sparse Inverse Covariance Matrix Estimation. *SIAM Journal on Scientific Computing* 41, 1 (2019), A380–A401. https://doi.org/10.1137/17M1147615 arXiv:https://doi.org/10.1137/17M1147615

Matthias Bollhöfer, Olaf Schenk, Radim Janalik, Steve Hamm, and Kiran Gullapalli. 2020. State-of-the-Art Sparse Direct Solvers. (2020), 3–33. https://doi.org/10.1007/978-3-030-43736-7_1

Robert Bridson, Ronald Fedkiw, and John Anderson. 2002. Robust Treatment of Collisions, Contact and Friction for Cloth Animation. *ACM Trans. on Graph.* 21 (05 2002).

Bernard Brogliato. 1999. *Nonsmooth Mechanics.* Springer-Verlag.

George E. Brown, Matthew Overby, Zahra Forootaninia, and Rahul Narain. 2018. Accurate Dissipative Forces in Optimization Integrators. *ACM Trans. Graph.* 37, 6, Article 282 (dec 2018), 14 pages. https://doi.org/10.1145/3272127.3275011

Michael B Chang, Tomer Ullman, Antonio Torralba, and Joshua B Tenenbaum. 2016. A compositional object-based approach to learning physical dynamics. *arXiv preprint arXiv:1612.00341* (2016).

Bicheng Chen, Nianfeng Wang, Xianmin Zhang, and Wei Chen. 2020. Design of dielectric elastomer actuators using topology optimization on electrodes. *Smart Mater. Struct.* 29, 7 (June 2020), 075029. https://doi.org/10.1088/1361-665x/ab8b2d

Gilles Daviet, Florence Bertails-Descoubes, and Laurence Boissieux. 2011. A Hybrid Iterative Solver for Robustly Capturing Coulomb Friction in Hair Dynamics. *ACM Trans. on Graph.* 30 (12 2011).

Alban de Vaucorbeil, Vinh Phu Nguyen, Sina Sinaie, and Jian Ying Wu. 2019. Material point method after 25 years: theory, implementation and applications. *Submitted to Advances in Applied Mechanics* (2019), 1.

B. Desmorat. 2007. Structural rigidity optimization with frictionless unilateral contact. *International Journal of Solids and Structures* 44, 3 (Feb. 2007), 1132–1144. https://doi.org/10.1016/j.ijsolstr.2006.06.010

Jørgen S. Dokken, Sebastian K. Mitusch, and Simon W. Funke. 2020. Automatic shape derivatives for transient PDEs in FEniCS and Firedrake. arXiv:2001.10058 [math.OC]

Tao Du, Kui Wu, Pingchuan Ma, Sebastien Wah, Andrew Spielberg, Daniela Rus, and Wojciech Matusik. 2021. DiffPD: Differentiable Projective Dynamics. *ACM Trans. Graph.* 41, 2, Article 13 (nov 2021), 21 pages. https://doi.org/10.1145/3490168

Christof Eck, Jiri Jarusek, Miroslav Krbec, Jiri Jarusek, and Miroslav Krbec. 2005. *Unilateral Contact Problems : Variational Methods and Existence Theorems.* CRC Press. https://doi.org/10.1201/9781420027365

Zachary Ferguson et al. 2020. *IPC Toolkit.* https://ipc-sim.github.io/ipc-toolkit/

Zachary Ferguson, Minchen Li, Teseo Schneider, Francisca Gil-Ureta, Timothy Langlois, Chenfanfu Jiang, Denis Zorin, Danny M. Kaufman, and Daniele Panozzo. 2021. Intersection-free Rigid Body Dynamics. *ACM Transactions on Graphics (SIGGRAPH)* 40, 4, Article 183 (2021).

Konstantinos Gavriil, Ruslan Guseinov, Jesús Pérez, Davide Pellis, Paul Henderson, Florian Rist, Helmut Pottmann, and Bernd Bickel. 2020. Computational Design of Cold Bent Glass FaçAdes. *ACM Trans. Graph.* 39, 6, Article 208 (nov 2020), 16 pages. https://doi.org/10.1145/3414685.3417843

Moritz Geilinger, David Hahn, Jonas Zehnder, Moritz Bächer, Bernhard Thomaszewski, and Stelian Coros. 2020. ADD: analytically differentiable dynamics for multi-body systems with frictional contact. *ACM Transactions on Graphics (TOG)* 39, 6 (2020), 1–15.

Christophe Geuzaine and Jean-François Remacle. 2009. Gmsh: A 3-D finite element mesh generator with built-in pre- and post-processing facilities. *Internat. J. Numer. Methods Engrg.* 79, 11 (2009), 1309–1331. https://doi.org/10.1002/nme.2579 arXiv:https://onlinelibrary.wiley.com/doi/pdf/10.1002/nme.2579

Andreas Griewank and Andrea Walther. 2008. *Evaluating derivatives: principles and techniques of algorithmic differentiation.* Vol. 105. Siam. https://doi.org/10.1137/1.9780898717761

Christian Hafner, Christian Schumacher, Espen Knoop, Thomas Auzinger, Bernd Bickel, and Moritz Bächer. 2019. X-CAD: Optimizing CAD Models with Extended Finite Elements. *ACM Trans. Graph.* 38, 6, Article 157 (Nov. 2019), 15 pages. https://doi.org/10.1145/3355089.3356576

David Hahn, Pol Banzet, James M. Bern, and Stelian Coros. 2019. Real2Sim: Visco-Elastic Parameter Estimation from Dynamic Motion. *ACM Trans. Graph.* 38, 6, Article 236 (Nov. 2019), 13 pages. https://doi.org/10.1145/3355089.3356548

David Harmon, Etienne Vouga, Breannan Smith, Rasmus Tamstorf, and Eitan Grinspun. 2009. Asynchronous contact mnumpageechanics. In *ACM Trans. on Graph. (TOG)*, Vol. 28. ACM.

David Harmon, Etienne Vouga, Rasmus Tamstorf, and Eitan Grinspun. 2008. Robust Treatment of Simultaneous Collisions. *SIGGRAPH (ACM Trans. on Graph.)* 27, 3 (2008).

Jaroslav Haslinger, Pekka Neittaanmaki, and Timo Tiihonen. 1986. Shape optimization in contact problems based on penalization of the state inequality. *Aplikace matematiky* 31, 1 (1986), 54–77. https://eudml.org/doc/15435

Eric Heiden, Miles Macklin, Yashraj S Narang, Dieter Fox, Animesh Garg, and Fabio Ramos. 2021. DiSECt: A Differentiable Simulation Engine for Autonomous Robotic Cutting. In *Proceedings of Robotics: Science and Systems.* Virtual. https://doi.org/10.15607/RSS.2021.XVII.067

Eric Heiden, David Millard, Erwin Coumans, Yizhou Sheng, and Gaurav S Sukhatme. 2020. NeuralSim: Augmenting Differentiable Simulators with Neural Networks. *arXiv preprint arXiv:2011.04217* (2020).

J. Herskovits, A. Leontiev, G. Dias, and G. Santos. 2000. Contact shape optimization: a bilevel programming approach. *Structural and Multidisciplinary Optimization* 20, 3 (Nov. 2000), 214–221. https://doi.org/10.1007/s001580050149

Shayan Hoshyari, Hongyi Xu, Espen Knoop, Stelian Coros, and Moritz Bächer. 2019. Vibration-minimizing motion retargeting for robotic characters. *ACM Trans. Graph.* 38, 4 (July 2019), 1–14. https://doi.org/10.1145/3306346.3323034

Jerry Hsu, Nghia Truong, Cem Yuksel, and Kui Wu. 2022. A General Two-Stage Initialization for Sag-Free Deformable Simulations. *ACM Trans. Graph.* 41, 4, Article 64 (jul 2022), 13 pages. https://doi.org/10.1145/3528223.3530165

Yuanming Hu, Luke Anderson, Tzu-Mao Li, Qi Sun, Nathan Carr, Jonathan Ragan-Kelley, and Fredo Durand. 2019a. DiffTaichi: Differentiable Programming for Physical Simulation. In *International Conference on Learning Representations.*

Yuanming Hu, Jiancheng Liu, Andrew Spielberg, Joshua B Tenenbaum, William T Freeman, Jiajun Wu, Daniela Rus, and Wojciech Matusik. 2019b. Chainqueen: A real-time differentiable physical simulator for soft robotics. In *2019 International conference on robotics and automation (ICRA).* IEEE, 6265–6271.

Yixin Hu, Teseo Schneider, Bolun Wang, Denis Zorin, and Daniele Panozzo. 2020. Fast Tetrahedral Meshing in the Wild. *ACM Trans. Graph.* 39, 4, Article 117 (July 2020), 18 pages. https://doi.org/10.1145/3386569.3392385

Wenzel Jakob. 2010. Mitsuba renderer. http://www.mitsuba-renderer.org.

Krishna Murthy Jatavallabhula, Miles Macklin, Florian Golemo, Vikram Voleti, Linda Petrini, Martin Weiss, Breandan Considine, Jerome Parent-Levesque, Kevin Xie, Kenny Erleben, Liam Paull, Florian Shkurti, Derek Nowrouzezahrai, and Sanja Fidler. 2021. gradSim: Differentiable simulation for system identification and visuomotor control. *International Conference on Learning Representations (ICLR)* (2021). https://openreview.net/forum?id=c_E8kFWfhp0

Zhongshi Jiang, Teseo Schneider, Denis Zorin, and Daniele Panozzo. 2020. Bijective Projection in a Shell. *ACM Trans. Graph.* 39, 6, Article 247 (nov 2020), 18 pages. https://doi.org/10.1145/3414685.3417769

Noboru Kikuchi and John Tinsley Oden. 1988. *Contact Problems in Elasticity: A Study of Variational Inequalities and Finite Element Methods.* SIAM Studies in App. and Numer. Math., Vol. 8. Society for Industrial and Applied Mathematics.

Patrick M. Knupp. 2001. Algebraic Mesh Quality Metrics. *SIAM Journal on Scientific Computing* 23, 1 (2001), 193–218. https://doi.org/10.1137/S1064827500371499 arXiv:https://doi.org/10.1137/S1064827500371499

Minchen Li, Zachary Ferguson, Teseo Schneider, Timothy Langlois, Denis Zorin, Daniele Panozzo, Chenfanfu Jiang, and Danny M. Kaufman. 2020. Incremental Potential Contact: Intersection- and Inversion-free Large Deformation Dynamics. *ACM Transactions on Graphics* 39, 4 (2020).

Minchen Li, Zachary Ferguson, Teseo Schneider, Timothy Langlois, Denis Zorin, Daniele Panozzo, Chenfanfu Jiang, and Danny M. Kaufman. 2023a. Convergent Incremental Potential Contact. arXiv:2307.15908 [math.NA]

Yifei Li, Tao Du, Kui Wu, Jie Xu, and Wojciech Matusik. 2022. DiffCloth: Differentiable Cloth Simulation with Dry Frictional Contact. *ACM Trans. Graph.* (mar 2022). https://doi.org/10.1145/3527660 Just Accepted.

Zhehao Li, Qingyu Xu, Xiaohan Ye, Bo Ren, and Ligang Liu. 2023b. DiffFR: Differentiable SPH-Based Fluid-Rigid Coupling for Rigid Body Control. *ACM Trans. Graph.* 42, 6, Article 179 (dec 2023), 17 pages. https://doi.org/10.1145/3618318

Junbang Liang, Ming Lin, and Vladlen Koltun. 2019. Differentiable cloth simulation for inverse problems. *Neural Information Processing Systems* (2019).

Mickaël Ly, Romain Casati, Florence Bertails-Descoubes, Mélina Skouras, and Laurence Boissieux. 2018. Inverse Elastic Shell Design with Contact and Friction. *ACM Trans. Graph.* 37, 6, Article 201 (dec 2018), 16 pages. https://doi.org/10.1145/3272127.3275036

Guirec Maloisel, Espen Knoop, Christian Schumacher, and Moritz Bacher. 2021. Automated Routing of Muscle Fibers for Soft Robots. *IEEE Trans. Robot.* 37, 3 (June 2021), 996–1008. https://doi.org/10.1109/tro.2020.3043654

Charles C Margossian. 2019. A review of automatic differentiation and its efficient implementation. *Wiley Interdisciplinary Reviews: Data Mining and Knowledge Discovery* 9, 4 (2019), e1305. https://doi.org/10.1002/widm.1305

Aymeric Maury, Grégoire Allaire, and François Jouve. 2017. Shape optimisation with the level set method for contact problems in linearised elasticity. (Jan. 2017). https://hal.archives-ouvertes.fr/hal-01435325

Antoine McNamara, Adrien Treuille, Zoran Popović, and Jos Stam. 2004. Fluid Control Using the Adjoint Method. *ACM Transactions on Graphics / SIGGRAPH 2004* 23, 3 (Aug. 2004).

Sebastian K. Mitusch, Simon W. Funke, and Jørgen S. Dokken. 2019. dolfin-adjoint 2018.1: automated adjoints for FEniCS and Firedrake. *Journal of Open Source Software* 4, 38 (2019), 1292. https://doi.org/10.21105/joss.01292

William S. Moses, Sri Hari Krishna Narayanan, Ludger Paehler, Valentin Churavy, Michel Schanen, Jan Hückelheim, Johannes Doerfert, and Paul Hovland. 2022. Scalable Automatic Differentiation of Multiple Parallel Paradigms through Compiler Augmentation. In *Proceedings of the International Conference on High Performance Computing, Networking, Storage and Analysis* (Dallas, Texas) *(SC '22).* IEEE Press, Article 60, 18 pages.

Uwe Naumann. 2012. *The art of differentiating computer programs: an introduction to algorithmic differentiation.* Vol. 24. SIAM. https://doi.org/10.1137/1.9781611972078

Miguel Otaduy, Rasmus Tamstorf, Denis Steinemann, and Markus Gross. 2009. Implicit Contact Handling for Deformable Objects. *Comp. Graph. Forum* 28 (04 2009).

Julian Panetta, Abtin Rahimian, and Denis Zorin. 2017. Worst-case stress relief for microstructures. *ACM Transactions on Graphics* 36, 4 (2017). https://doi.org/10.1145/3072959.3073649

Julian Panetta, Qingnan Zhou, Luigi Malomo, Nico Pietroni, Paolo Cignoni, and Denis Zorin. 2015. Elastic Textures for Additive Fabrication. *ACM Trans. Graph.* 34, 4, Article 135 (July 2015), 12 pages.

Yi-Ling Qiao, Junbang Liang, Vladlen Koltun, and Ming Lin. 2020. Scalable Differentiable Physics for Learning and Control. In *International Conference on Machine Learning.* PMLR, 7847–7856.

Michael Rabinovich, Roi Poranne, Daniele Panozzo, and Olga Sorkine-Hornung. 2017. Scalable locally injective mappings. *ACM Transactions on Graphics (TOG)* 36, 4 (2017), 1.

Junior Rojas, Eftychios Sifakis, and Ladislav Kavan. 2021. Differentiable Implicit Soft-Body Physics. *arXiv preprint arXiv:2102.05791* (2021).

Connor Schenck and Dieter Fox. 2018. SPNets: Differentiable Fluid Dynamics for Deep Neural Networks. In *Proceedings of The 2nd Conference on Robot Learning (Proceedings of Machine Learning Research, Vol. 87)*, Aude Billard, Anca Dragan, Jan Peters, and Jun Morimoto (Eds.). PMLR, 317–335. https://proceedings.mlr.press/v87/schenck18a.html

Teseo Schneider, Jérémie Dumas, Xifeng Gao, Denis Zorin, and Daniele Panozzo. 2019. PolyFEM. https://polyfem.github.io/.

Christian Schumacher, Espen Knoop, and Moritz Bacher. 2020. Simulation-Ready Characterization of Soft Robotic Materials. *IEEE Robot. Autom. Lett.* 5, 3 (July 2020), 3775–3782. https://doi.org/10.1109/lra.2020.2982058

Christian Schumacher, Jonas Zehnder, and Moritz Bächer. 2018. Set-in-Stone: Worst-Case Optimization of Structures Weak in Tension. *ACM Trans. Graph.* 37, 6, Article 252 (dec 2018), 13 pages. https://doi.org/10.1145/3272127.3275085

Sicong Shan, Sung Kang, Jordan Raney, Pai Wang, Lichen Fang, Francisco Candido, Jennifer Lewis, and Katia Bertoldi. 2015. Multistable Architected Materials for Trapping Elastic Strain Energy. *Advanced materials (Deerfield Beach, Fla.)* 27 (06 2015). https://doi.org/10.1002/adma.201501708

Ashesh Sharma and Kurt Maute. 2018. Stress-based topology optimization using spatial gradient stabilized XFEM. *Structural and Multidisciplinary Optimization* 57, 1 (2018), 17–38.

Mélina Skouras, Bernhard Thomaszewski, Stelian Coros, Bernd Bickel, and Markus Gross. 2013. Computational Design of Actuated Deformable Characters. *ACM Trans. Graph.* 32, 4, Article 82 (jul 2013), 10 pages. https://doi.org/10.1145/2461912.2461979

David E Stewart. 2001. Finite-dimensional contact mechanics. *Phil. Trans. R. Soc. Lond. A* 359 (2001).

Stanisław Stupkiewicz, Jakub Lengiewicz, and Jovze Korelc. 2010. Sensitivity analysis for frictional contact problems in the augmented Lagrangian formulation. *Computer Methods in Applied Mechanics and Engineering* 199, 33 (July 2010), 2165–2176. https://doi.org/10.1016/j.cma.2010.03.021

Javier Tapia, Espen Knoop, Mojmir Mutný, Miguel A. Otaduy, and Moritz Bächer. 2020. MakeSense: Automated Sensor Design for Proprioceptive Soft Robots. *Soft Rob.* 7, 3 (June 2020), 332–345. https://doi.org/10.1089/soro.2018.0162

Davi Colli Tozoni, Jérémie Dumas, Zhongshi Jiang, Julian Panetta, Daniele Panozzo, and Denis Zorin. 2020. A Low-Parametric Rhombic Microstructure Family for Irregular Lattices. *ACM Trans. Graph.* 39, 4, Article 101 (jul 2020), 20 pages. https://doi.org/10.1145/3386569.3392451

Davi Colli Tozoni, Yunfan Zhou, and Denis Zorin. 2021. Optimizing Contact-Based Assemblies. *ACM Trans. Graph.* 40, 6, Article 269 (dec 2021), 19 pages. https://doi.org/10.1145/3478513.3480552

F. van Keulen, R.T. Haftka, and N.H. Kim. 2005. Review of options for structural design sensitivity analysis. Part 1: Linear systems. *Computer Methods in Applied Mechanics and Engineering* 194, 30 (2005), 3213–3243. https://doi.org/10.1016/j.cma.2005.02.002 Structural and Design Optimization.

Mickeal Verschoor and Andrei C Jalba. 2019. Efficient and accurate collision response for elastically deformable models. *ACM Trans. on Graph. (TOG)* 38, 2 (2019).

Patrick Wieschollek. 2016. CppOptimizationLibrary. https://github.com/PatWie/CppNumericalSolvers.

Peter Wriggers. 1995. Finite Element Algorithms for Contact Problems. *Archives of Comp. Meth. in Eng.* 2 (12 1995).

Jie Xu, Viktor Makoviychuk, Yashraj Narang, Fabio Ramos, Wojciech Matusik, Animesh Garg, and Miles Macklin. 2022. Accelerated Policy Learning with Parallel Differentiable Simulation. https://doi.org/10.48550/ARXIV.2204.07137

Xiaoting Zhang, Xinyi Le, Zihao Wu, Emily Whiting, and Charlie C.L. Wang. 2016. Data-Driven Bending Elasticity Design by Shell Thickness. *Computer Graphics Forum (Proceedings of Symposium on Geometry Processing)* 35, 5 (2016), 157–166.

## A TIME-DEPENDENT PROBLEMS

In this section, we show how to compute the derivative and adjoint equation for the time-dependent case. We do this in general form, only assuming that the force terms depend on solution and optimization parameters but not explicitly on time.

**Problem setup.** We assume all quantities involved in the adjoint equations and shape derivatives for the static case known from the main text. In this appendix, we derive how to update these to obtain the adjoint equation for the time-dependent PDE.

We consider the following time-dependent system, discretized in space.

$$\dot{\mathbf{u}} = \mathbf{v};\ M(\mathbf{q})\dot{\mathbf{v}} = \mathbf{h}(\mathbf{u}, \mathbf{q});\ \mathbf{u}(0) = \mathbf{g}^u(\mathbf{q});\ \mathbf{v}(0) = \mathbf{g}^v(\mathbf{q})$$

where $M(\mathbf{q})$ is the mass matrix, which may also depend on parameters $p$.

We assume that the discretization in time uses a BDF scheme of order $m$:

$$\dot{\mathbf{u}} \approx \frac{1}{\beta\Delta t}(\mathbf{u}^i + \sum_{j=1}^{\min(i,m)} \alpha_j^i \mathbf{u}^{i-j}).$$

In general, $\alpha_j^i$ does not depend on $i$, except at the first $m-1$ steps, when a higher-order scheme needs to be initialized with lower-order steps; more specifically, $\alpha_j^i$ is $j$-th coefficient of BDFi, for $1 \leqslant i < m$, and $j$-th coefficient of BDFm otherwise.

We assume that $\mathbf{h}(\mathbf{u}, \mathbf{q})$ does not directly depend on the velocities $\mathbf{v}$; if a dependence on velocities is needed, as we see below, it can be expressed directly in terms of $u$.

The discrete system has the form

$$\begin{aligned} \mathbf{u}^i + \sum_{j=1}^{\min(i,m)} \alpha_j^i \mathbf{u}^{i-j} &= \beta_i \Delta t\, \mathbf{v}^i, \\ M\left(\mathbf{v}^i + \sum_{j=1}^{\min(i,m)} \alpha_j^i \mathbf{v}^{i-j}\right) &= \beta_i \Delta t\, \mathbf{h}^i(\mathbf{u}^i, \mathbf{u}^{i-1}, \mathbf{q}) = \hat{\mathbf{h}}^i. \end{aligned} \tag{39}$$

where $M$ is the mass matrix. This is the form in which the system is solved in [Li et al. 2020].

For time-dependent problems, we consider functionals of the form

$$J(\mathbf{u}, \mathbf{q}) = \int_{t=0}^{T} J(\mathbf{u}, t, \mathbf{q}) dt,$$

where $J(\mathbf{u}, t, \mathbf{q})$ is a spatial functional, e.g., integral over the solid $\Omega(t)$ or its surface, of some pointwise quantity depending on the solution and/or its derivatives pointwise. In discretized form, this functional is

$$J(\mathbf{u}, \mathbf{q}) = \sum_{i=0}^{N} w_i J_i(\mathbf{u}^i, \mathbf{q}) = \sum_{i=0}^{N} \hat{J}^i,$$

where $w_i$ are quadrature weights (e.g., all $\Delta t$ in the simplest case), and N is the number of time steps.

**Remark on notation.** We omit most of the explicit arguments in functions $h$ and $J$ used in the expressions, to make the formulas more readable. The following is implied: $\mathbf{h}(\mathbf{u}^i, \mathbf{u}^{i-1}, \mathbf{q}, t_i) = \mathbf{h}_i(\mathbf{u}^i, \mathbf{u}^{i-1}, \mathbf{q}) = \mathbf{h}_i$ and similarly for $J_i$.

**Summary.** Computing the derivative $d_{\mathbf{q}}J$ requires the following components

- Derivatives $\partial_{\mathbf{u}} J_i$, $\partial_{\mathbf{u}} \mathbf{h}_i$, $\partial_{\mathbf{q}} J_i$ and $\partial_{\mathbf{q}} \mathbf{h}_i$. See Sections 7 to 9 in main text for corresponding formulas.
- Derivatives $\partial_{\mathbf{q}} \mathbf{g}^u$ and $\partial_{\mathbf{q}} \mathbf{g}^v$, derivatives of the initial conditions. See Section 5.4 in main text.

To compute the parametric derivative of $J$, the steps are as follows:

- Solve the forward system (39), and store the resulting solutions $\mathbf{u}^i, \mathbf{v}^i$, $i = 0 \dots N$ at every step.
- Initialize adjoint variables $\mathbf{p}_N, \boldsymbol{\nu}_N$ from (43) (general BDF: (13)).
- Perform backward time stepping using (41) (general BDF: (12)).
- At every step, evaluate derivative of the mass matrix $d_{\mathbf{q}}M$, if applicable, and use formula (44) (general BDF: (15)) to update $d_{\mathbf{q}}J$.

## A.1 Implicit Euler

**Discrete Lagrangian.** We use the Lagrangian-based approach (Céa's method) to derive the adjoint equation. The overall idea is to write the Lagrangian $\mathcal{L}$ for the functional $J$ viewing the equations for $\dot{\mathbf{v}}$ and $\dot{\mathbf{u}}$ as constraints with Lagrange multipliers $\mathbf{p}$ and $\boldsymbol{\mu}$. For the solution $(\mathbf{u}, \mathbf{v})$ for any optimization parameter values, the constraints are satisfied, $d_{\mathbf{q}}J = d_{\mathbf{q}}\mathcal{L}$, as the constraint terms identically vanish. The goal of introducing the adjoint variables is to eliminate the direct dependence of $d_{\mathbf{q}}J$ on the displacement and velocity derivatives: $d_{\mathbf{q}}\mathbf{u}^i$ or $d_{\mathbf{q}}\mathbf{v}^i$.

To achieve our objective, we expand the derivative $d_{\mathbf{q}}\mathcal{L}$, and isolate the terms multiplying $d_{\mathbf{q}}\mathbf{u}$ and $d_{\mathbf{q}}\mathbf{v}$. By setting the sum of each of these two sets of terms to zero (which corresponds to our adjoint equations), we can find $\mathbf{p}$ and $\boldsymbol{\mu}$ so that the derivative of the functional $d_{\mathbf{q}}J$ does not directly depend on $d_{\mathbf{q}}\mathbf{u}^i$ or $d_{\mathbf{q}}\mathbf{v}^i$.

The time-stepping for implicit Euler/BDF1 has the following simple form:

$$\begin{aligned} \mathbf{u}^i - \mathbf{u}^{i-1} &= \Delta t\, \mathbf{v}^i, \\ M(\mathbf{v}^i - \mathbf{v}^{i-1}) &= \Delta t\, \mathbf{h}^i = \hat{\mathbf{h}}^i. \end{aligned} \tag{40}$$

We introduce adjoint variables $p_i$ and $\mu_i$ (we use subscripts for the adjoint variables to indicate the time step, as these are often transposed in the formulas to make the formulas more readable).

In the derivation below, we drop most dependencies on variables, assuming $\hat{J}^i = \hat{J}^i(\mathbf{u}^i, \mathbf{q})$, $\mathbf{g}^u = \mathbf{g}^u(\mathbf{q})$, $\mathbf{g}^v = \mathbf{g}^v(\mathbf{q})$, $\hat{\mathbf{h}}^i = \hat{\mathbf{h}}(\mathbf{u}^i, \mathbf{u}^{i-1}, \mathbf{q})$ and $M = M(\mathbf{q})$.

The Lagrangian $\mathcal{L}$ has the form

$$\begin{aligned} \mathcal{L} = &\sum_{i=0}^{N} \hat{J}^i && \{\text{objective terms}\} \\ &+ \mathbf{p}_0^T(\mathbf{v}^0 - \mathbf{g}^v) + \boldsymbol{\mu}_0^T(\mathbf{u}^0 - \mathbf{g}^u) && \{\text{initial condition terms}\} \\ &+ \sum_{i=1}^{N} \mathbf{p}_i^T(M(\mathbf{v}^i - \mathbf{v}^{i-1}) - \hat{\mathbf{h}}^i) + \boldsymbol{\mu}_i^T(\mathbf{u}^i - \mathbf{u}^{i-1} - \Delta t\, \mathbf{v}^i). && \{\text{PDE terms}\} \end{aligned}$$

Rearranging terms, and shifting summation index for $\mathbf{u}^{i-1}$,

$$\begin{aligned}\mathcal{L} &= \mathbf{p}_0^T(\mathbf{v}^0 - \mathbf{g}^v) + \boldsymbol{\mu}_0^T(\mathbf{u}^0 - \mathbf{g}^u) + \hat{J}^0 \\ &+ \sum_{i=1}^{N} \hat{J}^i + \mathbf{p}_i^T(M(\mathbf{v}^i - \mathbf{v}^{i-1}) - \hat{\mathbf{h}}^i) + \boldsymbol{\mu}_i^T(\mathbf{u}^i - \mathbf{u}^{i-1} - \Delta t\, \mathbf{v}^i) \\ &= \mathbf{p}_0^T(\mathbf{v}^0 - \mathbf{g}^v) + \boldsymbol{\mu}_0^T(\mathbf{u}^0 - \mathbf{g}^u) + \hat{J}^0 \\ &+ \sum_{i=1}^{N} \hat{J}^i + \mathbf{p}_i^T(M\mathbf{v}^i - \hat{\mathbf{h}}^i) + \boldsymbol{\mu}_i^T(\mathbf{u}^i - \Delta t\, \mathbf{v}^i) - \sum_{i=0}^{N-1} \mathbf{p}_{i+1}^T M\mathbf{v}^i + \boldsymbol{\mu}_{i+1}^T \mathbf{u}^i.\end{aligned}$$

Combining two sums back together and separating $N$-th term from the first, we get

$$\begin{aligned}\mathcal{L} &= \mathbf{p}_0^T(\mathbf{v}^0 - \mathbf{g}^v) + \boldsymbol{\mu}_0^T(\mathbf{u}^0 - \mathbf{g}^u) + \hat{J}^0 - \mathbf{p}_1^T M\mathbf{v}^0 - \boldsymbol{\mu}_1^T\mathbf{u}^0 \\ &+ \sum_{i=1}^{N-1} \hat{J}^i + \mathbf{p}_i^T(M\mathbf{v}^i - \hat{\mathbf{h}}^i) + \boldsymbol{\mu}_i^T(\mathbf{u}^i - \Delta t\, \mathbf{v}^i) - \mathbf{p}_{i+1}^T M\mathbf{v}^i - \boldsymbol{\mu}_{i+1}^T\mathbf{u}^i \\ &+ \hat{J}^N + \mathbf{p}_N^T(M\mathbf{v}^N - \hat{\mathbf{h}}^N) + \boldsymbol{\mu}_N^T(\mathbf{u}^N - \Delta t\, \mathbf{v}^N).\end{aligned}$$

Collecting $\mathbf{u}^i$ and $\mathbf{v}^i$ terms:

$$\begin{aligned}\mathcal{L} &= \hat{J}^0 - \mathbf{p}_0^T\mathbf{g}^v - \boldsymbol{\mu}_0^T\mathbf{g}^u + (\mathbf{p}_0^T - \mathbf{p}_1^T M)\mathbf{v}^0 + (\boldsymbol{\mu}_0^T - \boldsymbol{\mu}_1^T)\mathbf{u}^0 \\ &+ \sum_{i=1}^{N-1} \hat{J}^i - \mathbf{p}_i^T\hat{\mathbf{h}}^i + (\boldsymbol{\mu}_i^T - \boldsymbol{\mu}_{i+1}^T)\mathbf{u}^i + ((\mathbf{p}_i^T - \mathbf{p}_{i+1}^T)M - \boldsymbol{\mu}_i^T\Delta t\,)\mathbf{v}^i \\ &+ \hat{J}^N - \mathbf{p}_N^T\hat{\mathbf{h}}^N + \boldsymbol{\mu}_N^T\mathbf{u}^N + (\mathbf{p}_N^T M - \boldsymbol{\mu}_N^T\Delta t\,)\mathbf{v}^N.\end{aligned}$$

Differentiating with respect to $\mathbf{q}$:

$$\begin{aligned}d_{\mathbf{q}}\mathcal{L} &= \partial_{\mathbf{q}}\hat{J}^0 - \mathbf{p}_0^T\partial_{\mathbf{q}}\mathbf{g}^v - \boldsymbol{\mu}_0^T\partial_{\mathbf{q}}\mathbf{g}^u - \mathbf{p}_1^T\partial_{\mathbf{q}}M\mathbf{v}^0 + (\mathbf{p}_0^T - \mathbf{p}_1^T M)d_{\mathbf{q}}\mathbf{v}^0 + \\ &+ (\partial_{\mathbf{u}^i}\hat{J}^0 + \boldsymbol{\mu}_0^T - \boldsymbol{\mu}_1^T)d_{\mathbf{q}}\mathbf{u}^0 + \\ &+ \sum_{i=1}^{N-1} \partial_{\mathbf{q}}\hat{J}^i - \mathbf{p}_i^T\partial_{\mathbf{q}}\hat{\mathbf{h}}^i + (\mathbf{p}_i^T - \mathbf{p}_{i+1}^T)\partial_{\mathbf{q}}M\mathbf{v}^i + \\ &+ \sum_{i=1}^{N-1} (\boldsymbol{\mu}_i^T - \boldsymbol{\mu}_{i+1}^T + \partial_{\mathbf{u}^i}\hat{J}^i - \mathbf{p}_i^T\partial_{\mathbf{u}^i}\hat{\mathbf{h}}^i)d_{\mathbf{q}}\mathbf{u}^i - \mathbf{p}_i^T\partial_{\mathbf{u}^{i-1}}\hat{\mathbf{h}}^i\, d_{\mathbf{q}}\mathbf{u}^{i-1} + \\ &+ ((\mathbf{p}_i^T - \mathbf{p}_{i+1}^T)M - \boldsymbol{\mu}_i^T\Delta t\,)d_{\mathbf{q}}\mathbf{v}^i + \\ &+ \partial_{\mathbf{q}}\hat{J}^N - \mathbf{p}_N^T\partial_{\mathbf{q}}\hat{\mathbf{h}}^N + (\partial_{\mathbf{u}^i}\hat{J}^N - \mathbf{p}_N^T\partial_{\mathbf{u}^N}\hat{\mathbf{h}}^N + \boldsymbol{\mu}_N^T)d_{\mathbf{q}}\mathbf{u}^N + \\ &- \mathbf{p}_N^T\partial_{\mathbf{u}^{N-1}}\hat{\mathbf{h}}^N d_{\mathbf{q}}\mathbf{u}^{N-1} + (\mathbf{p}_N^T M - \boldsymbol{\mu}_N^T\Delta t\,)d_{\mathbf{q}}\mathbf{v}^N + \mathbf{p}_N^T\partial_{\mathbf{q}}M\mathbf{v}^N.\end{aligned}$$

Reorganizing to have all terms for each $d_{\mathbf{q}}\mathbf{u}^i$ together:

$$\begin{aligned}d_{\mathbf{q}}\mathcal{L} &= \partial_{\mathbf{q}}\hat{J}^0 - \mathbf{p}_0^T\partial_{\mathbf{q}}\mathbf{g}^v - \boldsymbol{\mu}_0^T\partial_{\mathbf{q}}\mathbf{g}^u - \mathbf{p}_1^T\partial_{\mathbf{q}}M\mathbf{v}^0 + (\mathbf{p}_0^T - \mathbf{p}_1^T M)d_{\mathbf{q}}\mathbf{v}^0 + \\ &+ (\partial_{\mathbf{u}^i}\hat{J}^0 + \boldsymbol{\mu}_0^T - \boldsymbol{\mu}_1^T - \mathbf{p}_1^T\partial_{\mathbf{u}^0}\hat{\mathbf{h}}^1)d_{\mathbf{q}}\mathbf{u}^0 \\ &+ \sum_{i=1}^{N-1} \partial_{\mathbf{q}}\hat{J}^i - \mathbf{p}_i^T\partial_{\mathbf{q}}\hat{\mathbf{h}}^i + (\mathbf{p}_i^T - \mathbf{p}_{i+1}^T)\partial_{\mathbf{q}}M\mathbf{v}^i \\ &+ \sum_{i=1}^{N-1} (\boldsymbol{\mu}_i^T - \boldsymbol{\mu}_{i+1}^T + \partial_{\mathbf{u}^i}\hat{J}^i - \mathbf{p}_i^T\partial_{\mathbf{u}^i}\hat{\mathbf{h}}^i - \mathbf{p}_{i+1}^T\partial_{\mathbf{u}^i}\hat{\mathbf{h}}^{i+1})d_{\mathbf{q}}\mathbf{u}^i + \\ &+ ((\mathbf{p}_i^T - \mathbf{p}_{i+1}^T)M - \boldsymbol{\mu}_i^T\Delta t\,)d_{\mathbf{q}}\mathbf{v}^i \\ &+ \partial_{\mathbf{q}}\hat{J}^N - \mathbf{p}_N^T\partial_{\mathbf{q}}\hat{\mathbf{h}}^N + (\partial_{\mathbf{u}^i}\hat{J}^N - \mathbf{p}_N^T\partial_{\mathbf{u}^N}\hat{\mathbf{h}}^N + \boldsymbol{\mu}_N^T)d_{\mathbf{q}}\mathbf{u}^N + \\ &+ (\mathbf{p}_N^T M - \boldsymbol{\mu}_N^T\Delta t\,)d_{\mathbf{q}}\mathbf{v}^N + \mathbf{p}_N^T\partial_{\mathbf{q}}M\mathbf{v}^N.\end{aligned}$$

Introducing $\boldsymbol{\mu} = M^T\boldsymbol{\nu}$, we obtain the following adjoint equations from the terms multiplying $d_{\mathbf{q}}\mathbf{v}^i$ and $d_{\mathbf{q}}\mathbf{u}^i$ in the summation:

$$\boxed{\begin{aligned}\mathbf{p}_i - \mathbf{p}_{i+1} &= \Delta t\, \boldsymbol{\nu}_i, \\ M^T(\boldsymbol{\nu}_i - \boldsymbol{\nu}_{i+1}) &= (\partial_{\mathbf{u}^i}\hat{\mathbf{h}}^i)^T\mathbf{p}_i + (\partial_{\mathbf{u}^i}\hat{\mathbf{h}}^{i+1})^T\mathbf{p}_{i+1} - (\partial_{\mathbf{u}^i}\hat{J}^i)^T.\end{aligned}} \tag{41}$$

For the initial conditions we get from the terms multiplying $d_{\mathbf{q}}\mathbf{v}^N$ and $d_{\mathbf{q}}\mathbf{u}^N$:

$$\begin{aligned}\mathbf{p}_N &= \Delta t\, \boldsymbol{\nu}_N, \\ M^T\boldsymbol{\nu}_N &= (\partial_{\mathbf{u}^i}\hat{\mathbf{h}}^N)^T\mathbf{p}_N - (\partial_{\mathbf{u}^i}\hat{J}^N)^T.\end{aligned} \tag{42}$$

By introducing $\mathbf{p}_{N+1}$ and $\boldsymbol{\nu}_{N+1}$, the initial conditions can be simplified as

$$\boxed{\begin{aligned}\mathbf{p}_{N+1} &= 0, \\ \boldsymbol{\nu}_{N+1} &= 0.\end{aligned}} \tag{43}$$

For $\mathbf{p}_0, \boldsymbol{\nu}_0$ we have $M^T\boldsymbol{\nu}_0 = -(\partial_{\mathbf{u}^0}\hat{J}^0)^T + M^T\boldsymbol{\nu}_1 + \mathbf{p}_1^T\partial_{\mathbf{u}^0}\hat{\mathbf{h}}^1$ and $\mathbf{p}_0 = M^T\mathbf{p}_1$.

Finally, the expression for $d_{\mathbf{q}}J$ is obtained by dropping all terms with $d_{\mathbf{q}}\mathbf{v}^i$ and $d_{\mathbf{q}}\mathbf{u}^i$, as these are set to zero by our choice of equations for the adjoint, and retaining the rest:

$$\boxed{\begin{aligned}d_{\mathbf{q}}J &= \partial_{\mathbf{q}}\hat{J}^0 - \mathbf{p}_0^T\partial_{\mathbf{q}}\mathbf{g}^v - \boldsymbol{\mu}_0^T\partial_{\mathbf{q}}\mathbf{g}^u - \mathbf{p}_1^T\partial_{\mathbf{q}}M\mathbf{v}^0, \\ &+ \sum_{i=1}^{N} \partial_{\mathbf{q}}\hat{J}^i - \mathbf{p}_i^T\partial_{\mathbf{q}}\hat{\mathbf{h}}^i + \Delta t\, \boldsymbol{\nu}_i^T\partial_{\mathbf{q}}M\mathbf{v}^i.\end{aligned}} \tag{44}$$

### A.2 General BDF time integration

**Discrete Lagrangian.** For the general case, we split the Lagrangian $\mathcal{L}(\mathbf{u}, \mathbf{v}, \mathbf{p}, \boldsymbol{\mu}, \mathbf{q})$ into three parts: $J(\mathbf{u}, \mathbf{q})$ itself, the part $\mathcal{L}_c$ containing the Lagrange multipliers for the time steps $i = 1 \dots N$, and the part for initial conditions $\mathcal{L}_{in}$

$$\mathcal{L}(\mathbf{u}, \mathbf{v}, \mathbf{p}, \boldsymbol{\mu}, \mathbf{q}) = J(\mathbf{u}, \mathbf{q}) + \mathcal{L}_c(\mathbf{u}, \mathbf{v}, \mathbf{p}, \boldsymbol{\mu}, \mathbf{q}) + \mathcal{L}_{in}(\mathbf{u}^0, \mathbf{v}^0, \mathbf{p}^0, \boldsymbol{\mu}^0, \mathbf{q}),$$

where

$$\mathcal{L}_{in} = \mathbf{p}_0^T(\mathbf{v}^0 - \mathbf{g}^v) + \boldsymbol{\mu}_0^T(\mathbf{u}^0 - \mathbf{g}^u).$$

We start with $\mathcal{L}_c$. Remember that $\mathcal{L}_c$ depends on $h^i$, which has inputs $x$, $u^i$ and $u^{i-1}$ (due to friction):

$$\mathcal{L}_c = \sum_{i=1}^{N} \mathbf{p}_i^T M\left(\mathbf{v}^i + \sum_{j=1}^{\min(i,m)} \alpha_j^i \mathbf{v}^{i-j} - \hat{\mathbf{h}}^i\right) + \boldsymbol{\mu}_i^T\left(\mathbf{u}^i + \sum_{j=1}^{\min(i,m)} \alpha_j^i \mathbf{u}^{i-j} - \beta_i \Delta t\, \mathbf{v}^i\right).$$

We rearrange the double summations in this expression, so that each term depends only on $\mathbf{u}^i$ and $\mathbf{v}^i$, as the adjoint equations will be obtained by setting coefficients of $d_{\mathbf{q}}\mathbf{u}^i$ and $d_{\mathbf{q}}\mathbf{v}^i$ to zero after differentiation.

If we have a sum of the form

$$\sum_{i=1}^{N} \sum_{j=1}^{\min(i,m)} \alpha_j^i c_i^T z_{i-j},$$

we can change the summation order: let $r = i - j$,

$$\sum_{i=1}^{N} \sum_{r=\max(0,i-m)}^{i-1} \alpha_{i-r}^i c_i^T z_r = \sum_{r=0}^{N-1} \sum_{i=r+1}^{\min(r+m,N)} \alpha_{i-r}^i c_i^T z_r = \sum_{r=0}^{N-1} \sum_{j=1}^{\min(m,N-r)} \alpha_j^{j+r} c_{r+j}^T z_r,$$

where we introduced back $j = i - r$ in the last equation. Finally, renaming $r$ to $i$, we obtain the form for which each term contains $z_i$ only:

$$\sum_{i=0}^{N-1} \left( \sum_{j=1}^{\min(m,N-i)} \alpha_j^{i+j} c_{i+j}^T \right) z_i. \tag{45}$$

Returning to the Lagrangian, we regroup the terms in $\mathcal{L}$ as:

$$\mathcal{L}_c = \sum_{i=1}^{N} \left( \mathbf{p}_i^T \left( M\mathbf{v}^i - \hat{\mathbf{h}}^i \right) + \boldsymbol{\mu}_i^T \left( \mathbf{u}^i - \beta_i \Delta t\, \mathbf{v}^i \right) \right) + \sum_{i=1}^{N} \sum_{j=1}^{\min(i,m)} \left( \mathbf{p}_i^T M \alpha_j^i \mathbf{v}^{i-j} + \boldsymbol{\mu}_i^T \alpha_j^i \mathbf{u}^{i-j} \right).$$

Using (45), we get

$$\mathcal{L}_c = \sum_{i=1}^{N} \left( \mathbf{p}_i^T \left( M\mathbf{v}^i - \hat{\mathbf{h}}^i \right) + \boldsymbol{\mu}_i^T \left( \mathbf{u}^i - \beta_i \Delta t\, \mathbf{v}^i \right) \right) + \sum_{i=0}^{N-1} \sum_{j=1}^{\min(m,N-i)} \left( \mathbf{p}_{i+j}^T M \alpha_j^{i+j} \mathbf{v}^i + \boldsymbol{\mu}_{i+j}^T \alpha_j^{i+j} \mathbf{u}^i \right).$$

Collecting the terms for $\mathbf{u}^i$ and $\mathbf{v}^i$:

$$\begin{aligned}
&\mathcal{L}_c = \\
&\sum_{i=1}^{N-1} -\mathbf{p}_i^T \hat{\mathbf{h}}^i + \left( \left( \mathbf{p}_i^T + \sum_{j=1}^{\min(m,N-i)} \alpha_j^{i+j} \mathbf{p}_{i+j}^T \right) M - \beta_i \Delta t\, \boldsymbol{\mu}_i^T \right) \mathbf{v}^i + \\
&+ \left( \boldsymbol{\mu}_i^T + \sum_{j=1}^{\min(m,N-i)} \alpha_j^{i+j} \boldsymbol{\mu}_{i+j}^T \right) \mathbf{u}^i + \\
&\sum_{j=1}^{m} \mathbf{p}_j^T M \alpha_j^j \mathbf{v}^0 + \boldsymbol{\mu}_j^T \alpha_j^j \mathbf{u}^0 + \\
&- \mathbf{p}_N^T \hat{\mathbf{h}}^N + (\mathbf{p}_N^T M - \beta_N \Delta t\, \boldsymbol{\mu}_N^T) \mathbf{v}^N + \boldsymbol{\mu}_N^T \mathbf{u}^N.
\end{aligned}$$

We split this expression again, into $\mathcal{L}_c^{mid} + \mathcal{L}_c^0 + \mathcal{L}_c^N$, corresponding to three lines of the equation; these terms contribute to the time-dependent adjoint equations and boundary conditions. In this form, it is straightforward to differentiate with respect to $q$:

$$\begin{aligned}
d_{\mathbf{q}} \mathcal{L}_c^{mid} &= \\
&\sum_{i=1}^{N-1} -\mathbf{p}_i^T \partial_{\mathbf{q}} \hat{\mathbf{h}}^i + \left( \mathbf{p}_i^T + \sum_{j=1}^{\min(m,N-i)} \alpha_j^{i+j} \mathbf{p}_{i+j}^T \right) d_{\mathbf{q}} M \mathbf{v}^i + \\
&\sum_{i=1}^{N-1} \left( \left( \mathbf{p}_i^T + \sum_{j=1}^{\min(m,N-i)} \alpha_j^{i+j} \mathbf{p}_{i+j}^T \right) M - \beta_i \Delta t\, \boldsymbol{\mu}_i^T \right) d_{\mathbf{q}} \mathbf{v}^i + \\
&+ \left( \boldsymbol{\mu}_i^T + \sum_{j=1}^{\min(m,N-i)} \alpha_j^{i+j} \boldsymbol{\mu}_{i+j}^T - \mathbf{p}_i^T \partial_{\mathbf{u}^i} \hat{\mathbf{h}}^i - \mathbf{p}_{i+1}^T \partial_{\mathbf{u}^i} \hat{\mathbf{h}}^{i+1} \right) d_{\mathbf{q}} \mathbf{u}^i + \\
&- \mathbf{p}_1^T \partial_{\mathbf{u}^0} \hat{\mathbf{h}}^1 \, d_{\mathbf{q}} \mathbf{u}^0 \\
d_{\mathbf{q}} \mathcal{L}_c^0 &= \sum_{j=1}^{m} \alpha_j^j \left( \mathbf{p}_j^T d_{\mathbf{q}} M \mathbf{v}^0 + \mathbf{p}_j^T M d_{\mathbf{q}} \mathbf{v}^0 + \boldsymbol{\mu}_j^T d_{\mathbf{q}} \mathbf{u}^0 \right) \\
d_{\mathbf{q}} \mathcal{L}_c^N &= -\mathbf{p}_N^T \partial_{\mathbf{q}} \hat{\mathbf{h}}^N - \mathbf{p}_N^T \partial_{\mathbf{u}^N} \hat{\mathbf{h}}^N d_{\mathbf{q}} \mathbf{u}^N + \mathbf{p}_N^T d_{\mathbf{q}} M \mathbf{v}^N + \\
&+ (\mathbf{p}_N^T M - \beta_N \Delta t\, \boldsymbol{\mu}_N^T) d_{\mathbf{q}} \mathbf{v}^N + \boldsymbol{\mu}_N^T d_{\mathbf{q}} \mathbf{u}^N.
\end{aligned}$$

Similarly, we split

$$d_{\mathbf{q}} J = \sum_{i=1}^{N-1} \partial_{\mathbf{q}} \hat{J}^i + \sum_{i=1}^{N-1} \partial_{\mathbf{u}} \hat{J}^i d_{\mathbf{q}} \mathbf{u}^i + (\partial_{\mathbf{q}} \hat{J}^0 + \partial_{\mathbf{u}} \hat{J}^0 d_{\mathbf{q}} \mathbf{u}^0) + (\partial_{\mathbf{q}} \hat{J}^N + \partial_{\mathbf{u}} \hat{J}^N d_{\mathbf{q}} \mathbf{u}^N) = d_{\mathbf{q}} J^{mid} + d_{\mathbf{q}} J^0 + d_{\mathbf{q}} J^N.$$

**Adjoint equations.** Equating the coefficients of $d_{\mathbf{q}} \mathbf{u}^i$ and $d_{\mathbf{q}} \mathbf{v}^i$, $i = 1 \dots N-1$ to zero in $d_{\mathbf{q}} \mathcal{L}_c^{mid} + d_{\mathbf{q}} J^{mid}$, we obtain the adjoint equations:

$$\begin{aligned}
&M^T \left( \mathbf{p}_i + \sum_{j=1}^{\min(m,N-i)} \alpha_j^{i+j} \mathbf{p}_{i+j} \right) = \beta_i \Delta t\, \boldsymbol{\mu}_i, \\
&\boldsymbol{\mu}_i + \sum_{j=1}^{\min(m,N-i)} \alpha_j^{i+j} \boldsymbol{\mu}_{i+j} = (\partial_{\mathbf{u}^i} \hat{\mathbf{h}}^i)^T \mathbf{p}_i + (\partial_{\mathbf{u}^i} \hat{\mathbf{h}}^{i+1})^T \mathbf{p}_{i+1} - (\partial_{\mathbf{u}} \hat{J}^i)^T,
\end{aligned} \tag{46}$$

for $i = 1 \dots N-1$.

Making a substitution $\boldsymbol{\mu} = M^T \hat{\boldsymbol{\nu}}$, we obtain (12).

We obtain the adjoint equation in time in the form very similar to the forward equations (39). The most important difference is that the integration is "back in time", i.e., the finite difference formula for time derivative is applied to $i, \dots i+m$. This means that the system is integrated backwards, starting with $(\mathbf{p}_N, \boldsymbol{\mu}_N)$. Second, there is a slight difference in the coefficients of the scheme used. Specifically, the starting iterations do *not* use the lower-order BDF formulas, rather truncations of the same order BDF formula. At the same time, the end iterations, for small $i$, will use lower order coefficients, even though this is not needed. The reason for preferring this (although this seemingly damages the accuracy of the integration of the adjoint) is consistency with the functional discretization: as this fact is a consequence of deriving the adjoint from the time discretization, if we compute the functional using the same discretization, finite differences for the functional will be closer to the adjoint.

**Initial conditions for adjoint.** The initial conditions follow from setting coefficients of $d_{\mathbf{q}} \mathbf{u}^N$ and $d_{\mathbf{q}} \mathbf{v}^N$ to zero in $d_{\mathbf{q}} \mathcal{L}_c^N d_{\mathbf{q}} J^N$, i.e.

$$(\partial_{\mathbf{u}} \hat{J}^N)^T - \partial_{\mathbf{u}} \hat{\mathbf{h}}^N \mathbf{p}_N + \boldsymbol{\mu}_N = 0; \; M^T \mathbf{p}_N - \beta_N \Delta t\, \boldsymbol{\mu}_N = 0.$$

Substituting $\boldsymbol{\mu} = M^T \boldsymbol{\nu}$, we get

$$(\partial_{\mathbf{u}} \hat{J}^N)^T - \partial_{\mathbf{u}^N} \hat{\mathbf{h}}^N \mathbf{p}_N + M^T \boldsymbol{\nu}_N = 0; \; \mathbf{p}_N - \beta_N \Delta t\, \boldsymbol{\nu}_N = 0,$$

and a linear system for for $\boldsymbol{\nu}_N$:

$$(\partial_{\mathbf{u}} \hat{J}^N)^T + (M^T - \beta_N \Delta t\, \partial_{\mathbf{u}^N} \hat{\mathbf{h}}^N) \boldsymbol{\nu}_N = 0.$$

Solving these

$$(M^T - \beta_N \Delta t\, \partial_{\mathbf{u}^N} \hat{\mathbf{h}}^N) \boldsymbol{\nu}_N = -(\partial_{\mathbf{u}} \hat{J}^N)^T, \; \mathbf{p}_N = \beta_N \Delta t\, \boldsymbol{\nu}_N. \tag{47}$$

By introducing $\mathbf{p}_{N+1}, \; \boldsymbol{\nu}_{N+1}$, the initial condition can be simplified as (13).

Finally, the adjoint equations (12) only allow to solve down to to $i = 1$; the equations for $\mathbf{p}_0, \boldsymbol{\mu}_0$ are derived from $d_{\mathbf{q}} J^0 + d_{\mathbf{q}} \mathcal{L}_{in} + d_{\mathbf{q}} \mathcal{L}_c^0$; adding terms containing $d_{\mathbf{q}} \mathbf{u}^0$ and $d_{\mathbf{q}} \mathbf{v}^0$, we get:

$$\left( \partial_{\mathbf{u}} \hat{J}^0 + \boldsymbol{\mu}_0^T + \sum_{j=1}^{m} \alpha_j^j \boldsymbol{\mu}_j^T - \mathbf{p}_1^T \partial_{\mathbf{u}^0} \hat{\mathbf{h}}^1 \right) d_{\mathbf{q}} \mathbf{u}^0 + \left( \mathbf{p}_0^T + \sum_{j=1}^{m} \alpha_j^j \mathbf{p}_j^T M \right) d_{\mathbf{q}} \mathbf{v}^0,$$

which yields direct expressions (14) for $\mathbf{p}_0$ and $\boldsymbol{\mu}_0$, based on $\mathbf{p}_i, \boldsymbol{\mu}_i$ for $i = 1 \dots m$.

**Computing the derivative of $J$ from the forward and adjoint solutions.** Finally, once the adjoint variables are obtained, we can compute (15), by collecting all terms not containing $d_{\mathbf{q}} \mathbf{u}^i$ and $d_{\mathbf{q}} \mathbf{v}^i$.

Partial derivatives $\partial_{\mathbf{q}} \hat{\mathbf{h}}, \partial_{\mathbf{u}} \hat{\mathbf{h}}$ and $\partial_{\mathbf{q}} \hat{J}_i, \partial_{\mathbf{u}} \hat{J}_i$ are exactly the same as used in the construction of the system for static adjoint and computation of the functional. The differences, specific to time discretization, are:

- Mass matrix derivative $d_{\mathbf{q}} M$. See Section A.3.
- Partial derivatives of the initial conditions with respect to parameters $\partial_{\mathbf{q}} \mathbf{g}^v$ and $\partial_{\mathbf{q}} \mathbf{g}^u$, for positions and velocities (See Appendix A.4). Typically, a 3D position and velocity for the whole

object (or angular velocity for the object rotating as a rigid body) are used as parameters, so these are trivial to compute.

### A.3 Mass matrix derivative

Consider our Mass Matrix as follows:

$$M_{Ds+i,Dt+i} = \sum_{e \in E(s) \cap E(t)} \int_{\bar{q}^e(\hat{K}_e)} \rho(\mathbf{q})\, \phi^{\mathrm{loc}_e(s)}(x)\ \phi^{\mathrm{loc}_e(t)}(x)\ dx,$$

where $i \in \{1, .., D\}$ and $D$ equals 2 or 3 (representing dimension). This means mass matrix $M$ has $D \cdot n$ rows and columns. Here, we use notation to define the local index of a node $\mathrm{loc}_e(\ell)$ with respect to elements $e$ containing it.

Then, we can obtain the shape derivative with respect to perturbation $\theta$ ($x^\epsilon = x + \epsilon\theta(x)$) by computing the Gateaux Derivative below for each element:

$$\begin{aligned}
\partial_q M_{Ds+i,Dt+i} &= \frac{d}{d\epsilon}\Big|_{\epsilon=0} \sum_{e \in E(s) \cap E(t)} \int_{\bar{q}^e(\hat{K}_e)^\epsilon} \rho(\mathbf{q})\, \phi^{\mathrm{loc}_e(s)}(x^\epsilon)\ \phi^{\mathrm{loc}_e(t)}(x^\epsilon)\ dx^\epsilon \\
&= \sum_{e \in E(s) \cap E(t)} \int_{\bar{q}^e(\hat{K}_e)} \partial_{\mathbf{q}}\rho(\mathbf{q})\, \phi^{\mathrm{loc}_e(s)}(x)\ \phi^{\mathrm{loc}_e(t)}(x) + \\
&\quad + \rho(\mathbf{q})\, \phi^{\mathrm{loc}_e(s)}(x)\ \phi^{\mathrm{loc}_e(t)}(x)\ \nabla \cdot \theta(x)\ dx \\
&= \sum_{e \in E(s) \cap E(t)} \sum_{l \in \mathrm{Loc}_e} \int_{\bar{q}^e(\hat{K}_e)} \partial_{\mathbf{q}}\rho(\mathbf{q})\, \phi^{\mathrm{loc}_e(s)}(x)\ \phi^{\mathrm{loc}_e(t)}(x) + \\
&\quad + \rho(\mathbf{q})\, \phi^{\mathrm{loc}_e(s)}\ \phi^{\mathrm{loc}_e(t)}\ \nabla\xi^l\ dx \cdot \theta^l.
\end{aligned}$$

### A.4 Initial condition derivatives

We need to compute partial derivatives of the initial conditions with respect to optimization parameters $\mathbf{q}$, $\partial_{\mathbf{q}}\mathbf{g}^v$ and $\partial_{\mathbf{q}}\mathbf{g}^u$, for positions and velocities. Notice that both $\partial_{\mathbf{q}}\mathbf{g}^v$ and $\partial_{\mathbf{q}}\mathbf{g}^u$ are discrete vector fields on domain $\Omega_{\bar{\mathbf{q}}}$. Consider we have one vector value $\mathbf{q}^m$ per node of the domain.

If $(\mathbf{g}^v)_s = \mathbf{q}^m$, where $(\mathbf{g}^v)_s$ is initial condition at node $s$, the derivative with respect to $q_m$ is simply the identity matrix ($\partial_{\mathbf{q}^m}(\mathbf{g}^v)_s = I$). At the same time, it is the zero matrix w.r.t. any other $q^{m^*}$, with $m^* \neq m$. Same thing goes for $\mathbf{g}^u$.

## B PARAMETRIC DERIVATIVES OF FORCES

In this section, we derive general expressions for gradient-dependent volume forces.

In a general form, the contribution to the PDE can be written as

$$\mathcal{H}^v(u, w, Q) = \int_{\Omega_{\bar{q}}} f^v((\nabla u(x), q(x)) : \nabla w\, dx.$$

### B.1 Gradient-dependent volume forces

**Shape derivatives.** we omit the dependence on $\mathbf{q}$, and use $\nabla f$ to denote $\partial_{\nabla u} f$.

Define $\Omega_\epsilon = \Omega_{\bar{\mathbf{q}}+\theta\epsilon}$, $\Omega = \Omega_{\bar{\mathbf{q}}}$ and $x^\epsilon = x + \epsilon\theta$. Let $u^\epsilon$ be the solution on domain $\Omega_\epsilon$. Then computing the Gâteaux derivative of $\mathcal{H}^v$ we get:

$$\begin{aligned}
\frac{d}{d\epsilon}\Big|_{\epsilon=0} \mathcal{H}^f &= \frac{d}{d\epsilon}\Big|_{\epsilon=0} \int_{\Omega_\epsilon} f(\nabla_{x^\epsilon} u^\epsilon) : \nabla_{x^\epsilon} w^\epsilon\ dx^\epsilon \\
&= \frac{d}{d\epsilon}\Big|_{\epsilon=0} \int_\Omega f((\nabla u)F_\epsilon^{-1}) : (\nabla w)F_\epsilon^{-1}\ \det F_\epsilon\ dx \\
&= \int_\Omega \frac{d}{d\epsilon}\Big|_{\epsilon=0} \Big(f((\nabla u)F_\epsilon^{-1})F_\epsilon^{-T} : \nabla w\ \det F_\epsilon\Big)\ dx \\
&= \int_\Omega -f(\nabla u)\nabla\theta^T : \nabla w + \boxed{(\nabla f(\nabla u) : \nabla\delta u) : \nabla w} + \\
&\quad -(\nabla f(\nabla u) : (\nabla u \nabla\theta)) : \nabla w + (f(\nabla u) : \nabla w)\nabla \cdot \theta\ dx.
\end{aligned} \tag{48}$$

Thus we have for the shape derivative contribution:

$$\boxed{B^f(\theta, p) = \int_\Omega -f(\nabla u)\nabla\theta^T : \nabla p - (\nabla f(\nabla u) : (\nabla u \nabla\theta)) : \nabla p + (f(\nabla u) : \nabla p)\nabla \cdot \theta\ dx.}$$

$B^f(\theta, p)$ is linear in $\theta$ and $p$, and we convert it to a matrix form by substituting basis functions for $\theta$ and $p$:

$$\begin{aligned}
[B^f]_{Da+i,Db+j} = &\sum_{e \in E(a) \cap E(b)} \sum_{k,l \in 1..D} \delta_{i,j} \int_{\bar{q}^e(\hat{K}_e)} -[\nabla\xi^{\mathrm{loc}_e(b)}]_k f_{kl} [\nabla\phi^{\mathrm{loc}_e(a)}]_l\ dx + \\
+ &\sum_{e \in E(a) \cap E(b)} \sum_{k,l,m \in 1..D} \int_{\bar{q}^e(\hat{K}_e)} -\nabla f(\nabla u)_{iklm} [\nabla\xi^{\mathrm{loc}_e(b)}]_l [\nabla u]_{jm} [\nabla\varphi^{\mathrm{loc}_e(a)}]_k\ dx + \\
+ &\sum_{e \in E(a) \cap E(b)} \sum_{k \in 1..D} \int_{\bar{q}^e(\hat{K}_e)} f(\nabla u)_{ik} [\nabla\phi^{\mathrm{loc}_e(a)}]_k [\nabla\xi^{\mathrm{loc}_e(b)}]_j\ dx.
\end{aligned}$$

the sum is over elements $e$ containing both $a$ and $b$. Again, we use notation $\mathrm{loc}_e(\ell)$ to define the local index of a node with respect to the elements $e$ containing it.

The contribution to the left-hand side of the adjoint equation is

$$\boxed{A^f(\psi, p) = \int_\Omega (\nabla f(\nabla u) : \nabla\psi) : \nabla p\, dx,}$$

which is the boxed term from (48), corresponding to $w^T \partial_{\mathbf{u}} h\, \delta u$, with replacements $w := p$ and $\delta u := \psi$. Discretizing according to our FE basis:

$$[A^f]_{Da+i,Db+j} = \sum_{e \in E(a) \cap E(b)} \sum_{k,l \in 1..D} \int_{\bar{q}^e(\hat{K}_e)} (\nabla f)_{ikjl} [\nabla\phi^{\mathrm{loc}_e(b)}]_l [\nabla\phi^{\mathrm{loc}_e(a)}]_k\ dx,$$

where we sum over all elements $\Omega_e = \bar{q}(\hat{K})$, with $\hat{K}$ being the reference element.

**Non-shape volumetric parameter derivatives.** We assume that the force depends on $q = q(x)$, a function of the point in $\Omega_{\bar{q}}$, defined by its values $\mathbf{q}$ at the same nodes as the solution, and interpolated using the same basis $\phi$.

The perturbed parameter function $q$ is defined as

$$q^\epsilon(x) = q(x) + \epsilon\theta(x),$$

where $\theta(x)$ represents the perturabtion, assumed to be given in the same basis as $q$ and solution.

$$\begin{aligned}
\frac{d}{d\epsilon}\Big|_{\epsilon=0} \mathcal{H}^v &= \frac{d}{dt}\Big|_{\epsilon=0} \int_{\Omega_\epsilon} f(\nabla u^\epsilon, q^\epsilon) : \nabla w^\epsilon\ dx^\epsilon \\
&= \int_\Omega (\nabla_1 f : \nabla\delta u) : \nabla w\ +\ (\nabla_2 f \cdot \frac{d}{d\epsilon} q^\epsilon) : \nabla w\ dx \\
&= \int_\Omega \boxed{(\nabla_1 f : \nabla\delta u) : \nabla w}\ +\ (\nabla_2 f \cdot \theta) : \nabla w\ dx.
\end{aligned} \tag{49}$$

Thus, the shape derivative contribution is:

$$\boxed{B^f(\theta, p) = \int_\Omega (\nabla_2 f \cdot \theta) : \nabla p \; dx.}$$

Discretizing:

$$[B^f]_{D_s a+i, D_s b+j} = \sum_{e \in E(a) \cap E(b)} \sum_{k \in 1..D_d} \int_{\bar{q}^e(\hat{K}_e)} [\nabla_2 f]_{ikj} \xi^{\mathrm{loc}_e(b)} [\nabla \phi^{\mathrm{loc}_e(a)}]_k \; dx.$$

The contribution to the left-hand side of the adjoint equation is

$$\boxed{A^f(\psi, p) = \int_\Omega (\nabla_1 f : \nabla \psi) : \nabla p \, dx,}$$

which is the boxed term from (49), depending on $\delta u$ with replacements $w := p$ and $\delta u := \psi$.

Discretizing according to our FE basis

$$[A^f]_{D_s a+i, D_s b+j} = \sum_{e \in E(a) \cap E(b)} \sum_{k,l \in 1..D_d} \int_{\bar{q}^e(\hat{K}_e)} (\nabla_1 f)_{ikjl} [\nabla \phi^{\mathrm{loc}_e(b)}]_l [\nabla \phi^{\mathrm{loc}_e(a)}]_k \; dx.$$

## C GENERAL FORM OF OBJECTIVE DERIVATIVES

For each objective $J$, the derivations below include vectors $R^o$ and $S^o$, corresponding to $\partial_u J$ and $\partial_q J$, which are necessary to compute the adjoint solution and the final shape derivative.

### C.1 Objectives depending on gradient of solution and shape

Consider an objective that depends on both the solution of the PDE and the domain :

$$J(\nabla u, \Omega) = \int_\Omega j(\nabla u, x) dx. \tag{50}$$

Computing the Gateaux derivative, while considering perturbation of the domain $x^\epsilon := x + \epsilon\theta$:

$$\begin{aligned}
\frac{d}{d\epsilon}\Big|_{t=0} J &= \frac{d}{d\epsilon}\Big|_{\epsilon=0} \int_{\Omega_\epsilon} j(\nabla u^\epsilon, x^\epsilon) \; dx^\epsilon \\
&= \frac{d}{d\epsilon}\Big|_{\epsilon=0} \int_\Omega j((\nabla u) F_\epsilon^{-1}, x + \epsilon\theta) \det(F_\epsilon) \; dx \\
&= \int_\Omega \frac{d}{d\epsilon}\Big|_{\epsilon=0} \Big( j((\nabla u) F_\epsilon^{-1}, x + \epsilon\theta) \det(F_\epsilon) \Big) \; dx \\
&= \int_\Omega \boxed{\nabla_1 j : \nabla \delta u} - \nabla_1 j : \nabla u \nabla \theta + \nabla_2 j \cdot \theta + j(\nabla u, x) \nabla \cdot \theta \; dx.
\end{aligned}$$

We can select the parts not depending on $\delta u$ to be part of $S$:

$$S^o(\theta) = \int_\Omega -\nabla_1 j : \nabla u \nabla \theta + \nabla_2 j \cdot \theta + j(\nabla u, x) \nabla \cdot \theta \; dx. \tag{51}$$

Discretizing according to our FE basis:

$$\begin{aligned}
[S^o]_{Da+i} = \sum_{e \in E(a)} \int_{\bar{q}^e(\hat{K}_e)} & -(\nabla u^T)_{ij} (\nabla_1 j)_{jk} [\nabla \xi^{\mathrm{loc}_e(a)}]_k + \\
& + \frac{\partial j}{\partial x_i} \xi^{\mathrm{loc}_e(a)} + j(u, x) [\nabla \xi^{\mathrm{loc}_e(a)}]_i \; dx.
\end{aligned}$$

And,

$$R^o(\psi) = \int_\Omega \nabla_1 j : \nabla \psi \; dx, \tag{52}$$

which can be discretized as follows:

$$[R^o]_{Da+i} = \sum_{e \in E(a)} \int_{\bar{q}^e(\hat{K}_e)} (\nabla_1 j)_{ij} \; [\nabla \phi^{\mathrm{loc}_e(a)}]_j \; dx.$$

### C.2 Objectives depending on solution and shape

Consider an objective that depends on both the solution of the PDE and the domain:

$$J(u, \Omega) = \int_\Omega j(u, x) dx. \tag{53}$$

Computing the Gateaux derivative, while considering perturbation of the domain $x^\epsilon := x + \epsilon\theta$:

$$\begin{aligned}
\frac{d}{d\epsilon}\Big|_{\epsilon=0} J &= \frac{d}{d\epsilon}\Big|_{\epsilon=0} \int_{\Omega_\epsilon} j(u^\epsilon, x^\epsilon) \; dx^\epsilon \\
&= \int_\Omega \boxed{\nabla_1 j \cdot \delta u} + \nabla_2 j \cdot \theta + j \nabla \cdot \theta \; dx.
\end{aligned}$$

We can select the parts depending on $\delta u$, which will be the rhs of our adjoint PDE (represented by vector $R$), while the remaining part is a term that should be added directly to the shape derivative (vector $S$).

So,

$$S^o(\theta) = \int_\Omega \nabla_2 j \cdot \theta + j(u, x) \nabla \cdot \theta \; dx. \tag{54}$$

Discretizing according to our FE basis:

$$[S]_{Da+i} = \sum_{e \in E(a)} \int_{\bar{q}^e(\hat{K}_e)} \frac{\partial j}{\partial x_i} \xi^{\mathrm{loc}_e(a)} + j(u, x) [\nabla \xi^{\mathrm{loc}_e(a)}]_i \; dx.$$

And,

$$R^o(\psi) = \int_\Omega \nabla_1 j \cdot \psi \; dx, \tag{55}$$

which can be discretized as follows:

$$[R]_{Da+i} = \sum_{e \in E(a)} \int_{\bar{q}^e(\hat{K}_e)} \frac{\partial j}{\partial u_i} \; \phi^{\mathrm{loc}_e(a)} \; dx.$$

## D CONTACT AND FRICTION AREA TERM

In our contact and friction formulas, we use $A_k$ as a weight for our forces, which measures the area of our contact pair $k$. In the formulation, it corresponds to the sum of surface areas associated with each primitive. In 3D, it is 1/3 of the sum of areas of incident triangles for vertices and edges, and the area of triangles. For a triangle $T = (t_0, t_1, t_2)$, where $t_i$ corresponds to the position of each triangle's vertex, the corresponding triangle area will be:

$$A_\Delta(T) = A_\Delta(t_0, t_1, t_2) = \tfrac{1}{2} \|(t_1 - t_0) \times (t_2 - t_0)\|.$$

If $k$ corresponds to a point-triangle contact pair between point $p$ and triangle $T$, and Incid(p) has the incident triangles of $p$, we have:

$$A_k = \sum_{T \in \mathrm{Incid}(p)} \tfrac{1}{3} A_\Delta(T).$$

In this context, $\partial_{\bar{\mathbf{q}}} A_k$ corresponds to the gradient of the area term, which can be computed as a sum of the $\partial_{\bar{\mathbf{q}}} A_\Delta$ terms:

$$\partial_{\bar{\mathbf{q}}} A_\Delta(T) = \frac{(t_1 - t_0) \times (t_2 - t_0)}{2\|(t_1 - t_0) \times (t_2 - t_0)\|} \partial_{\bar{\mathbf{q}}}((t_1 - t_0) \times (t_2 - t_0)).$$

## E FRICTION DERIVATIVE TERMS

For friction, we have:

$$B^f(p, \theta) = \sum_k \partial_{\bar{\mathbf{q}}} F_k^f s\theta \cdot p\, A_k + F_k^f \cdot p\ \partial_{\bar{\mathbf{q}}} A_k\ A_k,$$

and

$$A^f(\psi, p) = \sum_k \partial_{\mathbf{u}} F_k \psi \cdot p\ A_k,$$

which reduces to computing the derivative of each $F_k^f$ term with respect to $x$, $u^i$ and $u^{i-1}$.

$$\begin{aligned}
\partial_{x_\ell} F_k^f = &-\gamma_{k_1,k_2}\ T_k f_\eta(\|\tau_k\|) \frac{\tau_k}{\|\tau_k\|} \times \\
&\left(\kappa \frac{N_k}{\|N_k\|} \cdot (b''(\partial_{\mathbf{x}}\mathbf{d}\, d_k)(\partial_{\mathbf{x}}\mathbf{d}\, d_k)^T + b' \partial_{\mathbf{x}}\mathbf{d}(\partial_{\mathbf{x}}\mathbf{d}\, d_k))\ M^*\right)_\ell + \\
&- \gamma_{k_1,k_2}\ N_k (\partial_{\mathbf{x}}\mathbf{p}\, T_k\, M^*)_\ell f_\eta(\|\tau_k\|) \frac{\tau_k}{\|\tau_k\|} + \\
&- \gamma_{k_1,k_2}\ N_k T_k \frac{\tau_k}{\|\tau_k\|}\left(f_\eta' \frac{\tau_k}{\|\tau_k\|} \cdot ((\partial_{\mathbf{x}}\mathbf{p}\, T_k\, M^*)_\ell^T (\mathbf{u}^i - \mathbf{u}^{i-1}))\right) + \\
&- \gamma_{k_1,k_2}\ N_k T_k f_\eta(\|\tau_k\|)\left(\left(\frac{I_2}{\|\tau_k\|} - \frac{\tau_k \tau_k^T}{\|\tau_k\|^3}\right)(\partial_{\mathbf{x}}\mathbf{p}\, T_k\, M^*)_\ell^T (\mathbf{u}^i - \mathbf{u}^{i-1})\right).
\end{aligned} \tag{56}$$

$$\begin{aligned}
\partial_{u_\ell^i} F_k^f = &-\gamma_{k_1,k_2}\ N_k T_k \frac{\tau_k}{\|\tau_k\|}\left(f_\eta' \frac{\tau_k}{\|\tau_k\|} \cdot \left(T_k^T\right)_\ell\right) + \\
&- \gamma_{k_1,k_2}\ N_k T_k f_\eta(\|\tau_k\|)\left(\left(\frac{I_2}{\|\tau_k\|} - \frac{\tau_k \tau_k^T}{\|\tau_k\|^3}\right)\left(T_k^T\right)_\ell\right).
\end{aligned} \tag{57}$$

$$\begin{aligned}
\partial_{u_\ell^{i-1}} F_k^f = &-\gamma_{k_1,k_2}\ T_k f_\eta(\|\tau_k\|) \frac{\tau_k}{\|\tau_k\|} \times \\
&\left(\kappa \frac{N_k}{\|N_k\|} \cdot (b'' \nabla d_k \nabla d_k^T + b' \nabla^2 d_k)\right)_\ell + \\
&- \gamma_{k_1,k_2}\ N_k (\partial_{\mathbf{x}}\mathbf{p}\, T_k)_\ell f_\eta(\|\tau_k\|) \frac{\tau_k}{\|\tau_k\|} + \\
&- \gamma_{k_1,k_2}\ N_k T_k \frac{\tau_k}{\|\tau_k\|}\left(f_\eta' \frac{\tau_k}{\|\tau_k\|} \cdot (\partial_{\mathbf{x}}\mathbf{p}\, T_k)_\ell^T (\mathbf{u}^i - \mathbf{u}^{i-1}))\right) + \\
&- \gamma_{k_1,k_2}\ N_k T_k f_\eta(\|\tau_k\|)\left(\left(\frac{I_2}{\|\tau_k\|} - \frac{\tau_k \tau_k^T}{\|\tau_k\|^3}\right)(\partial_{\mathbf{x}}\mathbf{p}\, T_k)_\ell^T (\mathbf{u}^i - \mathbf{u}^{i-1})\right).
\end{aligned} \tag{58}$$

## F REGULARIZATION DERIVATIVES

**Scale-invariant smoothing.** The regularization in (37) is used for shape optimization, when the optimization parameter is $q_m = v_i$, a vertex of the shape. That said, the derivative with respect to each vertex $v_i$ is:

$$\partial_{v_i} J^{\text{smooth}} = p\|s_i\|^{p-2} s_i^T (\partial_{v_i} s_i) + \sum_{j \in N(i) \cap B} p\|s_j\|^{p-2} s_j^T (\partial_{v_i} s_j).$$

And we have that

$$\partial_{v_i} s_i = \frac{|N(i) \cap B| I}{\sum_{j \in N(i) \cap B} \|v_i - v_j\|} - \frac{\left(\sum_{j \in N(i) \cap B} \frac{v_i - v_j}{\|v_i - v_j\|}\right)\left(\sum_{j \in N(i) \cap B}(v_i - v_j)\right)^T}{\left(\sum_{j \in N(i) \cap B} \|v_i - v_j\|\right)^2}.$$

And, for $\partial_{v_i} s_j$, where $v_i$ is one of the neighbors of $v_j$:

$$\partial_{v_i} s_j = -\frac{I}{\sum_{k \in N(j) \cap B} \|v_j - v_k\|} + \frac{\left(\frac{v_j - v_i}{\|v_j - v_i\|}\right)\left(\sum_{k \in N(j) \cap B}(v_j - v_k)\right)^T}{\left(\sum_{k \in N(j) \cap B} \|v_j - v_k\|\right)^2}.$$

**Material parameter spatial smoothing.** For derivatives of (38) with respect to material parameters $\lambda_i, \mu_i$ we have

$$\partial_{\lambda_i} J^{\lambda,\mu \text{ smooth}} = 2 \sum_{t' \in Adj(t_i)} \left(\frac{\lambda_{t_i}}{\lambda_{t'}} - 1\right) + \left(1 - \frac{\lambda_{t'}}{\lambda_{t_i}}\right) \frac{\lambda_{t'}}{\lambda_{t_i}^2},$$

and

$$\partial_{\mu_i} J^{\lambda,\mu \text{ smooth}} = 2 \sum_{t' \in Adj(t_i)} \left(\frac{\mu_{t_i}}{\mu_{t'}} - 1\right) + \left(1 - \frac{\mu_{t'}}{\mu_{t_i}}\right) \frac{\mu_{t'}}{\mu_{t_i}^2}.$$

## G DIFFERENCE BETWEEN "OPTIMIZE-THEN-DISCRETIZE" AND "DISCRETIZE-THEN-OPTIMIZE"

There is a well-established theory showing that the equations derived through the Optimize-then-Discretize are the correct equations for optimality. This is, in general, not guaranteed for the "Discretize-then-Optimize" approach; the easiest approach is to ensure that for a choice of discretization methods, the results of both approaches are identical (which is what we do, although further analysis is needed to make any rigorous claims).

Specifically for shape optimization, "Optimize-then-Discretize" makes it possible to derive the gradients in the physical domain: “shape derivative calculus” [Allaire et al. 2021] allows one to compute shape derivatives with respect to changes in the shape of the domain on which PDE is solved using physical domain variables in which the PDEs have the standard form, e.g. for Poisson or elasticity, are expressed in terms of constant differentiation operators, e.g., the 2D Poisson equation in the weak form:

$$\int_{\Omega(q)} a(x, y) \nabla z \cdot \nabla w dx dy = \int_{\Omega(q)} f(x, y) w dx dy \tag{59}$$

with $(x, y)$ coordinates on the physical domain $\Omega(q)$, where $z(x, y)$ is the unknown function, $a(x, y)$ is a material parameter, $f(x, y)$ is the source term, $q$ is the optimization shape parameters.

In a typical FEM discretization, the "Discretize-then-Optimize approach" requires converting the equations to a fixed reference domain and then need to substitute into the equation, leading to a variable coefficient equation with an explicit dependence on shape parameters. In this case, the unknown is defined on the reference domain $\Omega_{ref}$ with coordinates $(u, v)$, mapped to the physical domain $\Omega(q)$ via the geometry map $x = x(u, v), y = y(u, v)$. If we denote the inverse of this map $u = u(x, y)$, $v = v(x, y)$, then the left-hand side of Equation (59) on the reference domain becomes

$$\int_{\Omega_{ref}} a(x, y)(\|\nabla u\|^2 z_x + \nabla u \cdot \nabla v z_y) w_x\ + (\|\nabla v\|^2 z_y + \nabla u \cdot \nabla v z_x) w_y |\det J(x, y)| du dv$$

with $\nabla$ denoting derivatives w.r.t. $x, y$, and $J(x, y)$ denoting the geometric map Jacobian matrix $\frac{\partial(x,y)}{\partial(u,v)}$. Here we spell out the expressions more explicitly instead of more concise matrix notation, to elucidate the increase in complexity. Please refer to Equation (48) for the complete derivation of shape derivatives following this way.

As typically the geometry map $x(u,v), y(u,v)$, rather than its inverse, is given explicitly in terms of shape parameters $q$ (as a linear function of $q$, if it is e.g., represented in a FEM basis), derivatives of $u, v$ w.r.t. $x, y$ need to be expressed in terms of derivatives of $x, y$ w.r.t. $u, v$, i.e., $\nabla u$, $\nabla v$ are the rows of the inverse of $J(x,y)$. In other words, a simple constant coefficient equation on a variable domain becomes a complex variable coefficient equation on a fixed domain, with coefficients depending on the geometric map in a complex nonlinear way. As a next step, these equations need to be discretized by substituting FEM expressions for $x(u,v;q)$,$y(u,v;q)$,$z(u,v)$, $f(u,v)$ in FEM basis, with the standard Galerkin procedure yielding stiffness matrix and right-hand side coefficients. Finally, the derivatives of the resulting coefficients with respect to $q$ need to be computed.

Note that the derivatives with respect to material parameters (e.g., coefficients of $a(x,y)$ in a FEM basis) unlike shape derivatives have similar complexity in either form. This is also true for elasticity equations: shape derivatives in the Discretize-then-Optimize setting are even more elaborate, but material parameter derivatives are relatively simple.

While, in the end, most equations required for shape derivative adjoints are very close to the forward equations (as shown in Equation (12) in the paper, the coefficient matrices are the same as in the forward solves), and can be computed relatively concisely, it is nontrivial to see this from differentiating the coefficients obtained from the equations above with respect to $q$. We are not aware of any tool that can automatically do this conversion, nor of any manual attempt ever done to compute shape derivatives in this way.